A study of well-balanced finite volume methods and refinement indicators for the shallow water equations

Sudi Mungkasi

September 2012

A thesis submitted for the degree of
Doctor of Philosophy
of The Australian National University

Dedicated to my wife, Asti,
our daughter, Daniella,
and my parents, Wagimin and Sulasmi.

This page was intentionally left blank.

Declaration

The work in this thesis is my own except where otherwise stated.

Sudi Mungkasi

This page was intentionally left blank.

Contents

Acknowledgements

The work for this thesis was undertaken at the Department of Mathematics, Mathematical Sciences Institute, The Australian National University (ANU). Here I acknowledge the contribution and support of a number of people, institutions and committees over the years of my candidature.

First and foremost, I sincerely thank my primary supervisor, Stephen Roberts, for his guidance, support, and encouragement. I have learnt a lot from him academically and non-academically. He has been very helpful in supporting me to do research in the directions of my own interests, which make me enjoy my PhD research. He has also been supportive to me in getting funds and travel grants during my PhD studies.

I am very grateful to my co-supervisors, Markus Hegland and Linda Stals. I acknowledge some discussions with Markus on weak local residuals and with Linda on adaptive grid methods.

I am indebted to some lecturers, postdoctoral fellows, staff, colleagues, and friends at the ANU. For some discussions, I thank Christopher Zoppou, Vikram Sunkara, Padarn Wilson, Brendan Harding, Mathew Langford, Shi Bai, Bin Zhou, Jiakun Liu, Srinivasa Subramanya Rao, Kowshik Bettadapura, Yuan Fang, and Chin Foon Khoo. I also thank Bishnu Lamichhane, John Urbas and Paul Leopardi also for some discussions. Kind thanks are due to Jodi Tutty and Annie Bartlett at the ANU Academic Skills and Learning Centre for some suggestions on the writing of this thesis. Thanks also go to Nick Guoth, Warren Yang and Kelly Wicks for technical and administrative support.

I thank my friends from Indonesia in Australia for the friendship, which has made me feel at home. Thanks are due to Robertus Anugerah Purwoko Putro and family, Hendra Gunawan Harno, Teddy Kurniawan, Jack Matsay and family, Supomo Suryo Hudoyo and family, Br Budi Hernawan OFM, and other Indonesian friends during my studies in Australia.

In my PhD period, I was visiting the Department of Applied Mathematics, the University of Washington, U.S.A. and Institut für Geometrie und Praktische Mathematik, RWTH Aachen University, Germany. I thank Professor Randall John LeVeque for his assistance and for some discussions, and Jihwan Kim, Jonathan Varkovitzky and Grady Lemoine at the University of Washington for some discussions. I thank Professor Sebastian Noelle for his assistance and some supervision on part of my work, and K. R. Arun, Guoxian Chen, and Marcel Makowski at RWTH Aachen University for some discussions.

During my PhD candidature, I was supported financially by The Australian National University. I acknowledge and thank the following institutions, organisations and committees for funding supports during my PhD candidature.

- The Australian National University for ANU PhD and Tuition Scholarships, ANU Vice Chancellor's travel grants, ANU Miscellaneous (top-up) Scholarships, and funding support for conferences,
- The Australian Mathematical Society (AustMS) for partial funding for my presentations in the AustMS conference meetings,
- ANZIAM and CSIRO for partial funding through ANZIAM-CSIRO Student Support Schemes for my presentations in the Engineering Mathematics and Applications Conference as well as Computational Techniques and Applications Conferences,
- Sanata Dharma University for covering the premium of my Overseas Health Cover Insurance,
- RWTH Aachen University for partial accommodation support while I visited Professor Sebastian Noelle,
- The University of Washington for one time in-city travel assistance while I visited Professor Randall John LeVeque,
- The Committe of the 2012 Gene Golub SIAM Summer School (G2S3) for the G2S3 travel grant funded by the U.S.A. Naval Postgraduate School for my participation in the summer school.

Last but not least, I thank my parents for their continuous encouragement and my wife, Asti, for her constant love.

Publications, Talks, and Awards

The following publications and preprints correspond to the work in this thesis.

- S. Mungkasi and S. G. Roberts, 2010, "On the best quantity reconstructions for a well balanced finite volume method used to solve the shallow water wave equations with a wet/dry interface", *ANZIAM Journal (E)*, 51: C48–C65, Australian Mathematical Society. (Based on the work in Chapter 2.)
  http://journal.austms.org.au/ojs/index.php/ANZIAMJ/article/view/2576/1289

- S. Mungkasi and S. G. Roberts, 2011, "A new analytical solution for testing debris avalanche numerical models", *ANZIAM Journal (E)*, 52: C349–C363, Australian Mathematical Society. (Based on the work in Chapter 3.)
  http://journal.austms.org.au/ojs/index.php/ANZIAMJ/article/view/3785/1465

- S. Mungkasi and S. G. Roberts, 2012, "Analytical solutions involving shock waves for testing debris avalanche numerical models", *Pure and Applied Geophysics*, 169 (10): 1847–1858, Springer. (Based on the work in Chapter 4.)
  http://dx.doi.org/10.1007/s00024-011-0449-1

- S. Mungkasi and S. G. Roberts, 2012, "Approximations of the Carrier-Greenspan periodic solution to the shallow water wave equations for flows on a sloping beach", *International Journal for Numerical Methods in Fluids*, 69 (4): 763–780, John Wiley & Sons. (Based on the work in Chapter 5.)
  http://dx.doi.org/10.1002/fld.2607

- S. Mungkasi and S. G. Roberts, 2011, "Numerical entropy production for shallow water flows", *ANZIAM Journal (E)*, 52: C1–C17, Australian Mathematical Society. (Based on part of the work in Chapter 6.)
  http://journal.austms.org.au/ojs/index.php/ANZIAMJ/article/view/3786/1410

- S. Mungkasi, S. G. Roberts, and S. Noelle, 2012, "Numerical entropy production as a refinement indicator for shallow water equations", *preprint*. (Based on part of the work in Chapter 6.)

- S. Mungkasi and S. G. Roberts, 2012, "Well-balanced computations of weak local residuals for shallow water equations", *preprint*. (Based on part of the work in Chapter 7.)

- S. Mungkasi and S. G. Roberts, 2012, "Weak local residuals as refinement indicators for shallow water equations", *preprint*. (Based on part of the work in Chapter 7.)

- S. Mungkasi and S. G. Roberts, 2011, "A finite volume method for shallow water flows on triangular computational grids", *Proceedings of IEEE International Conference on Advanced Computer Science and Information Systems (ICACSIS) 2011*, pages 79–84. (Based on the work in Appendix A.) `http://ieeexplore.ieee.org/xpl/freeabs_all.jsp?arnumber=6140781`

I have presented some parts of this thesis in talks during my PhD candidature. The talks are as follows.

- "Well-balanced finite volume methods for shallow water flows involving wet/dry interface" in the 53rd Australian Mathematical Society Annual Meeting, The University of South Australia, Adelaide, Australia, 28 Sep – 1 Oct 2009

- "Well-balanced finite volume methods for shallow water flows involving wet/dry interface" in Engineering Mathematics and Applications Conference 2009, The University of Adelaide, Adelaide, Australia, 6 – 9 Dec 2009

- "A new analytical solution for testing debris avalanche numerical models in the standard Cartesian coordinate system" in the 54th Australian Mathematical Society Annual Meeting, The University of Queensland, Brisbane, Australia, 27 – 30 Sep 2010

- "A new analytical solution for testing debris avalanche numerical models" in Computational Techniques and Applications Conference 2010, The University of New South Wales, Sydney, Australia, 28 Nov – 1 Dec 2010

- "Numerical entropy production for shallow water flows" in Computational Techniques and Applications Conference 2010, The University of New South Wales, Sydney, Australia, 28 Nov – 1 Dec 2010

- "Approximations of the Carrier-Greenspan periodic solution to the shallow water wave equations for flows on a sloping beach" in the 55th Australian Mathematical Society Annual Meeting, The University of Wollongong, Wollongong, Australia, 26 – 29 Sep 2011

- "A finite volume method for shallow water flows on triangular computational grids" in the IEEE International Conference on Advanced Computer Science and Information Systems (ICACSIS) 2011, Jakarta, Indonesia, 17 – 18 Dec 2011

- "Some exact solutions to shallow-water-type models and their use as numerical test problems" in a Seminar at IGPM, RWTH Aachen University, Aachen, Germany, 9 February 2012

I received the following awards during my PhD candidature.

- Best paper award in the IEEE International Conference on Advanced Computer Science and Information Systems (ICACSIS) 2011, Jakarta, Indonesia, 17 – 18 Dec 2011,

- Best presentation award, again in the IEEE International Conference on Advanced Computer Science and Information Systems (ICACSIS) 2011, Jakarta, Indonesia, 17 – 18 Dec 2011,

- ANU Vice Chancellor's travel grants to visit Professor Randall John LeVeque at the University of Washington, Seattle, U.S.A., 16 Nov–14 Dec 2011 and Professor Sebastian Noelle at RWTH Aachen University, Aachen, Germany, 6 Jan – 17 Feb 2012, and

- Travel grant from the U.S.A. Naval Postgraduate School to participate in the Gene Golub SIAM Summer School "Simulation and Supercomputing in the Geosciences", Monterey, California, U.S.A., 29 Jul – 10 Aug 2012.

This page was intentionally left blank.

Abstract

This thesis studies solutions to the shallow water equations analytically and numerically. The study is separated into three parts.

The first part is about well-balanced finite volume methods to solve steady and unsteady state problems. A method is said to be well-balanced if it preserves an unperturbed steady state at the discrete level. We implement hydrostatic reconstructions for the well-balanced methods with respect to the steady state of a lake at rest. Four combinations of quantity reconstructions are tested. Our results indicate an appropriate combination of quantity reconstructions for dealing with steady and unsteady state problems.

The second part presents some new analytical solutions to debris avalanche problems and reviews the implicit Carrier-Greenspan periodic solution for flows on a sloping beach. The analytical solutions to debris avalanche problems are derived using characteristics and a variable transformation technique. The analytical solutions are used as benchmarks to test the performance of numerical solutions. For the Carrier-Greenspan periodic solution, we show that the linear approximation of the Carrier-Greenspan periodic solution may result in large errors in some cases. If an explicit approximation of the Carrier-Greenspan periodic solution is needed, higher order approximations should be considered. We propose second order approximations of the Carrier-Greenspan periodic solution and present a way to get higher order approximations.

The third part discusses refinement indicators used in adaptive finite volume methods to detect smooth and nonsmooth regions. In the adaptive finite volume methods, smooth regions are coarsened to reduce the computational costs and nonsmooth regions are refined to get more accurate solutions. We consider the numerical entropy production and weak local residuals as refinement indicators. Regarding the numerical entropy production, our work is the first to implement the numerical entropy production as a refinement indicator into adaptive finite

volume methods used to solve the shallow water equations. Regarding weak local residuals, we propose formulations to compute weak local residuals on nonuniform meshes. Our numerical experiments show that both the numerical entropy production and weak local residuals are successful as refinement indicators.

Abbreviations

1D, 1.5D, 2D	one dimension, one-and-a-half dimensions, two dimensions
CFL	Courant-Friedrichs-Lewy
CG	Carrier-Greenspan
CK	Constantin-Kurganov
FVM	Finite Volume Method(s)
*i*FEM	innovative Finite Element Method
KKP	Karni-Kurganov-Petrova
MHR	Mangeney-Heinrich-Roche
NEP	Numerical Entropy Production
nNEP	normalised Numerical Entropy Production
SI	Systéme International (International System)
WLR	Weak Local Residual(s)

This page was intentionally left blank.

Chapter 1

Thesis overview

In this chapter, we provide the motivation, purpose, outline and contributions of this thesis.

1.1 Motivation

The initial motivation of this research comes from natural disasters caused by water flows, such as the Indian Ocean Boxing Day tsunami in 2004. Water flows can be modelled mathematically. One available model is the shallow water equations. Solving the shallow water equations is useful, as the solution can be used to predict where water will flow, how fast it will flow, how large an area is inundated, and if there is a possible dry region for a route of rescue or escape.

Some authors give the shallow water equations [53, 70] different names, such as, shallow water-wave equations [30] or Saint-Venant models [41] (Saint-Venant systems due to A. J. C. B. de Saint Venant [18]). We use these terms interchangeably depending on the term used in previous work by other researchers.

Exact analytical solutions to the shallow water equations are not available, except for specific cases (for example, dam break problems [58, 66], debris avalanche problems [41], and waves on a sloping beach [12]). One way to approximate or solve the shallow water equations in general is by use of numerical methods. In this thesis, we study analytical and numerical solutions to the shallow water equations, so that our contributions can be used in building better simulations of shallow water flows.

A number of numerical methods used to solve the shallow water equations are available in the literature. Some of those numerical methods are finite difference

methods [42, 67], finite element methods [73], and finite volume methods [7, 39, 40]. In this thesis we choose to use finite volume methods, and do not discuss other classes of methods.

Finite volume methods discretise a given domain into a finite number of cells. In the time evolution, the averaged quantities in each cell are updated by numerical fluxes and source terms. In particular, a finite volume method used to solve the shallow water wave equations is essentially defined in terms of the reconstruction of conserved quantities at the interfaces between cells, which are used to calculate fluxes across these interfaces.

Finite volume methods have at least two advantages over the physics of shallow water waves, and hence, over the accuracy of the numerical methods. First, finite volume methods are based on weak (integral) formulations, so the methods should be able to resolve smooth and nonsmooth (discontinuous) solutions better than other numerical methods, such as finite difference methods which are based on differential formulations. It is well-known that the shallow water equations, which are hyperbolic systems, admit discontinuous solutions even when the initial condition is smooth. Second, the methods can conserve the volumes of mass and momentum, as long as conservative numerical schemes are used. More descriptions on finite volume methods can be found in lecture notes and text books, such as those written by LeVeque [39, 40] and Bouchut [6].

Even though finite volume methods have the aforementioned advantages, their ability to resolve the steady state solutions and the accuracy of the resulting numerical solutions at wet/dry interfaces, shocks and contact discontinuities are still an issue [2, 53, 57]. This thesis will present possible ways to deal with this issue.

1.2 Purpose

The aims of this thesis are:

a. to propose implementations of well-balanced finite volume methods used to solve the shallow water equations,

b. to derive some analytical solutions to the problems of debris avalanche and periodic flow on a sloping beach, which can be used to test the accuracy of finite volume or other numerical methods, and

c. to develop error indicators for adaptive mesh refinement or coarsening for finite volume methods.

In the first aim, we study well-balanced methods. A method is said to be well-balanced if it preserves an unperturbed steady state at the discrete level. A standard (non-well-balanced) method may lead to spurious oscillations of water, when it is used to simulate the steady state of a lake at rest [53]. A well-balanced finite volume method is intended to give accurate solutions of steady state problems, while it can also solve nonsteady state problems. In this thesis, we study well-balanced methods based on hydrostatic reconstructions originally proposed by Audusse et al. [2]. We test different options for the reconstruction variables, and seek an appropriate choice of reconstruction variables for various situations when solving the shallow water equations using finite volume methods.

In the second aim, we study the debris-avalanche problems using the shallow water or Saint-Venant approach. We use the term *debris-avalanche* following the work of Mangeney et al. [41] in order to get a consistent terminology. Most researchers use the term *debris-avalanche* in relation to the Savage-Hutter model [60, 61], which is a modified Saint-Venant model [18]. New analytical solutions are derived and they can be used as benchmark solutions to test the performance of finite volume or other numerical methods.

As part of the second aim, some periodic flows on a sloping beach are studied. Analytical and numerical approximations of the flows are compared and discussed. The exact analytical solutions of the periodic flows were originally proposed by Carrier and Greenspan [12] in implicit forms. These exact solutions are often used as benchmark solutions to test the performance of finite volume or other numerical methods. An explicit (closed-form) approximation was introduced by Johns [31] in order to develop a numerical scheme, but we claim that the approximation can lead to large errors in some cases. We derive higher order explicit approximations to get more accurate solutions than that introduced by Johns [31].

In the third aim, we study error indicators used in adaptive mesh refinement, or coarsening, for finite volume methods. Error indicators are also known as refinement indicators, smoothness indicators, or shock detectors. The indicators we focus on are the numerical entropy production and weak local residuals. Puppo [54, 55] and Puppo and Semplice [56, 57] developed and implemented the numerical entropy production as a smoothness indicator for conservation laws. We adapt and implement the numerical entropy production as a smoothness in-

dicator for the shallow water equations in particular. Kurganov et al. [32, 33] proposed weak local residuals as smoothness indicators for conservation laws on uniform meshes. We extend the work of Kurganov et al. [32, 33] to balance laws (conservation laws with nonzero source terms) and specifically to the shallow water equations. We present a way of computing weak local residuals on nonuniform meshes, so that they can be used as smoothness indicators in adaptive-mesh finite volume methods.

1.3 Outline and contributions

This thesis is written in three parts, which correspond to the aims of this thesis. Part I consists of only one chapter, Chapter 2. Part II is constituted of Chapter 3, Chapter 4, and Chapter 5. Part III comprises Chapter 6 and Chapter 7.

The original contributions of this thesis are as follows.

- We give a performance comparison of several combinations of quantity reconstructions and indicate an appropriate choice of combination for a well-balanced method. This is given in Chapter 2. This contribution has been published in *ANZIAM Journal* [45].

- We derive a new analytical exact solution to the debris avalanche problem involving a dry area, and demonstrate its use in numerical tests. This contribution is covered in Chapter 3, and has been published in *ANZIAM Journal* [46].

- We derive a new analytical exact solution to the debris avalanche problem involving shock waves, and demonstrate its use in numerical tests. Chapter 4 covers this contribution, which has been published in *Pure and Applied Geophysics* journal [48].

- We show that the linear approximation of the Carrier-Greenspan periodic solution can lead to large errors. A new simple formula for the shoreline velocity is presented. We propose second order explicit approximations and present a way to obtain higher order approximations of the exact solution. These contributions are given in Chapter 5, and have been published in *International Journal for Numerical Methods in Fluids* [50].

- We formulate numerical entropy production as a refinement indicator for the shallow water equations. We prove properties of numerical entropy schemes relating to the steadiness of a lake at rest and its consistency to the entropy equation on smooth regions. Numerical entropy production is implemented in adaptive methods in one, one-and-a-half, and two dimensions successfully. These contributions are covered in Chapter 6. Some of them have been published in *ANZIAM Journal* [47].

- We formulate weak local residuals as a refinement indicator for balance laws, and in particular, the shallow water equations. We propose a well-balanced technique to compute weak local residuals of the momentum equation in one dimension. Implementations of weak local residuals in adaptive methods in one, one-and-a-half, and two dimensions are demonstrated. These contributions are given in Chapter 7.

About two thirds of the contributions in this thesis have been published (see pages xiii–xv of this thesis for detailed publications) and the rest is currently in preparation for publication submissions.

This page was intentionally left blank.

PART I:
WELL-BALANCED METHODS

This page was intentionally left blank.

Chapter 2

Well-balanced methods*

2.1 Introduction

When solving the shallow water wave equations, a robust and accurate numerical method is ideally needed. Such a method should be able to deal with both steady and unsteady state problems. In addition, the error produced by the method should be small on a relatively coarse discretisation of the domain. Recall that this thesis considers finite volume numerical methods.

Constructing a robust and accurate finite volume method is not without difficulties. One well-known difficult task for finite volume methods is wetting and drying processes through wet/dry interfaces. Some authors, such as Bollermann, Kurganov, and Noelle [5], Briganti and Dodd [9], Brufau, Vázquez-Cendón, and García-Navarro [11], Gallardo, Parés, and Castro [24], have attempted to deal with these wetting and drying problems. However, these problems have not been perfectly solved.

In this chapter, we investigate the use of various reconstruction strategies in order to construct a robust and accurate finite volume method that can deal with the wet/dry interface problem and solve both steady and unsteady state problems. We shall make a recommendation on an appropriate choice of reconstruction that leads to an accurate and robust well-balanced method. Note that a numerical method is said to be well-balanced if it preserves an unperturbed steady state at the discrete level.

The remainder of this chapter is organised as follows. We recall the one-dimensional shallow water equations and well-balanced finite volume methods

*The results of this chapter have been published [45].

in Section 2.2. In Section 2.3, we provide four combinations of quantity reconstructions. We then test the resulting methods with each combination to solve steady and unsteady state problems, where the simulation results are presented in Section 2.4. Finally, some concluding remarks are drawn in Section 2.5.

2.2 Governing equations and numerical methods

In this section, we recall the one-dimensional shallow water wave equations and a well-balanced finite volume method.

The conservative form of the one-dimensional shallow water wave equations is

$$\mathbf{q}_t + \mathbf{f}(\mathbf{q})_x = \mathbf{s}\,, \tag{2.1}$$

in which the quantity vector $\mathbf{q}$, the flux function $\mathbf{f}$, and the source term $\mathbf{s}$ are

$$\mathbf{q} = \begin{bmatrix} h \\ hu \end{bmatrix}, \quad \mathbf{f} = \begin{bmatrix} hu \\ hu^2 + \frac{1}{2}gh^2 \end{bmatrix}, \quad \text{and} \quad \mathbf{s} = \begin{bmatrix} 0 \\ -ghz_x \end{bmatrix}. \tag{2.2}$$

Here, x represents the one-dimensional spatial variable, t represents the time variable, $u = u(x,t)$ denotes the water velocity, $h = h(x,t)$ denotes the water height (depth), $z = z(x)$ denotes the topography (bed elevation), $w = h + z$ is the water stage, and g is the acceleration due to gravity. A mathematical derivation of (2.1) can be found in our previous work [43] or other references [30, 40] on shallow water equations.

An interesting problem arises for the "simple" lake at rest problem. In this case the vertical pressure term $(\frac{1}{2}gh^2)_x$ needs to precisely balance the bed gravity term $-ghz_x$. For a numerical scheme, the discretisation of these two terms needs to be carefully undertaken to maintain this balance. A finite volume method is said to be *well-balanced* if it preserves this balance, that is if it preserves the lake at rest solution ($u = 0,\ w =$ constant). Note that there exists a well-balanced method based on moving water, but we do not discuss this type of well-balanced method in this thesis.

To define a finite volume method we need to specify the way flow quantities are reconstructed at the interfaces between cells. Suppose at the $i + \frac{1}{2}$ interface between the ith and $(i+1)$th cells, we have used a standard technique to recon-

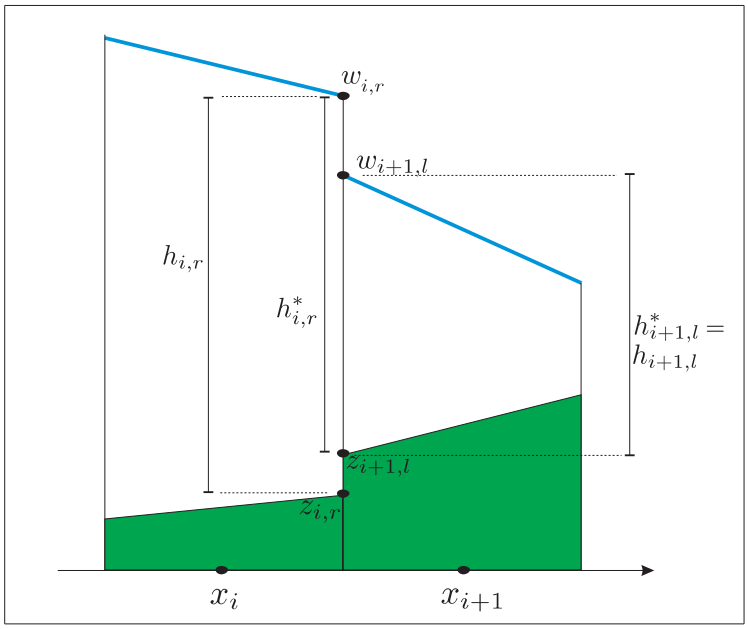

Figure 2.1: An illustration of the hydrostatic reconstruction at an interface between two cells for stage w, height h, and bed elevation z. In this figure, $z^*_{i+\frac{1}{2}} = z_{i+1,l}$.

struct the values of water depth and bed, $h_{i,r}$ and $z_{i,r}$ on the right edge of the ith cell and $h_{i+1,l}$ and $z_{i+1,l}$ on the left edge of the $(i+1)$th cell.

To obtain a well-balanced scheme, we use the hydrostatic reconstruction that was originally proposed by Audusse et al. [2] for first and second order methods and extended by Noelle et al. [53] for higher order methods. The new reconstructed values of h and z at the $i+\frac{1}{2}$ interface are

$$z^*_{i+\frac{1}{2}} := \max\{z_{i,r}, z_{i+1,l}\}\,, \tag{2.3}$$

$$h^*_{i,r} := \max\{0, h_{i,r} + z_{i,r} - z^*_{i+\frac{1}{2}}\}\,, \tag{2.4}$$

$$h^*_{i+1,l} := \max\{0, h_{i+1,l} + z_{i+1,l} - z^*_{i+\frac{1}{2}}\}\,. \tag{2.5}$$

An illustration of this spatial setting for the hydrostatic reconstruction is given in Figure 2.1. The values for h^* lead to auxiliary values for the conserved quantities, $\mathbf{Q}^* = (h^*, h^*u)^T$.

A semi-discrete version of our well-balanced finite volume scheme is [2, 53]

$$\Delta x_i \frac{d}{dt}\mathbf{Q}_i + \mathcal{F}^r(\mathbf{Q}_i, \mathbf{Q}_{i+1}, z_{i,r}, z_{i+1,l}) - \mathcal{F}^l(\mathbf{Q}_{i-1}, \mathbf{Q}_i, z_{i-1,r}, z_{i,l}) = \mathbf{S}_i^{(j)}\,, \tag{2.6}$$

where the right and left numerical fluxes of the ith cell are respectively calculated

at $x_{i+1/2}$ and $x_{i-1/2}$, and

$$\mathcal{F}^r(\mathbf{Q}_i, \mathbf{Q}_{i+1}, z_{i,r}, z_{i+1,l}) := \mathbf{F}(\mathbf{Q}^*_{i,r}, \mathbf{Q}^*_{i+1,l}) + \mathbf{S}_{i,r}\,, \tag{2.7}$$

and

$$\mathcal{F}^l(\mathbf{Q}_{i-1}, \mathbf{Q}_i, z_{i-1,l}, z_{i,r}) := \mathbf{F}(\mathbf{Q}^*_{i-1,r}, \mathbf{Q}^*_{i,l}) + \mathbf{S}_{i,l}\,. \tag{2.8}$$

Here, $\mathbf{Q}$ is the approximation of the vector $\mathbf{q}$, and $\mathbf{F}$ is a conservative numerical flux consistent with the homogeneous shallow water wave equations computed in such a way that the method is stable. In addition,

$$\mathbf{S}_{i,r} := \begin{bmatrix} 0 \\ \frac{g}{2}h^2_{i,r} - \frac{g}{2}(h^*_{i,r})^2 \end{bmatrix}, \quad \mathbf{S}_{i,l} := \begin{bmatrix} 0 \\ \frac{g}{2}h^2_{i,l} - \frac{g}{2}(h^*_{i,l})^2 \end{bmatrix} \tag{2.9}$$

are the corrections due to the water height modification in the hydrostatic reconstruction. Furthermore, the index j of $\mathbf{S}_i^{(j)}$ in equation (2.6) denotes the order of the numerical source term. First and second order numerical source terms are

$$\mathbf{S}_i^{(1)} := \begin{bmatrix} 0 \\ 0 \end{bmatrix} \quad \text{and} \quad \mathbf{S}_i^{(2)} := \begin{bmatrix} 0 \\ g\frac{h_{i,l}+h_{i,r}}{2}(z_{i,l} - z_{i,r}) \end{bmatrix}. \tag{2.10}$$

The well-balanced finite volume method presented above must be completed by quantity reconstructions used for flux computations, as will be discussed in the next section.

2.3 Quantity reconstructions

In this section, we investigate combinations of reconstruction quantities for finite volume methods used to solve the shallow water equations.

For the one-dimensional shallow water wave equations, we consider five quantities, namely: water height h, bed z, stage w, water velocity u, and momentum $p := hu$. Reconstructing two elements of the set $\{h, z, w\}$ together with one element of the set $\{u, p\}$ is enough to solve the equations in general. We are interested in those reconstructions that involve the reconstruction of stage w as it is the most important quantity in the development of a well-balanced method.

We consider four combinations of reconstruction quantities, namely:

A. stage w and momentum p (where bed z is fixed);

B. stage w and velocity u (where bed z is fixed);

C. stage w, water height h, and velocity u;

D. stage w, bed z, and velocity u.

Combination C was used by Audusse et al. [2], and we test the performance of this combination against the other combinations. Combination A, Combination B, and Combination C never result in negative water height, while Combination D results in negative water height at the wet/dry interface if it is applied naïvely. In addition, Combination A and Combination B allow piece-wise continuous linear approximation of the bed topography, while Combination C and Combination D lead to piece-wise discontinuous linear approximation of the bed topography.

When the second order method is used, Combination D may lead to negative water height if a modification is not made at the wet/dry interface [2]. An occurrence of negative water height is illustrated in Figure 2.2. In order to get a well-balanced method that is physically valid, negative water heights are not allowed. Therefore, we modify the quantity reconstructions around the wet/dry interfaces as follows. Consider the steady state of a lake at rest. We use the minmod limiter [40] for simplicity. Suppose that a wet/dry interface occurs at the ith cell and that $z_{i,r} > w_{i,r}$. Then we define an auxiliary variable $\delta = z_{i,r} - w_{i,r}$. In order to maintain conservation, we modify the value of z on both the right and on the left of the ith cell

$$z_{i,r}^{\text{new}} = w_{i,r} \quad \text{and} \quad z_{i,l}^{\text{new}} = z_{i,l} + \delta\,. \tag{2.11}$$

These new values replace the old ones and are used in subsequent computations. Such a modification is shown in Figure 2.3. This modification forces the water height reconstruction to be nonnegative, so that a method using Combination D can be used to solve steady state problems. Unfortunately, a method using Combination D with this modification leads to unphysical solutions at wet/dry areas when it is used to solve unsteady state problems, as we will see in Subsection 2.4.2.

In the next section (Section 2.4), the well-balanced scheme using Combination A of reconstruction quantities is called Method A; likewise, Method B, Method C, and Method D denote the well-balanced schemes using Combination B, Combination C, and Combination D respectively. Note that we apply the modification at the wet/dry interface for Method D.

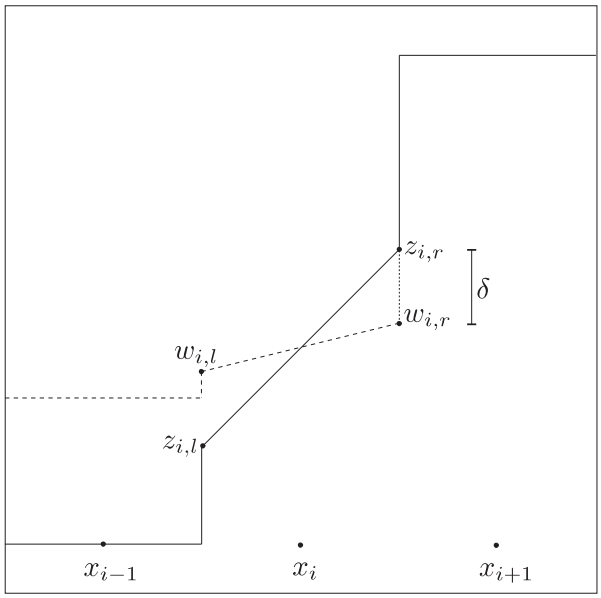

Figure 2.2: An occurrence of negative water height when the minmod limiter is used. Here, the free surface is shown by the dashed line and the water bed by the continuous line.

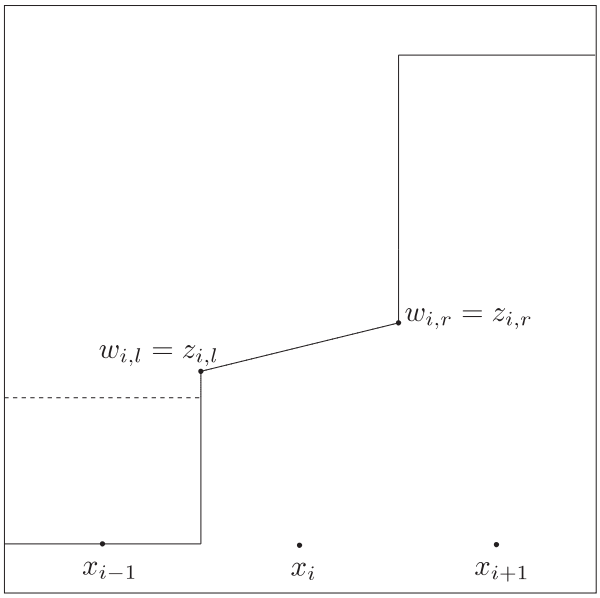

Figure 2.3: A modified reconstruction relating to the previous figure. Here, the free surface is shown by the dashed line and the water bed by the continuous line.

2.4 Numerical tests

We provide simulation results in this section. We use Python 2.4 software and adapt the ANUGA package[†] for programming. Steady and unsteady state problems are considered. The simulations use the second order source term $\mathbf{S}_i^{(2)}$ and second order spatial and temporal discretisations.

The numerical setting is as follows. We use the central upwind formulation proposed by Kurganov, Noelle, and Petrova [36] to compute the numerical fluxes. Quantities are measured in Systéme International (SI) units, and the acceleration due to gravity is set as $g = 9.81$. The minimum water height allowed in the flux computation is $h_{\min} = 10^{-6}$. The minmod limiter is used for quantity reconstruction. In the current experiments, each spatial domain is discretised into 400 cells. The Courant-Friedrichs-Lewy (CFL) number used in the simulations is 1.0.

The discrete L^1 absolute error

$$E = \frac{1}{N}\sum_{i=1}^{N} |q(x_i) - Q_i| \tag{2.12}$$

is used to quantify numerical error, where N is the number of cells, q is the exact quantity function, x_i is the centroid of the ith cell, and Q_i is the average value of quantity of the ith cell produced by the numerical method. The L^1 *absolute* error is chosen, rather than the relative error, as it applies to both zero velocity and nonzero velocity cases. The relative error of the velocity is not defined for zero velocity.

To compute the velocity based on momentum and height, we proceed as follows. With the momentum $p = hu$ and the water stage w as conserved quantities, the flux calculation requires the value of velocity u where $u = p/h$ and the water depth h is calculated by $h = w - z$. If the water depth approaches zero, the calculation of velocity u becomes numerically unreliable and produces unphysically large velocities at wet/dry interfaces. The calculation problems due to small water depths near a wet/dry interface can be alleviated by regularising the velocity as described by Roberts et al. [59]. The regularised velocity is defined as

$$u = \frac{p}{h + \epsilon/h}\,, \tag{2.13}$$

where $\epsilon = 10^{-12}$ is a regularisation parameter that controls the minimal magnitude of the denominator.

[†]http://anuga.anu.edu.au/

In the following two subsections, numerical results are presented. We consider two representative problems with wet/dry interfaces, namely: a steady "lake at rest with shoreline" and an unsteady "oscillating lake on a parabolic bed". The first problem has a fixed wet/dry interface, while the second problem has a moving wet/dry interface.

2.4.1 Steady state: a lake at rest

First, we consider the steady state of a lake at rest as follows. Suppose that we have the topography of an artificial lake, with the lake at rest and the stage with a value of $w = 4.5$ as shown in Figure 2.4. This lake is specifically made so that it has sloping wet/dry interfaces, discontinuous wet/dry interfaces, and discontinuities of the topography. Sloping wet/dry interfaces occur on the left and on the right "ends" of the lake. In addition, discontinuous wet/dry interfaces are found in the middle of the lake due to the existence of an island with very steep shore. This artificial setting is intended to make the problem difficult to solve by numerical methods.

Our experiments show that Methods A and B, which approximate the bed z as a continuous function, fail to be well-balanced. These methods can maintain the well-balanced property at wet/wet interfaces, but fail around wet/dry interfaces. The failure is significant if the wet/dry interface involves large changes in the bed as demonstrated by the island given in our test.

The reason for this failure can be described as follows. When we take the approximation of bed z to be continuous (as in Methods A and B) and the water height h to be nonnegative, we may have a cell with sloping water surface at wet/dry interface as shown in Figure 2.5 so as to maintain the conservation of the water. This leads to a nonzero flux at the interface of that cell, which then induces a nonzero momentum and so the water moves. The motion at wet/dry interface propagates to cells next to it and so on, leading to a lake which is not at rest. Indeed the resulting velocities can be quite large. This type of numerical solution is known as a numerical storm [53].

In contrast, Methods C and D, which approximate the bed z discontinuously, are successful in solving this steady state problem. In our simulations, the results generated by Methods C and D at time $t = 2.0$ have errors for the momentum and for the velocity on the order of 10^{-15}, which is machine accuracy.

From these results, a finite volume scheme using a well-balanced flux calcu-

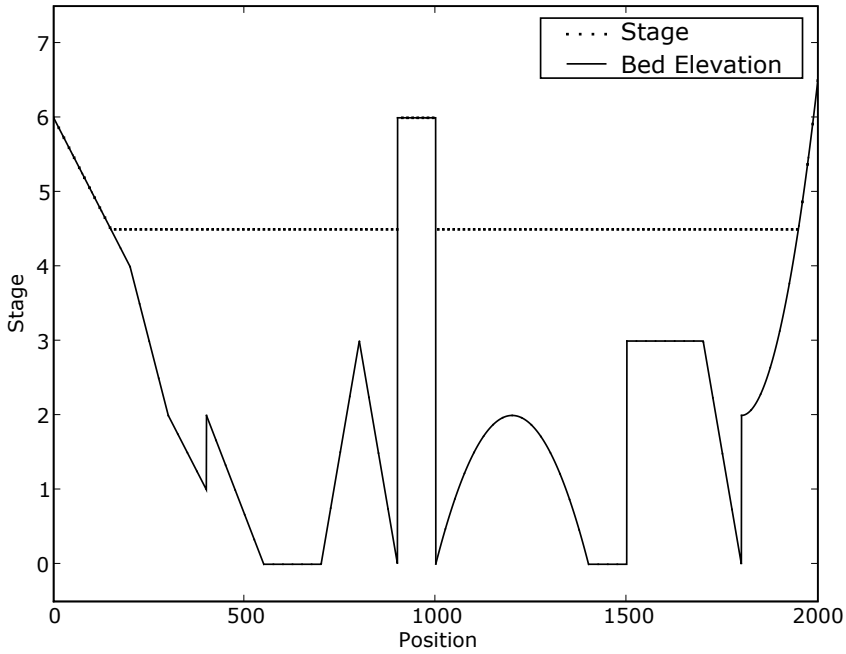

Figure 2.4: Cross section for topography of a lake at rest.

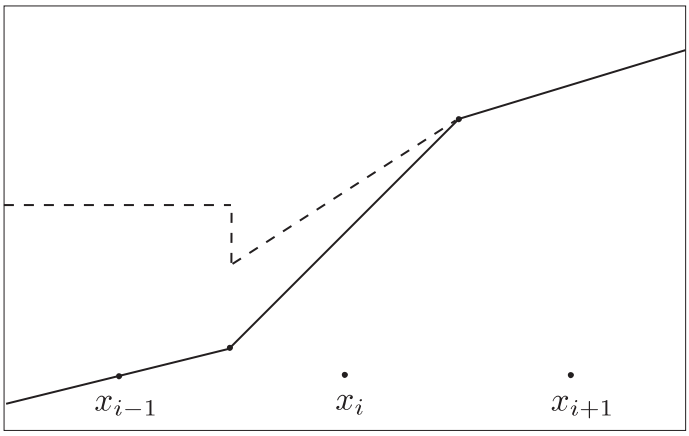

Figure 2.5: Piece-wise continuous linear approximation of bed z at wet/dry interface. Free surface (dashed line). Water bed (continuous line).

lation is successful in preserving the steady state of a lake at rest if the spatial domain is all wet. However, it may fail in preserving that steady state if the spatial domain contains wet/dry interfaces. Extra care must be taken when reconstructing the quantities in this case.

2.4.2 Unsteady state: oscillation on a parabolic bed

The second test is unsteady state oscillation on a parabolic bed as follows. Consider a parabolic canal bed

$$z = \frac{D_0}{L^2} x^2 \,, \tag{2.14}$$

where D_0 will denote the maximum equilibrium water depth with an equilibrium horizontal water surface length of $2L$. Let A denote the amplitude of the oscillation. We consider initial conditions in this canal, for the water velocity u and stage w given by

$$u = 0 \tag{2.15}$$

and

$$w = D_0 + \frac{2AD_0}{L^2}[x - A/2] \,. \tag{2.16}$$

The solution of this problem consists of the flat water surface moving up one side of the canal, reaching a maximum height and then falling back and then rising on the other side of the canal, and then repeating indefinitely. Therefore, the solution is an oscillation. Following Thacker [71], we find the exact (analytical) solution, in terms of velocity u and stage w, to be

$$u = -A\omega \sin(\omega t) \,, \tag{2.17}$$

$$w = D_0 + \frac{2AD_0}{L^2} \cos(\omega t) \left[x - \frac{A}{2} \cos(\omega t) \right] \,, \tag{2.18}$$

where the angular frequency ω and the period T of oscillation are respectively

$$\omega = \frac{\sqrt{2gD_0}}{L} \quad \text{and} \quad T = \frac{2\pi}{\omega} \,. \tag{2.19}$$

In addition, the shorelines are located at

$$x = A\cos(\omega t) \pm L \,. \tag{2.20}$$

Note that at dry areas we have $u = 0$ and $w = z$.

We use this exact solution to test the properties of the different choices of reconstruction. For our numerical experiment we consider the case where $D_0 =$

Table 2.1: Errors in water height h, momentum p and velocity u at $t = T$; and the maximum absolute velocity $u_{\max}$ involved at $t = T$. Method A fails.

Method	h error	p error	u error	$u_{\max}$
A	-	-	-	-
B	$1.26 \cdot 10^{-3}$	$1.00 \cdot 10^{-2}$	$2.60 \cdot 10^{-3}$	0.4
C	$1.03 \cdot 10^{-2}$	$8.08 \cdot 10^{-2}$	$1.94 \cdot 10^{-2}$	0.9
D	$1.88 \cdot 10^{-3}$	$1.37 \cdot 10^{-2}$	$2.25 \cdot 10^{-1}$	7.9

10, $L = 2500$ and $A = L/2$. The spatial domain to be discretised is the interval $[-2L, 2L]$.

The error comparison and the maximum absolute velocities $u_{\max}$ obtained at time $t = T$ (where T is the period of oscillation) for the various reconstruction methods are given in Table 2.1. We deem that Method A fails to solve this problem since it requires artificially small time steps relative to the other methods. Methods B and C successfully solve this problem. Method B results in the smallest error (but recall that Method B fails to solve the steady state problem as discussed in Subsection 2.4.1). Figure 2.6 shows the numerical results for Method C at time $t = T$, and Figure 2.7 is a magnification of Figure 2.6 at cells around wet/dry interface on the interval $[3500, 3850]$. Note that Method D leads to unphysical velocity in some of the dry areas as Figure 2.8 illustrates. Therefore, Method C, which is a well-balanced method with reconstruction on stage w, water height h, and velocity u, performs better than the other methods in general.

2.5 Concluding remarks

We find that the well-balanced finite volume scheme combined with quantity reconstructions based on stage, height, and velocity has been found to be more robust and accurate than the same scheme combined with quantity reconstructions based on either:

- stage and momentum (where bed is fixed);
- stage and velocity (where bed is fixed); or
- stage, bed, and velocity.

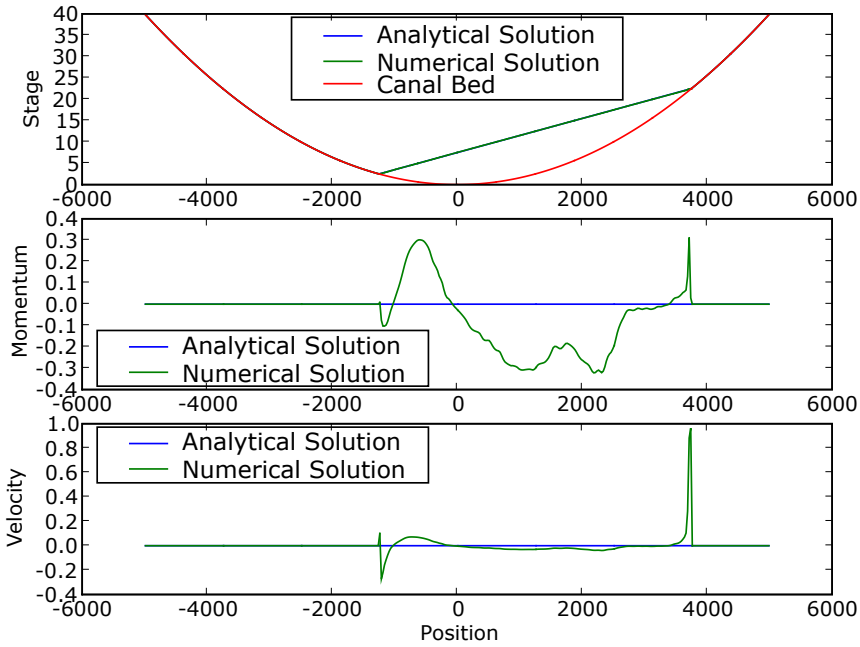

Figure 2.6: Simulation results at time $t = T$ using Method C.

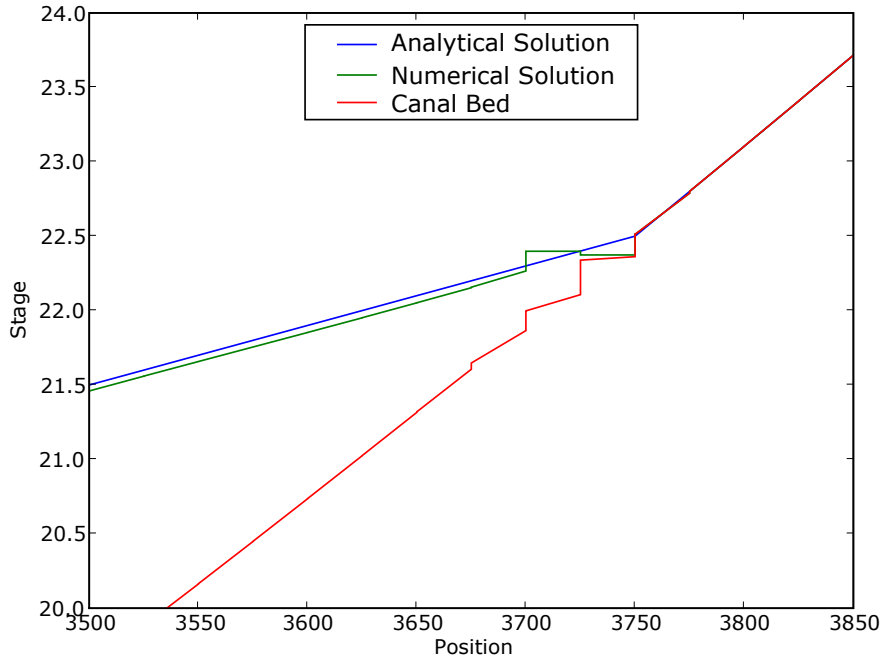

Figure 2.7: A magnification of the cells on interval $[3500, 3850]$ at time $t = T$ using Method C. The canal bed is the discretised version.

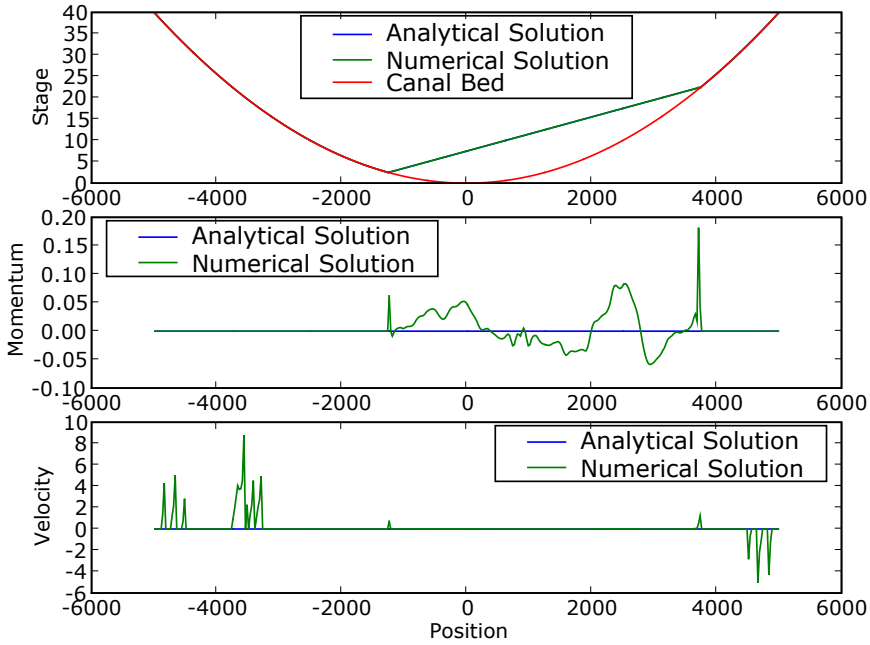

Figure 2.8: Simulation results at time $t = T$ using Method D. Unphysical velocity occurs at dry areas.

We note that when the velocity is zero, the momentum is zero. This means that stage and height are the appropriate choice for variable reconstructions to get a well-balanced method.

The discussion in this chapter was limited in one dimension. Many parameters are involved in our numerical simulations, such as the CFL number, the minimum water height allowed in the flux computation, velocity regularisation, and the slope limiter. We have only taken specific values for each of these parameters and used the standard minmod limiter.

In the next part (Part II) of this thesis, we shall present some analytical solutions and use them as benchmarks for testing further numerical solutions.

This page was intentionally left blank.

PART II:
SOME EXACT SOLUTIONS

This page was intentionally left blank.

Chapter 3

Avalanche involving a dry area*

3.1 Introduction

Avalanche problems have been studied using the Saint-Venant approach (shallow water wave equations) by a number of researchers [41, 46, 52, 65, 66] on a planar topography. The planar topography makes avalanche models simpler than models based on arbitrary topography. Indeed, we limit our discussion in this chapter to problems with planar topography. Readers interested in shallow water models for arbitrary topography are referred to other work, such as that of Bouchut and Westdickenberg [8] and the references therein. In addition, those interested in solving avalanche problems using a modified Saint-Venant model called the Savage-Hutter model [60, 61] are referred to the work of Tai et al. [69] and the references therein.

Some research on dam break and debris avalanche problems using the Saint-Venant model is summarised as follows. Ritter [58] and Stoker [65, 66] solved the so called "dam break" problem for the case with horizontal topography. Mangeney et al. [41] derived an analytical solution to the debris avalanche problem in a topography-linked coordinate system involving a dry area, where the wall separating quiescent wet and dry areas initially is not vertical, but orthogonal to the topography. The dam break and debris avalanche problems were solved by employing the characteristics of the Saint-Venant model.

Because a nonvertical dam is not very similar to some real-world scenarios [1], we shall consider a modified problem having a vertical wall initially and develop its solution in the standard Cartesian coordinate system. That is, in this chapter

*The results of this chapter have been published [46]

we derive an analytical solution to a debris avalanche problem having initial vertical wall in the standard Cartesian coordinate system. Characteristics and a transformation technique are used to obtain the analytical solution.

The analytical solution, which we shall derive, to a debris avalanche problem is based on the Saint-Venant approach. Using the Saint-Venant approach implies that debris is treated as a depth-averaged fluid. We use this analytical solution as a benchmark to assess two finite volume methods applied to the debris avalanche problem. The considered debris avalanche problem is a simplification of real world scenarios on the avalanches of debris, such as snow, sands, rocks, as well as landslides. In other words, our work can be an aid in simulations of these real world scenarios.

Three problems are considered. The first is the dam break problem in the standard Cartesian coordinate system having initial condition shown in Figure 3.1(a). This problem has been solved by Ritter [58]. The second is the debris avalanche problem in the topography-linked coordinate system having initial condition illustrated in Figure 3.1(b). Mangeney et al. [41] have proposed a solution to this problem. The third is the debris avalanche problem in the standard Cartesian coordinate system having initial condition shown in Figure 3.1(c). This third problem represents a modified version of the first and second problems, and is the one we solve in this chapter.

The rest of this chapter is structured as follows. We review the Saint-Venant models involving a Coulomb-type friction in Section 3.2. In Section 3.3, we recall the existing solutions of Ritter [58] and Mangeney, Heinrich, and Roche [41]. Section 3.4 provides a new analytical solution to the modified debris avalanche problem. We implement the new analytical solution to test the performance of finite volume methods and present the numerical results in Section 3.5. Finally, Section 3.6 concludes this chapter with some remarks about the new solution.

3.2 Saint-Venant models

In this section, we review the Saint-Venant model in the standard Cartesian coordinate system and the Saint-Venant model in the topography-linked coordinate system. In the previous chapter, derivatives of functions were denoted by shorthand notations like $()_x$ and $()_t$. Note that here we use the Leibniz notations, like $\frac{\partial}{\partial x}$ and $\frac{\partial}{\partial t}$, for derivatives of functions in order to help the analytical work in this

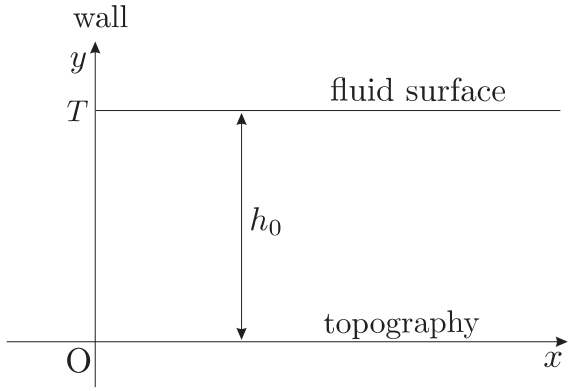

(a)

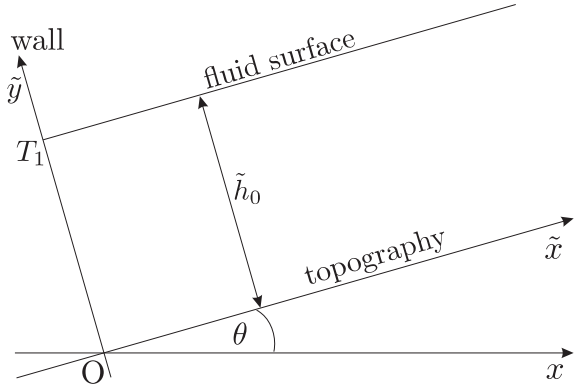

(b)

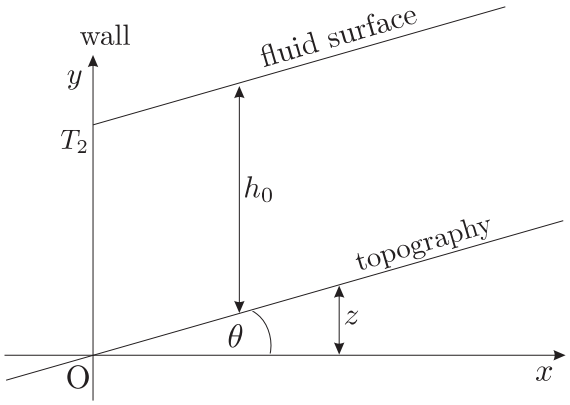

(c)

Figure 3.1: Initial conditions of three considered problems: (a) A dam break problem in the standard Cartesian coordinate system. (b) A debris avalanche problem in the topography-linked coordinate system. (c) A debris avalanche problem in the standard Cartesian coordinate system.

section.

3.2.1 Equations in the standard Cartesian coordinate

Recall that in the standard Cartesian coordinate system, the mass and momentum equations governing the fluid motion are

$$\frac{\partial h}{\partial t} + \frac{\partial (hu)}{\partial x} = 0\,, \tag{3.1}$$

$$\frac{\partial (hu)}{\partial t} + \frac{\partial \left(hu^2 + \frac{1}{2}gh^2\right)}{\partial x} = -gh\frac{dz}{dx} + hF\,. \tag{3.2}$$

These two equations are called the Saint-Venant model or the shallow water equations in the standard Cartesian coordinate system. Here, x represents the coordinate in one-dimensional space, t represents the time variable, $u = u(x,t)$ denotes the fluid velocity, $h = h(x,t)$ denotes the fluid height, $z = z(x)$ is the topography, and g is the acceleration due to gravity. In addition, F is a factor representing the Coulomb-type friction defined as

$$F = -g\ \cos^2\theta\ \tan\delta\ \operatorname{sgn} u \tag{3.3}$$

in the standard Cartesian coordinate system. This Coulomb-type friction is adapted from the one used by Mangeney et al. [41]. For further reference, we use the notations δ for representing the dynamic friction angle, θ for the angle between the topography (bed elevation) and the horizontal line, and w for the quantity $h + z$ called the stage. For our reference, the values $\tan\delta$ and $\tan\theta$ are called the friction slope and bed slope respectively. Note that in the standard Cartesian coordinate system, we limit our discussion to the problems having bed topography $z(x)$ with property $dz/dx = \tan\theta$, where θ is constant.

Following Mangeney et al. [41], we limit our discussion to the case when the friction slope is not larger than the bed slope, that is, $\tan\delta \leq \tan\theta$. With this limitation, after the separating wall is broken, we assume that the fluid motion never stops. Consequently, the Coulomb-type friction (3.3) can be simplified to

$$F = g\ \cos^2\theta\ \tan\delta \tag{3.4}$$

for the debris avalanche problem in the standard Cartesian coordinate system for time $t > 0$.

Taking equation (3.1) into account, we can rewrite equation (3.2) as

$$\frac{\partial u}{\partial t} + u\frac{\partial u}{\partial x} = -g\frac{\partial h}{\partial x} - g\tan\theta + F\,. \tag{3.5}$$

Introducing a "wave speed"[†] defined as

$$c = \sqrt{gh}\,, \tag{3.6}$$

and replacing h by c, we can rewrite equations (3.1) and (3.5) as

$$2\frac{\partial c}{\partial t} + 2u\frac{\partial c}{\partial x} + c\frac{\partial u}{\partial x} = 0\,, \tag{3.7}$$

$$\frac{\partial u}{\partial t} + u\frac{\partial u}{\partial x} + 2c\frac{\partial c}{\partial x} + g\tan\theta - F = 0\,. \tag{3.8}$$

An addition of equation (3.7) to equation (3.8) and subtraction of equation (3.7) from equation (3.8) result in

$$\left\{\frac{\partial}{\partial t} + (u+c)\,\frac{\partial}{\partial x}\right\}\cdot(u + 2c - mt) = 0\,, \tag{3.9}$$

$$\left\{\frac{\partial}{\partial t} + (u-c)\,\frac{\partial}{\partial x}\right\}\cdot(u - 2c - mt) = 0\,, \tag{3.10}$$

respectively, where

$$m = -g\tan\theta + F\,. \tag{3.11}$$

Note that this value of m is assumed to be the horizontal acceleration of a particle sliding down an inclined topography [21, 46].

In other words, equations (3.1) and (3.2) are equivalent to the characteristic relations

$$C_+ : \frac{dx}{dt} = u + c\,, \tag{3.12}$$

$$C_- : \frac{dx}{dt} = u - c\,, \tag{3.13}$$

in which

$$u + 2c - mt = k_+ = \text{constant along each curve } C_+\,, \tag{3.14}$$

$$u - 2c - mt = k_- = \text{constant along each curve } C_-\,, \tag{3.15}$$

where $m = -g\tan\theta + F$ and $c = \sqrt{gh}$, and $k_\pm$ are usually called the Riemann invariants.

[†]Following Stoker [66], we prefer to call c the wave speed (instead of the wave velocity), as it measures the propagation speed of the wave relative to the fluid velocity u. Moreover, the value of c is always nonnegative by definition, whereas the value of velocity could be negative or nonnegative.

3.2.2 Equations in the topography-linked coordinate

In the topography-linked coordinate system, the Saint-Venant model written in the conservative form with a flat topography is

$$\frac{\partial \tilde{h}}{\partial t} + \frac{\partial \left(\tilde{h}\tilde{u}\right)}{\partial \tilde{x}} = 0\,, \tag{3.16}$$

$$\frac{\partial \left(\tilde{h}\tilde{u}\right)}{\partial t} + \frac{\partial \left(\tilde{h}\tilde{u}^2 + \frac{1}{2}g\tilde{h}^2\cos\theta\right)}{\partial \tilde{x}} = -\tilde{h}\left(g\sin\theta - \tilde{F}\right)\,. \tag{3.17}$$

Equations (3.16) and (3.17) are the equation of mass and that of momentum respectively. Here, $\tilde{x}$ represents the coordinate in one-dimensional space, t represents the time variable, $\tilde{u} = \tilde{u}(\tilde{x}, t)$ denotes the fluid velocity, $\tilde{h} = \tilde{h}(\tilde{x}, t)$ denotes the fluid height, θ is the angle between the topography (bed elevation) and the horizontal line, and g is the acceleration due to gravity. In addition, $\tilde{F}$ is a factor representing the Coulomb-type friction, given by

$$\tilde{F} = -g\ \cos\theta\ \tan\delta\ \operatorname{sgn}\tilde{u} \tag{3.18}$$

in this topography-linked coordinate system. Recall that we use the notation δ for representing the dynamic friction angle, and the values $\tan\delta$ and $\tan\theta$ are the friction slope and bed slope respectively.

Again, following Mangeney et al. [41], we limit our discussion to the case when $\tan\delta \leq \tan\theta$, so the Coulomb-type friction is defined by

$$\tilde{F} = g\ \cos\theta\ \tan\delta \tag{3.19}$$

for the debris avalanche problem in the topography-linked coordinate system for time $t > 0$. We use tilde ˜ notation attached in the quantity variables for those variables corresponding to the problem in the topography-linked coordinate system, and the standard quantity variables (without tilde ˜ notation) are used for variables corresponding to the problem in the standard Cartesian coordinate system.

Taking equation (3.16) into account, we can rewrite equation (3.17) as[‡]

$$\frac{\partial \tilde{u}}{\partial t} + \tilde{u}\frac{\partial \tilde{u}}{\partial \tilde{x}} = -g\cos\theta\frac{\partial \tilde{h}}{\partial \tilde{x}} - g\sin\theta + \tilde{F}\,. \tag{3.20}$$

[‡]Equations (1) and (2) in the paper of Mangeney et al. [41] were called "mass and momentum equations". We believe that it was a typographical error (misprint), as in their context, it should be written as "momentum and mass equations".

Introducing a "wave speed" defined as

$$\tilde{c} = \sqrt{g\tilde{h}\cos\theta}\,, \tag{3.21}$$

Mangeney et al. [41] showed that equations (3.16) and (3.20) can be rewritten as

$$2\frac{\partial\tilde{c}}{\partial t} + 2\tilde{u}\frac{\partial\tilde{c}}{\partial\tilde{x}} + \tilde{c}\frac{\partial\tilde{u}}{\partial\tilde{x}} = 0\,, \tag{3.22}$$

$$\frac{\partial\tilde{u}}{\partial t} + \tilde{u}\frac{\partial\tilde{u}}{\partial\tilde{x}} + 2\tilde{c}\frac{\partial\tilde{c}}{\partial\tilde{x}} + g\sin\theta - \tilde{F} = 0\,. \tag{3.23}$$

The value of $\tilde{c}$ is the wave speed relative to the fluid velocity $\tilde{u}$. An addition of (3.22) to (3.23) and subtraction of (3.22) from (3.23) result in

$$\left\{\frac{\partial}{\partial t} + (\tilde{u}+\tilde{c})\,\frac{\partial}{\partial\tilde{x}}\right\}\cdot(\tilde{u} + 2\tilde{c} - \tilde{m}t) = 0\,, \tag{3.24}$$

$$\left\{\frac{\partial}{\partial t} + (\tilde{u}-\tilde{c})\,\frac{\partial}{\partial\tilde{x}}\right\}\cdot(\tilde{u} - 2\tilde{c} - \tilde{m}t) = 0\,, \tag{3.25}$$

respectively, where

$$\tilde{m} = -g\sin\theta + \tilde{F}\,. \tag{3.26}$$

In other words, equations (3.16) and (3.17) are equivalent to the characteristic relations

$$\tilde{C}_+ : \frac{d\tilde{x}}{dt} = \tilde{u} + \tilde{c}\,, \tag{3.27}$$

$$\tilde{C}_- : \frac{d\tilde{x}}{dt} = \tilde{u} - \tilde{c}\,, \tag{3.28}$$

in which

$$\tilde{u} + 2\tilde{c} - \tilde{m}t = \tilde{k}_+ = \text{constant along each curve } \tilde{C}_+\,, \tag{3.29}$$

$$\tilde{u} - 2\tilde{c} - \tilde{m}t = \tilde{k}_- = \text{constant along each curve } \tilde{C}_-\,, \tag{3.30}$$

where $\tilde{m} = -g\sin\theta + \tilde{F}$, and $\tilde{c} = \sqrt{g\tilde{h}\cos\theta}$. Here $\tilde{k}_\pm$ are the Riemann invariants.

From equations (3.12)–(3.15) and (3.27)–(3.30), we see that the problems in the topography-linked coordinate system are analogous to those in the standard Cartesian coordinate system. Therefore, analytical and numerical methods applicable in the standard Cartesian coordinate system are also applicable in the topography-linked coordinate system and vice versa.

To conclude this section, we provide some remarks relating to the Saint-Venant models for debris avalanche problems.

Remark 3.1. The original constant friction term used by Mangeney et al. [41] depends on the internal friction angle δ. It has the property that: if $\delta = \theta$, then the source term in the momentum equation vanishes; if $\delta < \theta$, then the fluid accelerates without bound; and for $\delta > \theta$, the material is brought to rest in finite time. However, note that in our definition of the Coulomb-type friction here, we do not have the same behaviour; that is, δ does not have the same interpretation as a friction angle as the one used by Mangeney et al. [41]. Indeed, following Dressler [21] the acceleration term of Mangeney et al. [41] has been divided by $\cos\theta$, so that it is valid for the shallow water approach.

Remark 3.2. The formulation of the Coulomb-type friction in the standard Cartesian coordinate system is different from that in the topography-linked coordinate system. The discrepancy is due to the differing assumptions that must be made for the systems to be valid. The topography-linked system is valid for a sheet of water on an inclined plane where variations in the depth measured in the normal direction are assumed to be small relative to the wavelength, whereas the standard Cartesian coordinate system is valid when variations on the top surface (measured vertically in standard Cartesian coordinates) are assumed small, as in studying tsunamis or waves on a beach. The two formulations of the Coulomb-type friction tend to agree as $\theta \to 0$.

Remark 3.3. For a topography inclined downwards at angle θ without friction, the shallow water approach implies that the horizontal acceleration of a particle sliding down is $-g\tan\theta$, rather than the true value $-g\sin\theta\cos\theta$. See Dressler [21] for this description. The assumed acceleration $-g\tan\theta$ and the true value $-g\sin\theta\cos\theta$ tend to agree as $\theta \to 0$.

3.3 Existing solutions

We review Ritter's solution to the dam break problem [58] and the solution due to Mangeney, Heinrich, and Roche for the debris avalanche problem [41].

Consider the dam break problem without friction on a horizontal bed in the standard Cartesian coordinate system given in Figure 3.1(a). This problem was solved analytically by Ritter [58] and Stoker [66]. Ritter's solution is

$$u = \frac{2}{3}\left(\frac{x}{t} - c_0\right), \quad h = \frac{1}{9g}\left(\frac{x}{t} + 2c_0\right)^2, \tag{3.31}$$

for $-2c_0t \leq x \leq c_0t$, where $c_0 = \sqrt{gh_0}$.

Mangeney, Heinrich, and Roche (MHR) [41] derived an analytical solution to the debris avalanche problem with friction in the topography-linked coordinate system, as shown in Figure 3.1(b). The MHR solution is

$$\tilde{u} = \frac{2}{3}\left(\frac{\tilde{x}}{t} - \tilde{c}_0 + \tilde{m}t\right), \quad \tilde{h} = \frac{1}{9g\cos\theta}\left(\frac{\tilde{x}}{t} + 2\tilde{c}_0 - \frac{1}{2}\tilde{m}t\right)^2. \tag{3.32}$$

This solution is defined on the interval $-2\tilde{c}_0t + \frac{1}{2}\tilde{m}t^2 < \tilde{x} < \tilde{c}_0t + \frac{1}{2}\tilde{m}t^2$, where $\tilde{m} = -g\sin\theta + \tilde{F}$ and $\tilde{c}_0 = \sqrt{g\tilde{h}_0\cos\theta}$.

3.4 A new solution

In this section, we derive a new analytical solution to the debris avalanche problem in the standard Cartesian coordinate system using two methods, namely, the method of characteristics and a transformation technique.

Although the equations corresponding to the topography-linked coordinate system allow large bottom slopes, due to the initial condition used by Mangeney et al. [41], the MHR solution is accurate only for mild slopes. For steep slopes, soon after the wall given in Figure 3.1(b) is removed, some material around point T_1 would fall down and collapse with some material from around point O moving to the left. This supports the contention that the MHR solution is not accurate for steep slopes.

Here, we derive an analytical solution to a debris avalanche problem with a vertical wall on a sloping topography, as shown in Figure 3.1(c) in the standard Cartesian coordinate system. Our analytical solution is also valid only for small slopes due to the Saint-Venant approach being used. However, the initial condition that we use involves a vertical wall, which is physically more realistic as it is more similar to some real world scenarios [1] than the problem considered by Mangeney et al. [41]. Our derivation utilises properties of the characteristics and follows closely the derivations of Mangeney et al. [41] and Stoker [66].

The debris avalanche (motion) at time $t > 0$ consists of three zones: Zone I is dry (debris free); Zone II has a quadratic free surface; and Zone III has a linear free surface. This is illustrated in Figure 3.2. After the wall is removed, the fluid in Zone III moves with an acceleration a. To be consistent with the approximate nature of our basic equations (3.1) and (3.2) for shallow waves (consult the explanation of Dressler [21]), we take the horizontal acceleration $a = m$.

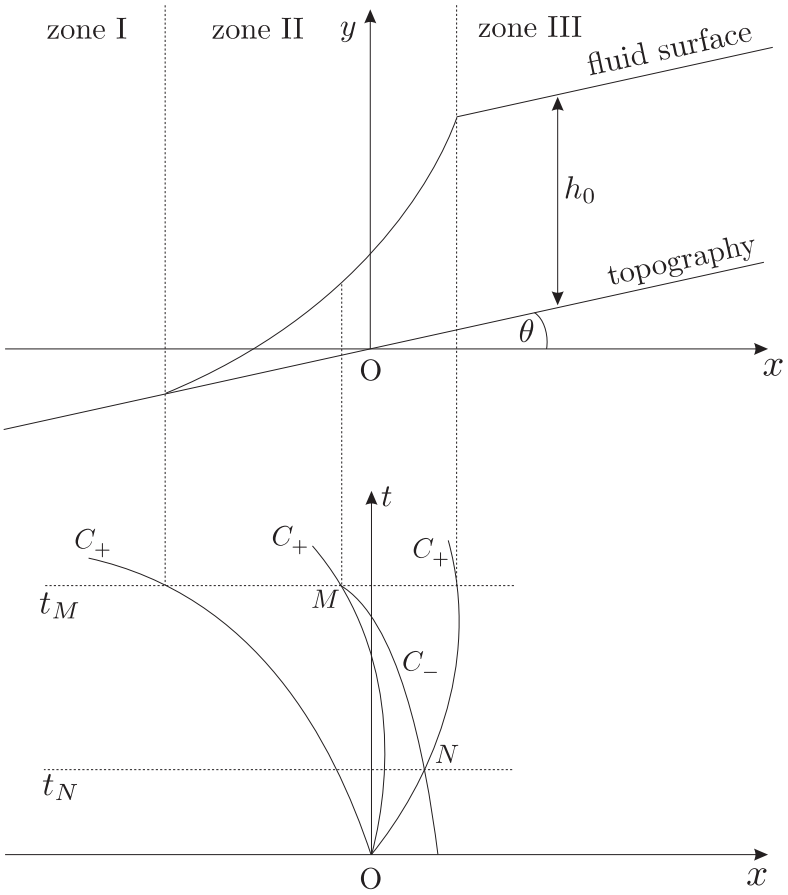

Figure 3.2: A schematic diagram of a debris avalanche and its characteristics at time $t > 0$. The coordinates xy at the top are used to show the fluid surface and the topography. The coordinates xt at the bottom are used to show the characteristic curves, which correspond to the fluid surface.

On the rightmost characteristic curve C_+ emanating from the origin, we have a velocity $u = at$ and relative wave speed $c_0 = \sqrt{gh_0}$. Hence, at any point N on that curve, we have a velocity $u = at_N$ and relative wave speed $c = c_0$ where t_N is the time associated with point N. Now, consider an arbitrary point M in Zone II such that $t_M > t_N$, where t_M is the time of the avalanche associated with point M. Since k_- is constant along characteristic curve C_- passing through points M and N, and we have $a = m$, the velocity at point M is

$$u = 2c - 2c_0 + mt\,, \tag{3.33}$$

where t_M is rewritten as t for simplicity. The slope

$$\frac{dx}{dt} = u + c = 3c - 2c_0 + mt \tag{3.34}$$

is the slope of each characteristic curve C_+ in the rarefaction fan. Since k_+ is constant along each curve defined by $dx/dt = u + c$ and since the velocity u is given by (3.33), the relative wave speed c is constant along each curve in the rarefaction fan. As a result, equation (3.34) can be integrated to obtain

$$c = \frac{1}{3}\left(\frac{x}{t} + 2c_0 - \frac{1}{2}mt\right)\,, \tag{3.35}$$

that is,

$$h = \frac{1}{9g}\left(\frac{x}{t} + 2c_0 - \frac{1}{2}mt\right)^2\,. \tag{3.36}$$

Substituting (3.35) into (3.33), we obtain

$$u = \frac{2}{3}\left(\frac{x}{t} - c_0 + mt\right)\,. \tag{3.37}$$

The fluid height must be nonnegative, so $c \geq 0$, and from (3.35) we have $x \geq -2c_0t + \frac{1}{2}mt^2$. This implies that the track of the front wave is $x = -2c_0t + \frac{1}{2}mt^2$. The tail wave follows the rightmost characteristic curve C_+ emanating from the origin, and satisfies $dx/dt = u + c = at + c_0$. Integrating this differential equation and using $a = m$, we find that the track of the tail wave is $x = c_0t + \frac{1}{2}mt^2$.

In summary, the analytical solution to the debris avalanche problem is (3.37) and (3.36) for $-2c_0t + \frac{1}{2}mt^2 \leq x \leq c_0t + \frac{1}{2}mt^2$.

Alternatively, we can derive (3.37) and (3.36) using a transformation as follows. Substituting the new variables [21, 41, 72]

$$\xi = x - \frac{1}{2}mt^2\,, \quad \tau = t\,, \quad \upsilon = u - mt\,, \quad H = h \tag{3.38}$$

into (3.1) and (3.2), we obtain

$$H_\tau + (\upsilon H)_\xi = 0\,, \tag{3.39}$$

$$(H\upsilon)_\tau + \left(H\upsilon^2 + \frac{1}{2}gH^2\right)_\xi = 0\,. \tag{3.40}$$

Therefore, for a given initial condition, if the solution to (3.39) and (3.40) is

$$\upsilon = \upsilon(\xi,\tau) \quad \text{and} \quad H = H(\xi,\tau)\,, \tag{3.41}$$

then the solution to (3.1) and (3.2) is

$$u(x,t) = \upsilon\left(\xi,t\right) + mt \quad \text{and} \quad h(x,t) = H\left(\xi,t\right)\,. \tag{3.42}$$

Employing this transformation together with Ritter's solution given in Section 3.3 reproduces the solution (3.37) and (3.36).

Before we proceed to the numerical tests, we provide some remarks relating to the validity of the MHR and the new solutions.

Remark 3.4. The MHR solution is not valid for a steep slope because of the initial condition, which makes the dam-wall overhang. The new solution is not valid for a steep slope because of the shallow water approach, which assumes that the vertical acceleration is negligible.

Remark 3.5. The new solution is derived with friction, which is included in the definition of m. Note that the new solution is also valid for avalanche problems without friction, by setting that the friction factor equals zero.

3.5 Numerical tests

In this section, we utilise our analytical solution to test a finite volume method (FVM) used to solve the Saint-Venant model. We use the Python 2.4 software and adapt the ANUGA package[§] for programming.

Audusse et al. [2] established that in order to resolve the solution accurately at wet/dry interfaces, and to ensure that the FVM is well-balanced, stage $w := h+z$ and height h should be reconstructed. This has been verified in Chapter 2. Therefore, we consider two methods with reconstruction based on stage w and height h.

[§]http://anuga.anu.edu.au/

Table 3.1: Numerical settings in the simulations.

Description	Specification
Units of the measured quantities	SI system
Acceleration g due to gravity	9.81
Minimum height allowed in the flux computation	10^{-6}
Limiter for quantity reconstruction	minmod
Courant–Friedrichs–Lewy number	1.0
Error quantification (see equation (2.12))	discrete L^1
Spatial domain	$[-1000, 1000]$
Initial fluid height h_0 on the right of the wall	20

We compare the performance of the FVM with reconstruction based on stage w, height h, and velocity u to that of the FVM with reconstruction based on stage w, height h, and momentum $p := hu$ in solving the debris avalanche problem. For further reference in this section, we call the FVM with reconstruction based on stage w, height h, and velocity u as Method A and the FVM with reconstruction based on stage w, height h, and momentum p as Method B. Note that the terms "Method A" and "Method B" are introduced for simplicity in this chapter and the next one (Chapter 4). These methods are different from "Method A" and "Method B" in Chapter 2.

In all simulations, the specification follows from our previous work in Chapter 2, except for the initial fluid height h_0. We use the well-balanced finite volume scheme presented in Chapter 2, but note that here we have an additional friction source. The discretisation of the friction term hF included in the source at the ith cell is $h_i F$, where h_i is the value of the numerical height at the centroid of the cell. That is, the first and second order numerical source terms are

$$\mathbf{S}_i^{(1)} := \begin{bmatrix} 0 \\ h_i F \end{bmatrix} \quad \text{and} \quad \mathbf{S}_i^{(2)} := \begin{bmatrix} 0 \\ -g\frac{h_{i,r}+h_{i,l}}{2}(z_{i,r} - z_{i,l}) + h_i F \end{bmatrix}, \tag{3.43}$$

where F is defined by (3.3). We limit our simulations to second order spatial and second order temporal discretisations, which is followed by the use of the second order numerical source term. The central upwind flux formulation proposed by Kurganov, Noelle, and Petrova [36] is used to compute the numerical fluxes. The details of the numerical settings are given in Table 3.1.

We have assumed that $\tan\delta \leq \tan\theta$. Consequently, we have three possible

test cases: $0 = \tan\delta = \tan\theta$; $0 = \tan\delta < \tan\theta$; and $0 < \tan\delta \leq \tan\theta$. One representative of each case is considered.

1. First, we test the numerical methods for a problem with friction slope $\tan\delta = 0$ and bed slope $\tan\theta = 0$. The errors for stage w and momentum p with various numbers of cells are presented in Table 3.2. Figure 3.3 illustrates the exact solution of the free fluid surface (stage) at several instants in time for this first case ($t = 0, 5, 10, 15, 20, 25, 30$).

2. Second, we consider a problem with friction slope $\tan\delta = 0$ and bed slope $\tan\theta = 0.1$. The errors for stage w and momentum p with various numbers of cells are presented in Table 3.3. Figure 3.4 illustrates the exact solution of the free fluid surface at several instants in time for this second case ($t = 0, 5, 10, 15, 20, 25, 30$).

3. Finally, for the third case we consider a problem with friction slope $\tan\delta = 0.05$ and bed slope $\tan\theta = 0.1$. The errors for stage w and momentum p with various number of cells are presented in Table 3.4. For this third case, Figure 3.5 shows the debris avalanche consisting of stage w and momentum p at time $t = 15$ using Method B with 800 cells.

Movies of the simulations using Method B are given in the supplementary files[¶] *dam-break.avi*, *avalanche-frictionless.avi*, and *avalanche-friction.avi* respectively for the first, second, and third case simulated with 800 cells for time $t \in [0, 15]$. Method A leads to similar results and movies.

According to Tables 3.2–3.4, as the cell length is halved, the errors produced by the FVMs are halved. This suggests that we have only first order of convergence, even though we have used second order methods. The reason is that a large error occurs around the front wave at the wet/dry interface; this is called the wet/dry interface problem. This problem was also identified in the simulations of Mangeney et al. [41]. Diffusion is also found around the tail wave, but it is not as significant as that around the wet/dry interface. Based on Tables 3.2–3.4, the error produced by Method B is slightly smaller than the error produced by Method A in solving the debris avalanche problem. (The source of discrepancy of the errors produced by Methods A and B is not clear, but the discrepancy seems caused by round-off errors due to different numerical treatments of the methods.)

[¶]The supplementary files are available at `http://journal.austms.org.au/ojs/index.php/ANZIAMJ/rt/suppFiles/3785/0`.

Table 3.2: Errors for $\tan\delta = 0$ and $\tan\theta = 0$ at $t = 15$.

Number	w error		p error	
of cells	A	B	A	B
100	0.1074	0.1010	1.5234	1.4212
200	0.0511	0.0499	0.7162	0.7067
400	0.0254	0.0250	0.3537	0.3556
800	0.0127	0.0125	0.1771	0.1785
1600	0.0063	0.0063	0.0887	0.0894

Table 3.3: Errors for $\tan\delta = 0$ and $\tan\theta = 0.1$ at $t = 15$.

Number	w error		p error	
of cells	A	B	A	B
100	0.1121	0.1006	1.8559	1.5028
200	0.0534	0.0501	0.8445	0.7428
400	0.0257	0.0250	0.3885	0.3695
800	0.0128	0.0126	0.1919	0.1846
1600	0.0064	0.0063	0.0956	0.0925

Table 3.4: Errors for $\tan\delta = 0.05$ and $\tan\theta = 0.1$ at $t = 15$.

Number	w error		p error	
of cells	A	B	A	B
100	0.1092	0.1010	1.4858	1.2775
200	0.0527	0.0504	0.6924	0.6402
400	0.0256	0.0251	0.3285	0.3204
800	0.0128	0.0126	0.1640	0.1611
1600	0.0064	0.0063	0.0823	0.0810

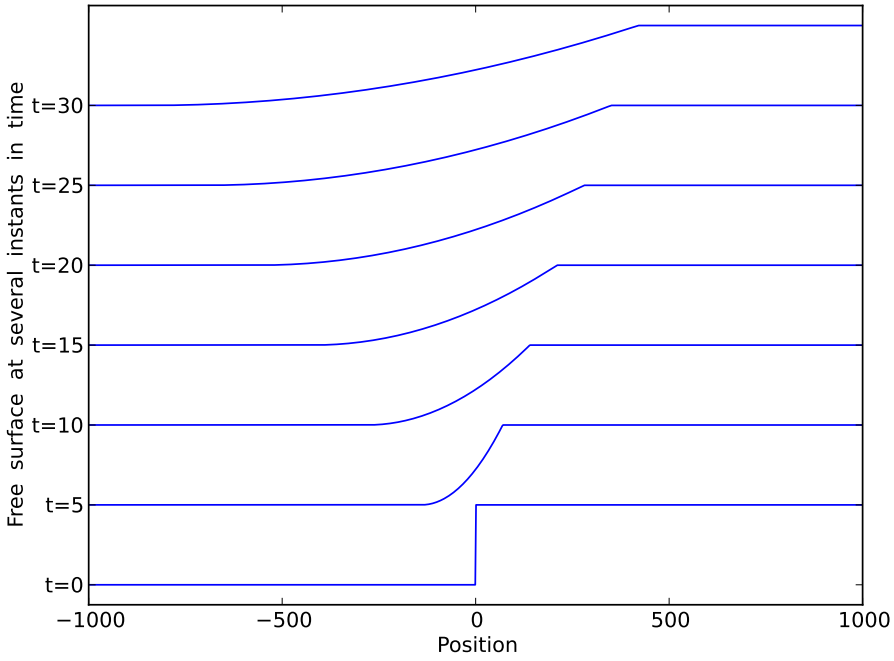

Figure 3.3: Free surface for several instants in time for the dam break problem without friction. From the bottom to the top are the free surfaces at $t = 0, 5, 10, 15, 20, 25, 30$ respectively.

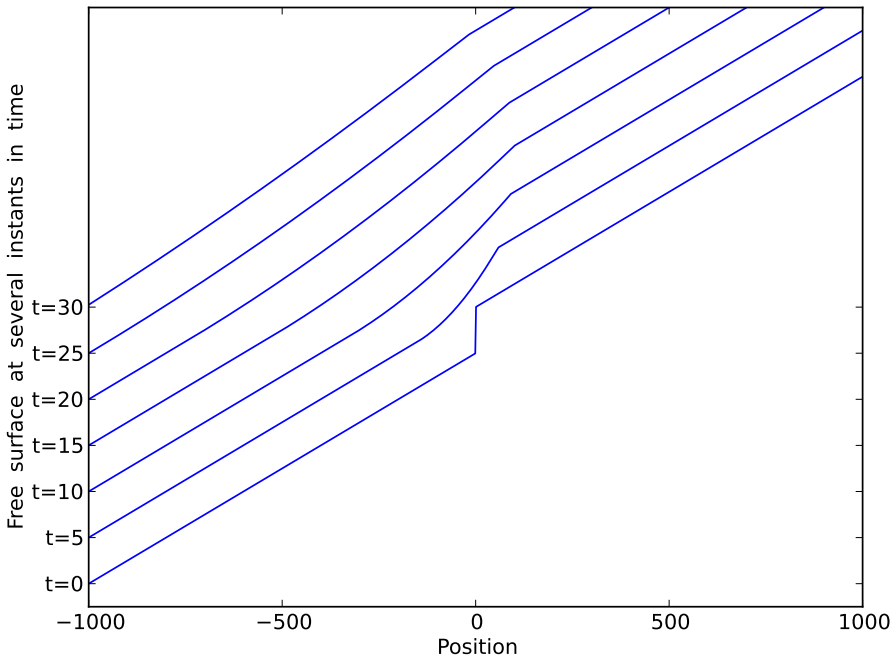

Figure 3.4: Free surface for several instants in time for the avalanche problem without friction. From the bottom to the top are the free surfaces at $t = 0, 5, 10, 15, 20, 25, 30$ respectively.

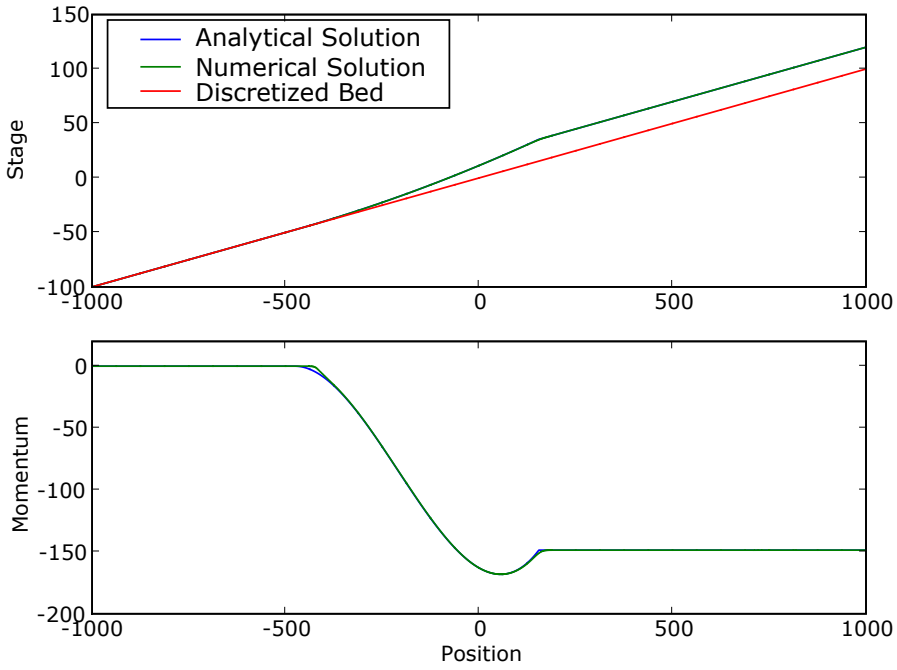

Figure 3.5: Avalanche with $\tan\delta = 0.05$, $\tan\theta = 0.1$, at $t = 15$. The subfigure at the top shows the stage (free surface) and the topography. The subfigure at the bottom shows the momentum, which corresponds to the free surface.

3.6 Concluding remarks

A new analytical solution has been derived and can be used to test the performance of finite volume methods. We have used a Saint-Venant approach in the standard Cartesian coordinate system to solve the debris avalanche problem with friction. The drawback of the Saint-Venant approach is that the solution is not physically valid for a very steep sloping topography.

The debris avalanche problem discussed in this chapter does not involve shock waves. In the next chapter, we shall derive a new analytical solution to debris avalanche problems involving shock waves.

This page was intentionally left blank.

Chapter 4

Avalanche involving a shock*

4.1 Introduction

In the previous chapter (Chapter 3), we derived solutions to debris avalanche problems only for cases involving wet and dry regions, that is, one region either on the left or right to the separating wall is dry, and no discontinuous solution was involved. However, it is well-known that because the model is hyperbolic, the Saint-Venant model admits a discontinuous solution called a bore or shock (shock wave) or hydraulic jump. This was also stated by Mangeney et al. [41], which means that the study of debris avalanche problems using a Saint-Venant approach will be complete if a shock is included.

Therefore, in this chapter we consider problems on inclined slopes involving wet and wet regions, that is, both regions on the left and right to the initially separating wall are wet. With this setting, a shock will be formed as time evolves [66]. We apply the method of characteristics and a transformation technique to obtain the analytical solution to the debris avalanche problem involving a shock.

Two problems are considered. The first is the debris avalanche problem in the standard Cartesian coordinate system, as shown in Figure 4.1, and the second is the debris avalanche problem in the topography-linked coordinate system, as shown in Figure 4.2. We derive the analytical solutions to both problems having still state initially (zero initial velocity). Assuming that h_1 and h_0 are nonnegative representing the fluid heights on the left and right respectively of the separating wall given initially, we see that these two problems are generalisations of those solved by Stoker [65, 66] and Mangeney et al. [41]. They are also generalisations

*The results of this chapter have been published [48].

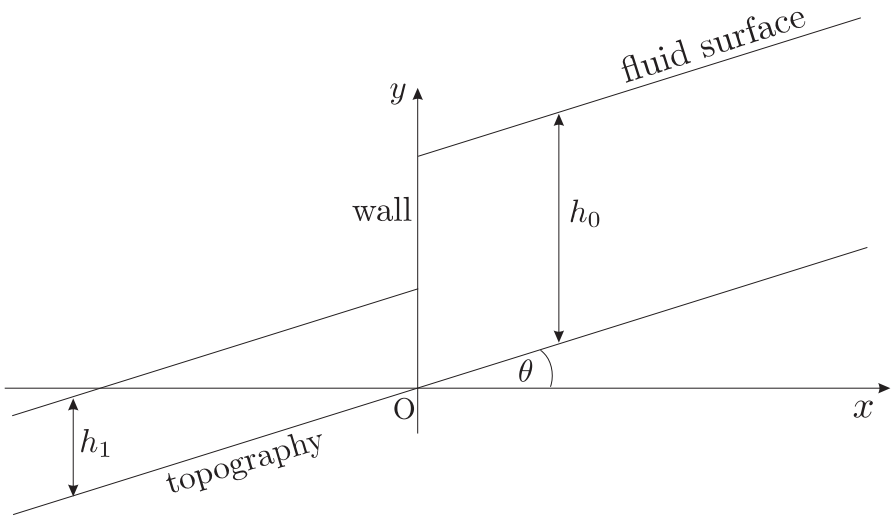

Figure 4.1: Initial profile of the debris avalanche problem in the standard Cartesian coordinate system.

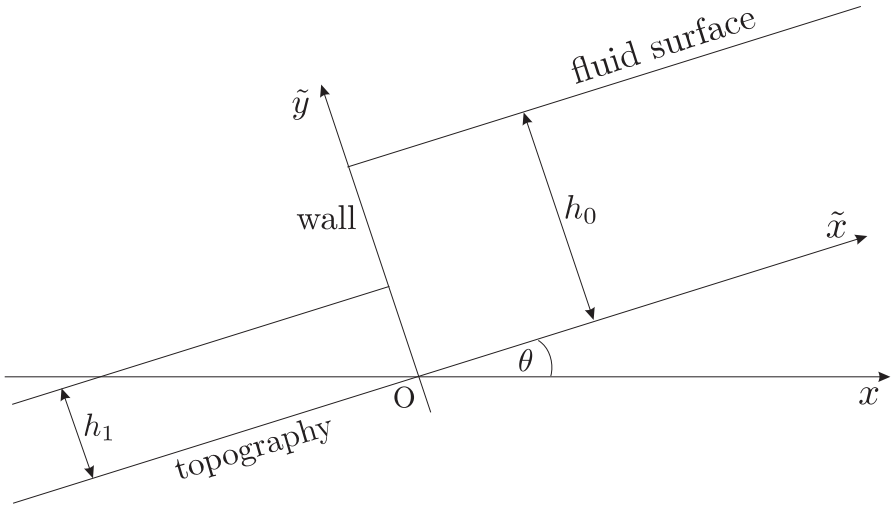

Figure 4.2: Initial profile of the debris avalanche problem in the topography-linked coordinate system.

of the problems solved in Chapter 3. Note that for the case with a horizontal topography, these two problems coincide and Stoker [65, 66] has already solved it; for the case with an inclined topography and $h_1 = 0$ in the topography-linked coordinate system, Mangeney et al. [41] have proposed a solution; the case with an inclined topography and $h_1 = 0$ in the standard Cartesian coordinate system has been solved in Chapter 3.

The remainder of this chapter is organised as follows. Section 4.2 derives the analytical solution of the corresponding debris avalanche problem in the standard Cartesian coordinate system, and presents the properties of the analytical solution. Section 4.3 briefly derives the analytical solution of the debris avalanche problem in the topography-linked coordinate system. In Section 4.4, we use the analytical solution in the standard Cartesian coordinate system to test debris avalanche numerical models. Finally, some concluding remarks are provided in Section 4.5.

4.2 A new solution in the standard Cartesian system

In this section, we shall derive the solution to the debris avalanche problem using characteristics and a transformation, and present the properties of the solution. Our derivation follows the work of Dressler [21], Mangeney et al. [41], and Stoker [66].

4.2.1 Derivation of the analytical solution

Recall the debris avalanche problem shown in Figure 4.1. The method of characteristics for the Saint-Venant model is actually an adaptation of the method implemented by Courant and Friedrich [17] in studying gas dynamics.

Figure 4.1 illustrates the fluid profile at time $t = 0$, while Figure 4.3 shows the fluid motion and its characteristics at time $t > 0$. Note that Figure 4.3 is a schematic illustration of the flow adapted from the work of Stoker [66] and Mangeney et al. [41]. At time $t = 0$, there exists only two regions: Zone (1) has a linear surface with height h_1 on the left of the separating wall; and Zone (0) has a linear surface with height h_0 on the right. At time $t > 0$, four regions exists: Zone (1) is the linear surface with a constant height h_1; Zone (2) is another linear

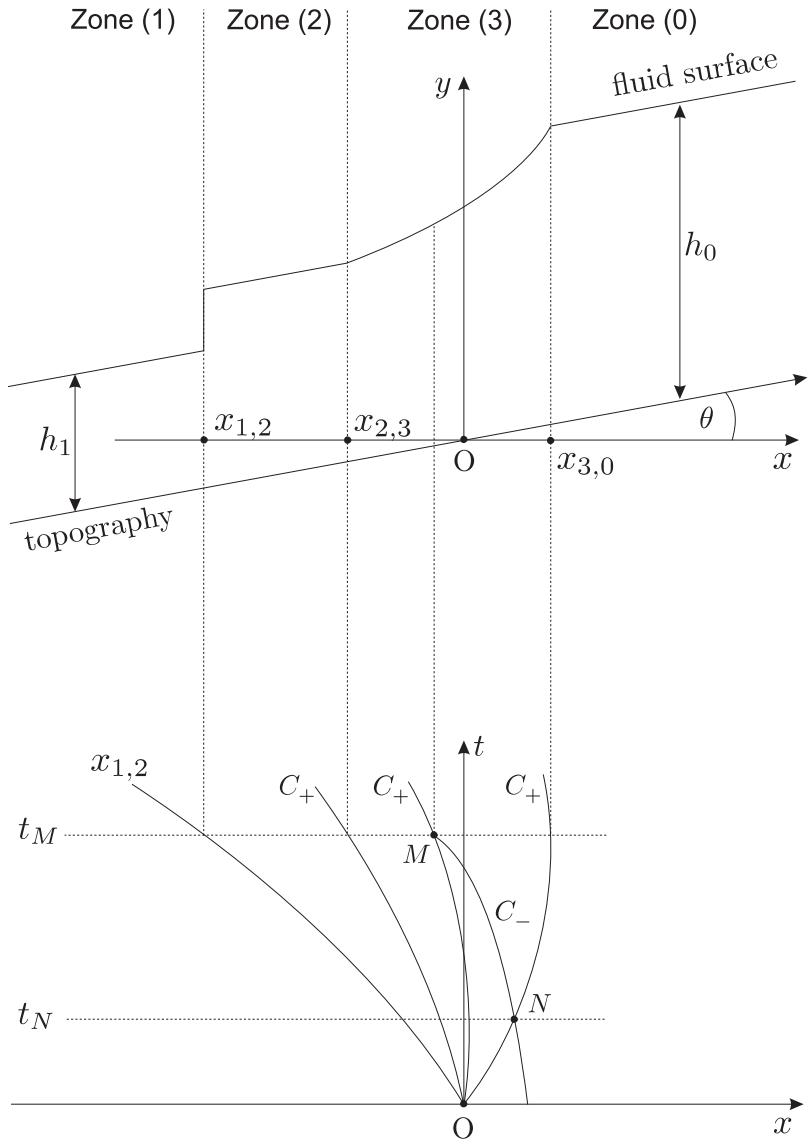

Figure 4.3: A schematic profile of the debris avalanche problem involving a shock in the standard Cartesian coordinate system and their corresponding characteristic curves.

surface with constant height h_2 ; Zone (3) has a quadratic surface with height h_3 ; and Zone (0) is the linear surface with height h_0 . For time $t > 0$, we name $x_{1,2}$ as the point separating Zone (1) and Zone (2); $x_{2,3}$ as the point separating Zone (2) and Zone (3); and similarly $x_{3,0}$ separating Zone (3) and Zone (0). Zones (1) and (0) are the quiet regions, that is, the fluid is affected only by the acceleration due to gravity and remains unaffected by disturbance. Zones (2) and (3) are the disturbance regions, where the solutions in terms of height h and velocity u need to be found.

For further reference, we use the following conventions. For an arbitrary value of m , we use notations in Zones (1), (3), and (0) as follows: the velocity, height, and wave speed are denoted respectively by u_i , h_i , and c_i , where $i = 1, 3, 0$; the subscripts of the variables represent the name of the zone. For Zone (2), we denote the velocity, height, and wave speed by u_2 , h_2 , and c_2 only for the case when $m = 0$, and we state those quantities explicitly if we have $m \neq 0$. In addition, still in Zone (2), the shock velocity is denoted by σ only for the case when $m = 0$, and we also state it explicitly if the case is $m \neq 0$. Note that the shock position is exactly at the interface between Zones (1) and (2).

Recall that Zones (1) and (0) are the quiet regions, that is, the fluid is affected only by the acceleration due to gravity. Therefore, the heights at Zones (1) and (0) remain h_1 and h_0 respectively, and their corresponding velocities are the same value given by $u_1 = u_0 = mt$.

The solution at Zone (3) having a quadratic profile is derived in a similar way to our previous work in Chapter 3. On the rightmost characteristic curve C_+ emanating from the origin, we have a velocity $u = at$ and relative wave speed $c_0 = \sqrt{gh_0}$. Hence, at arbitrary point N on that curve, we have a velocity $u = at_N$ and relative wave speed $c = c_0$ where t_N is the time associated with point N . Now consider an arbitrary point M in Zone II such that $t_M > t_N$, where t_M is the time associated with point M . Since k_- is constant along characteristic curve C_- passing through points M and N , and we have $a = m$, the velocity at point M is

$$u = 2c - 2c_0 + mt \,, \tag{4.1}$$

where t_M is rewritten as t for simplicity. The slope

$$\frac{dx}{dt} = u + c = 3c - 2c_0 + mt \tag{4.2}$$

is the slope of each characteristic curve C_+ in the rarefaction fan. Since k_+ is

constant along each curve defined by $dx/dt = u + c$ and since the velocity u is given by (4.1), the relative wave speed c is constant along each curve in the rarefaction fan. As a result, equation (4.2) can be integrated to give

$$c = \frac{1}{3}\left(\frac{x}{t} + 2c_0 - \frac{1}{2}mt\right) , \tag{4.3}$$

that is,

$$h = \frac{1}{9g}\left(\frac{x}{t} + 2c_0 - \frac{1}{2}mt\right)^2 . \tag{4.4}$$

Substituting (4.3) into (4.1), we obtain

$$u = \frac{2}{3}\left(\frac{x}{t} - c_0 + mt\right) . \tag{4.5}$$

The position of $x_{3,0}$ is characterised by

$$\frac{dx}{dt} = u_0 + c_0 = mt + c_0 . \tag{4.6}$$

Therefore, $x_{3,0} = c_0 t + \frac{1}{2}mt^2$.

Suppose that we have $m = 0$, so we have the classical dam break problem. The solution at Zone (2) is derived as follows. After the separating wall is removed ($t > 0$), a shock occurs. The shock position is at $x_{1,2}$, at the interface between Zone (1) and Zone (2). Let us denote the shock velocity as σ , which is a constant, so that the shock position is $x_{1,2} = \sigma t$ at time t . The shock conditions[†] are [66]

$$-\sigma\,(u_2 - \sigma) = \frac{1}{2}\left(c_1^2 + c_2^2\right) , \tag{4.7}$$

$$c_2^2\,(u_2 - \sigma) = -c_1^2\sigma . \tag{4.8}$$

Using equation (4.8), we eliminate c_2^2 from equation (4.7) resulting in the quadratic equation

$$\sigma\,(u_2 - \sigma)^2 + \frac{1}{2}c_1^2\,(u_2 - \sigma) - \frac{1}{2}c_1^2\sigma = 0 . \tag{4.9}$$

From this quadratic equation, we have

$$u_2 = \sigma - \frac{c_1^2}{4\sigma}\left(1 + \sqrt{1 + 8\left(\frac{\sigma}{c_1}\right)^2}\right) , \tag{4.10}$$

[†]These shock conditions were derived by Stoker [66] for the case when the topography is horizontal. In fact, the shock conditions for arbitrary shape of topography are still the same as long as the topography is continuous, as proved by Dressler [20].

in which the positive sign (instead of the negative) in front of the square root is chosen such that $u_2 - \sigma$ and $-\sigma$ have the same sign. This same sign guarantees that Zone (2) expands out as time t evolves. Using equation (4.7), we eliminate u_2 from equation (4.34) to obtain

$$c_2 = c_1 \sqrt{\frac{1}{2}\left(\sqrt{1 + 8\left(\frac{\sigma}{c_1}\right)^2} - 1\right)}\,. \tag{4.11}$$

The shock conditions (4.7) and (4.8) now become (4.10) and (4.11). We see that there exists infinitely many solutions satisfying (4.10) and (4.11), as there are three unknowns namely u_2 , c_2 , and σ , but only two equations are given. To get a unique set of solutions, we need one more equation. The other equation is found by observing the characteristic curve passed by $x_{2,3}$. Recall that k_- is constant along each characteristic curve C_- . Therefore,

$$u - 2c - mt = -2c_0 \tag{4.12}$$

over the whole Zone (3), and

$$u - 2c - mt = u_2 - 2c_2 \tag{4.13}$$

at point $x_{2,3}$. As a result, we have

$$-2c_0 = u_2 - 2c_2 \tag{4.14}$$

at point $x_{2,3}$. Therefore, u_2 , c_2 , and σ are found by solving three simultaneous equations (4.10), (4.11), and (4.14).

Now if $m \neq 0$, at Zone (2), the quantities u_2 and σ defined for $m = 0$ described above must be corrected for the fluid velocity and shock velocity. Recall that the constant m is the horizontal acceleration of a particle sliding down an inclined topography. This implies that the fluid velocity and shock velocity at Zone (2) is $u_2 + mt$ and $\sigma + mt$ respectively. The position of $x_{2,3}$ is then characterised by

$$\frac{dx}{dt} = (u_2 + mt) + c_2\,, \tag{4.15}$$

which implies that $x_{2,3} = (u_2 + c_2)t + \frac{1}{2}mt^2$. In addition, the shock position is $x_{1,2} = \sigma t + \frac{1}{2}mt^2$.

Therefore, the solution to the debris avalanche problem in the standard Cartesian coordinate system is

$$h(x,t) = \begin{cases} h_1 & \text{if } x < \sigma t + \frac{1}{2}mt^2\,, \\ h_2 & \text{if } \sigma t + \frac{1}{2}mt^2 \le x < (u_2 + c_2)t + \frac{1}{2}mt^2\,, \\ \frac{1}{9g}\left(\frac{x}{t} + 2c_0 - \frac{1}{2}mt\right)^2 & \text{if } (u_2 + c_2)t + \frac{1}{2}mt^2 \le x < c_0 t + \frac{1}{2}mt^2\,, \\ h_0 & \text{if } x \ge c_0 t + \frac{1}{2}mt^2\,, \end{cases} \tag{4.16}$$

and

$$u(x,t) = \begin{cases} mt & \text{if } x < \sigma t + \frac{1}{2}mt^2\,, \\ u_2 + mt & \text{if } \sigma t + \frac{1}{2}mt^2 \le x < (u_2 + c_2)t + \frac{1}{2}mt^2\,, \\ \frac{2}{3}\left(\frac{x}{t} - c_0 + mt\right) & \text{if } (u_2 + c_2)t + \frac{1}{2}mt^2 \le x < c_0 t + \frac{1}{2}mt^2\,, \\ mt & \text{if } x \ge c_0 t + \frac{1}{2}mt^2\,, \end{cases} \tag{4.17}$$

for time $t > 0$. Here u_2, c_2, and σ are the solutions of the three simultaneous equations (4.10), (4.11), and (4.14). The value of h_2 is calculated using relation $c_2 = \sqrt{gh_2}$.

Alternatively, we can implement a transformation technique to obtain the solution to the debris avalanche problem by recalling the solution to the classical dam break problem. The solution, where $m = 0$ and $h_0 > h_1$, is [66]

$$h(x,t) = \begin{cases} h_1 & \text{if } x < \sigma t\,, \\ h_2 & \text{if } \sigma t \le x < (u_2 + c_2)t \\ \frac{1}{9g}\left(\frac{x}{t} + 2c_0\right)^2 & \text{if } (u_2 + c_2)t \le x < c_0 t\,, \\ h_0 & \text{if } x \ge c_0 t\,, \end{cases} \tag{4.18}$$

and

$$u(x,t) = \begin{cases} 0 & \text{if } x < \sigma t\,, \\ u_2 & \text{if } \sigma t \le x < (u_2 + c_2)t\,, \\ \frac{2}{3}\left(\frac{x}{t} - c_0\right) & \text{if } (u_2 + c_2)t \le x < c_0 t\,, \\ 0 & \text{if } x \ge c_0 t\,, \end{cases} \tag{4.19}$$

for time $t > 0$. Here u_2, c_2, and σ are the solutions of the three simultaneous equations (4.10), (4.11), and (4.14). The value of h_2 is calculated using relation $c_2 = \sqrt{gh_2}$. Let us now recall the transformation technique used in Chapter 3 as follows. We consider the Saint-Venant model in the standard Cartesian coordinate system, (3.1) and (3.2), and denote that $m = -g\tan\theta + F$ and $c = \sqrt{gh}$. Introducing the new variables [21, 41, 72]

$$\xi = x - \frac{1}{2}mt^2\,, \quad \tau = t\,, \quad \upsilon = u - mt\,, \quad H = h \tag{4.20}$$

into (3.1) and (3.2), we obtain

$$H_\tau + (\upsilon H)_\xi = 0\,, \tag{4.21}$$

$$(H\upsilon)_\tau + \left(H\upsilon^2 + \frac{1}{2}gH^2\right)_\xi = 0\,. \tag{4.22}$$

Therefore for a given initial condition, if the solution to (4.21) and (4.22) is

$$\upsilon = \upsilon(\xi,\tau)\,, \quad \text{and} \quad H = H(\xi,\tau) \tag{4.23}$$

then the solution to (3.1) and (3.2) is

$$u(x,t) = \upsilon\,(\xi,t) + mt\,, \quad \text{and} \quad h(x,t) = H\,(\xi,t)\ . \tag{4.24}$$

Consequently, the solution to the debris avalanche problem shown in Figure 4.1, where $h_0 > h_1$, is (4.16) and (4.17) for time $t > 0$.

4.2.2 Properties of the analytical solution

Here we provide three properties of the analytical solution (4.16) and (4.17) we have derived to the debris avalanche problem following the properties of the solution to the dam break problem presented by Stoker [66].

The first is the property of the solution at point $x = \frac{1}{2}mt^2$. If

$$u_2 + c_2 + mt \le 0\,, \tag{4.25}$$

this point $x = \frac{1}{2}mt^2$ belong to Zone (3), and we have that at this point the fluid height, velocity, and momentum are

$$h = \frac{4}{9}h_0\,, \quad u = -\frac{2}{3}c_0\,, \quad p = -\frac{8}{27}h_0c_0\,, \tag{4.26}$$

respectively. If

$$u_2 + c_2 + mt > 0\,, \tag{4.27}$$

the point $x = \frac{1}{2}mt^2$ belong to Zone (2), and we see that the fluid height, velocity, and momentum at this point are

$$h = h_2\,, \quad u = u_2 + mt\,, \quad p = h_2(u_2 + mt)\,, \tag{4.28}$$

respectively.

The second is the height of the shock, measured by $h_2 - h_1$. The height of the shock is zero when $h_1 = 0$ or $h_1 = h_0$, and it attains its maximum $h_2 - h_1 = 0.32h_0$ when $h_1/h_0 = 0.176$, as described by Stoker [66].

The third is the behavior of the solution when $h_1 = h_0$ or $h_1 = 0$. Recalling the solution given by (4.16) and (4.17), and its illustration in Figure 4.3, we describe the behavior as follows. When $h_1 = h_0$, "the height of the shock is zero" corresponds to the fact that the shock speed σ equals the value of the fluid velocity upstream u_0. At the same time, Zone (3) disappears, as the width of Zone (3) is zero. We note that when $h_1 = h_0$, what happens is just a block of fluid sliding downstream with a constant height h_0 and velocity $u = mt$. For the other case, when $h_1 = 0$, the analytical solution (4.16) and (4.17) becomes:

$$h(x,t) = \begin{cases} 0 & \text{if } x < -2c_0t + \frac{1}{2}mt^2\,, \\ \frac{1}{9g}\left(\frac{x}{t} + 2c_0 - \frac{1}{2}mt\right)^2 & \text{if } -2c_0t + \frac{1}{2}mt^2 \le x < c_0t + \frac{1}{2}mt^2\,, \\ h_0 & \text{if } x \ge c_0t + \frac{1}{2}mt^2\,, \end{cases} \tag{4.29}$$

and

$$u(x,t) = \begin{cases} 0 & \text{if } x < -2c_0t + \frac{1}{2}mt^2\,, \\ \frac{2}{3}\left(\frac{x}{t} - c_0 + mt\right) & \text{if } -2c_0t + \frac{1}{2}mt^2 \le x < c_0t + \frac{1}{2}mt^2\,, \\ mt & \text{if } x \ge c_0t + \frac{1}{2}mt^2\,, \end{cases} \tag{4.30}$$

that is, we recover the analytical solution derived in Chapter 3 to the debris avalanche problem involving a dry bed in the standard Cartesian coordinate system. When $h_1 = 0$, we say that there is not a shock in the solution. This is because when $h_1 = 0$, Zone (2) is squeezed out into one point, which is the interface between wet and dry areas, and the dry area is always reached by the rarefaction wave.

4.3 A new solution in the topography-linked system

Consider the debris avalanche problem in the topography-linked coordinate system shown in Figure 4.2. In this section, we briefly derive the analytical solution to the problem.

Because the debris avalanche problem in the topography-linked coordinate system is analogous to that in the standard Cartesian coordinate system (see

Subsections 3.2.1 and 3.2.2), methods applicable in the standard Cartesian coordinate system are also applicable in the topography-linked coordinate system. Therefore, we can use either the method of characteristics or a transformation technique to solve the debris avalanche problem in the topography-linked coordinate system. For brevity, we solve the problem using a transformation.

Recall the solution (4.18) and (4.19) to the classical dam break problem. Introducing the new variables

$$\tilde{\xi} = \tilde{x} - \frac{1}{2}\tilde{m}t^2\,, \quad \tau = t\,, \quad \tilde{v} = \tilde{u} - \tilde{m}t\,, \quad \tilde{H} = \tilde{h} \tag{4.31}$$

into (3.16) and (3.17), we can solve the problem in the transformed coordinate. The solution is then transformed back to the original topography-linked coordinate so that the solution to the debris avalanche problem shown in Figure 4.2, where $\tilde{h}_0 > \tilde{h}_1$, is

$$\tilde{h}(\tilde{x},t) = \begin{cases} \tilde{h}_1 & \text{if } \tilde{x} < \tilde{\sigma}t + \frac{1}{2}\tilde{m}t^2\,, \\ \tilde{h}_2 & \text{if } \tilde{\sigma}t + \frac{1}{2}\tilde{m}t^2 \le \tilde{x} < (\tilde{u}_2 + \tilde{c}_2)t + \frac{1}{2}\tilde{m}t^2\,, \\ \frac{1}{9g\cos\theta}\left(\frac{\tilde{x}}{t} + 2\tilde{c}_0 - \frac{1}{2}\tilde{m}t\right)^2 & \text{if } (\tilde{u}_2 + \tilde{c}_2)t + \frac{1}{2}\tilde{m}t^2 \le \tilde{x} < \tilde{c}_0 t + \frac{1}{2}\tilde{m}t^2\,, \\ \tilde{h}_0 & \text{if } \tilde{x} \ge \tilde{c}_0 t + \frac{1}{2}\tilde{m}t^2\,, \end{cases} \tag{4.32}$$

and

$$\tilde{u}(\tilde{x},t) = \begin{cases} \tilde{m}t & \text{if } \tilde{x} < \tilde{\sigma}t + \frac{1}{2}\tilde{m}t^2\,, \\ \tilde{u}_2 + \tilde{m}t & \text{if } \tilde{\sigma}t + \frac{1}{2}\tilde{m}t^2 \le \tilde{x} < (\tilde{u}_2 + \tilde{c}_2)t + \frac{1}{2}\tilde{m}t^2\,, \\ \frac{2}{3}\left(\frac{\tilde{x}}{t} - \tilde{c}_0 + \tilde{m}t\right) & \text{if } (\tilde{u}_2 + \tilde{c}_2)t + \frac{1}{2}\tilde{m}t^2 \le \tilde{x} < \tilde{c}_0 t + \frac{1}{2}\tilde{m}t^2\,, \\ \tilde{m}t & \text{if } \tilde{x} \ge \tilde{c}_0 t + \frac{1}{2}\tilde{m}t^2\,, \end{cases} \tag{4.33}$$

for time $t > 0$. Here $\tilde{u}_2$, $\tilde{c}_2$, and $\tilde{\sigma}$ are the solutions of the three simultaneous equations

$$\tilde{u}_2 = \tilde{\sigma} - \frac{\tilde{c}_1^2}{4\tilde{\sigma}}\left(1 + \sqrt{1 + 8\left(\frac{\tilde{\sigma}}{\tilde{c}_1}\right)^2}\right), \tag{4.34}$$

$$\tilde{c}_2 = \tilde{c}_1\sqrt{\frac{1}{2}\left(\sqrt{1 + 8\left(\frac{\tilde{\sigma}}{\tilde{c}_1}\right)^2} - 1\right)}, \tag{4.35}$$

$$-2\tilde{c}_0 = \tilde{u}_2 - 2\tilde{c}_2 \tag{4.36}$$

where $\tilde{m} = -g\sin\theta + \tilde{F}$. Note that $\tilde{c}_i = \sqrt{g\tilde{h}_i\cos\theta}$, $i = 1, 2, 3, 0$. The value of $\tilde{h}_2$ is calculated using relation $\tilde{c}_2 = \sqrt{g\tilde{h}_2\cos\theta}$.

The properties of this solution are similar to those of the solution to the debris avalanche problem in the standard Cartesian coordinate system. In particular, if $\tilde{h}_1 = 0$, the analytical solution (4.32) and (4.33) becomes:

$$\tilde{h}(\tilde{x},t) = \begin{cases} \tilde{h}_1 & \text{if } \tilde{x} < -2\tilde{c}_0 t + \frac{1}{2}\tilde{m}t^2\,, \\ \frac{1}{9g\cos\theta}\left(\frac{\tilde{x}}{t} + 2\tilde{c}_0 - \frac{1}{2}\tilde{m}t\right)^2 & \text{if } -2\tilde{c}_0 t + \frac{1}{2}\tilde{m}t^2 \le \tilde{x} < \tilde{c}_0 t + \frac{1}{2}\tilde{m}t^2\,, \\ \tilde{h}_0 & \text{if } \tilde{x} \ge \tilde{c}_0 t + \frac{1}{2}\tilde{m}t^2\,, \end{cases} \tag{4.37}$$

and

$$\tilde{u}(\tilde{x},t) = \begin{cases} \tilde{m}t & \text{if } \tilde{x} < -2\tilde{c}_0 t + \frac{1}{2}\tilde{m}t^2\,, \\ \frac{2}{3}\left(\frac{\tilde{x}}{t} - \tilde{c}_0 + \tilde{m}t\right) & \text{if } -2\tilde{c}_0 t + \frac{1}{2}\tilde{m}t^2 \le \tilde{x} < \tilde{c}_0 t + \frac{1}{2}\tilde{m}t^2\,, \\ \tilde{m}t & \text{if } \tilde{x} \ge \tilde{c}_0 t + \frac{1}{2}\tilde{m}t^2\,, \end{cases} \tag{4.38}$$

that is, we recover the analytical solution derived by Mangeney et al. [41] to the debris avalanche problem involving a dry bed in the topography-linked coordinate system. However, we argue that the analytical solution (4.32) and (4.33) and that of Mangeney et al. [41] are not valid physically (Note that Remarks 3.1–3.4 are also true for our discussion in this chapter). This is because for cases with steep bed slopes, some material at the top around the wall given in Figure 4.2 would fall down and collapse with some material from around point O moving to the left soon after the wall is removed [46]. This collapse due to the overhang initial condition should have a defect to the solution of Mangeney et al. [41]. Because of this reason, it is better for us to use the solution to the debris avalanche problem in the standard Cartesian coordinate system to test the debris avalanche numerical models.

4.4 Numerical tests

In this section, we test the finite volume numerical models (finite volume methods) used to solve the debris avalanche problem. We compare the performance of Method A (the finite volume method with reconstruction based on stage $w := h + z$, height h, and velocity u) to that of Method B (the finite volume method with reconstruction based on stage w, height h, and momentum $p := hu$) in solving the debris avalanche problem involving a shock. Note that Method A and Method B used in this section are the same as Method A and Method B used in Chapter 3 (see Section 3.5), but different from Method A and Method B in Chapter 2.

In all simulations, the numerical settings are as follows. We implement the same numerical scheme used in Chapter 3. We use second order spatial, and second order temporal discretisations. The central upwind flux formulation proposed by Kurganov et al. [36] is used to compute the numerical fluxes. Quantities are measured in SI units. The acceleration due to gravity is taken as $g = 9.81$. The minmod limiter is applied in the quantity reconstruction. The Courant–Friedrichs–Lewy number used in the simulations is 1.0. The spatial domain is $[-100, 100]$. The initial fluid heights are $h_1 = 5$ on the left and $h_0 = 10$ on the right of the wall. The discrete L^1 absolute error is used to quantify numerical error (see equation (2.12)).

The simulations are done in the Python 2.4 programming language and we adapt the ANUGA package[‡]. Similar numerical solvers have also been tested for solving the Saint-Venant model in our previous work ([45, 47, 50] for the case without friction and [46] for the case with friction).

Three test cases are considered. First, we test the numerical methods for a problem with friction slope $\tan\delta = 0$ and bed slope $\tan\theta = 0$. Table 4.1 shows the errors for stage w, momentum p and velocity u for various numbers of cells for this first case. Second, we consider a problem with friction slope $\tan\delta = 0$ and bed slope $\tan\theta = 0.1$. Table 4.2 presents the errors for stage w, momentum p and velocity u for various numbers of cells for this second case. Finally, for the third case we consider a problem with friction slope $\tan\delta = 0.05$ and bed slope $\tan\theta = 0.1$. The errors for stage w, momentum p and velocity u for various numbers of cells are presented in Table 4.3. For this third case, Figure 4.4 shows the debris avalanche consisting of stage w, momentum p, and velocity u at time $t = 5$ using Method B with 400 cells. Method A results in a similar figure.

Several remarks can be drawn from the numerical results. From the error comparison shown in Tables 4.1, 4.2, and 4.3, we see that Methods A and B performs[§] similarly. To be specific we could say that Method B results in slightly smaller error, but the difference between the results of Methods A and B are indeed insignificant. (The source of discrepancy of the errors produced by Methods A and B is not clear. However, it seems that the discrepancy comes from numerical round-off errors due to different numerical treatments of these meth-

[‡]http://anuga.anu.edu.au/

[§]In the simulations for the debris avalanche problem involving a dry area presented in Chapter 3, Method B resulted in slightly smaller error.

Table 4.1: Errors for $\tan\delta = 0$ and $\tan\theta = 0$ at $t = 5$.

Number	w error		p error		u error	
of cells	A	B	A	B	A	B
100	0.0525	0.0522	0.4592	0.4566	0.0602	0.0599
200	0.0280	0.0280	0.2531	0.2530	0.0318	0.0318
400	0.0146	0.0147	0.1337	0.1343	0.0167	0.0168
800	0.0067	0.0067	0.0599	0.0600	0.0077	0.0077
1600	0.0033	0.0033	0.0296	0.0297	0.0038	0.0038

Table 4.2: Errors for $\tan\delta = 0$ and $\tan\theta = 0.1$ at $t = 5$.

Number	w error		p error		u error	
of cells	A	B	A	B	A	B
100	0.0662	0.0659	0.6348	0.6280	0.0732	0.0725
200	0.0324	0.0322	0.2987	0.2944	0.0364	0.0360
400	0.0165	0.0164	0.1518	0.1504	0.0186	0.0185
800	0.0083	0.0083	0.0764	0.0756	0.0094	0.0094
1600	0.0041	0.0041	0.0382	0.0378	0.0047	0.0047

Table 4.3: Errors for $\tan\delta = 0.05$ and $\tan\theta = 0.1$ at $t = 5$.

Number	w error		p error		u error	
of cells	A	B	A	B	A	B
100	0.0582	0.0576	0.4983	0.4921	0.0658	0.0651
200	0.0301	0.0300	0.2664	0.2642	0.0339	0.0337
400	0.0152	0.0152	0.1360	0.1353	0.0172	0.0172
800	0.0077	0.0077	0.0693	0.0692	0.0087	0.0087
1600	0.0039	0.0039	0.0358	0.0359	0.0045	0.0045

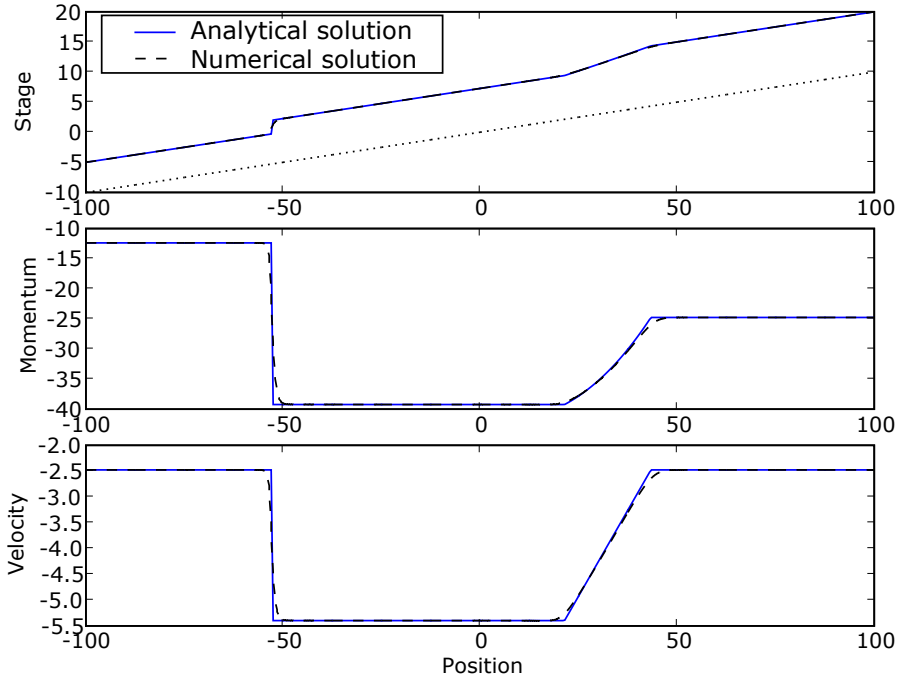

Figure 4.4: Stage, momentum, and velocity for an avalanche with $\tan\delta = 0.05$, $\tan\theta = 0.1$, at $t = 5$, using Method B where the spatial domain is descretised into 400 cells. The dotted line in the first subfigure represents the bed topography.

ods.) In addition, according to Tables 4.1, 4.2, and 4.3, as the cell length is halved, the errors produced by the numerical methods are halved. This means that we have only first order of convergence, even though we have used second order methods. This is due to diffusions around the shock and the corners in the numerical solution, as shown in Figure 4.4. It is well-known in the numerical analysis of conservation laws that in the presence of a shock or discontinuity, finite volume methods converge at most with first order accuracy [38, 39].

4.5 Concluding remarks

We have used the shallow water approach to solve debris avalanche problems involving shock waves. New analytical solutions to the debris avalanche problems involving shock waves have been found. The analytical solutions to the problems in the standard Cartesian coordinate system has been used for testing

the performance of two finite volume numerical models using different ways of reconstructing the conserved quantities. Numerical results show that both reconstructions lead to the same accuracy when the numerical models are used to solve the one-dimensional debris avalanche problem involving a shock for the parameter settings considered.

In the next chapter, we shall study the Carrier-Greenspan periodic solution for flows on a sloping beach. The Carrier-Greenspan periodic solution is a popular benchmark to test the performance of numerical methods used to solve the shallow water equations. Therefore, the next chapter will complement the analytical results of this chapter and the previous chapter.

Chapter 5

The Carrier-Greenspan periodic solution*

5.1 Introduction

The Carrier-Greenspan solutions [12] to the shallow water wave equations for flows on a sloping beach has been widely applied to test the performance of numerical methods used to solve the shallow water wave equations (consult [3, 10, 19, 31, 62] for example). This makes the Carrier-Greenspan solutions almost as popular as the dam break solutions.

The Carrier-Greenspan solutions are of two types, periodic and transient. This chapter focuses only on periodic-type waves. We note that the Carrier-Greenspan periodic solution involves a fixed boundary and a moving boundary. To generate the periodic waves, either the Carrier-Greenspan exact solution or its approximation at the fixed boundary is prescribed.

Johns [31] presented a specific form of the Carrier-Greenspan exact solution of periodic-type over a spatial domain, and prescribed an approximate solution at the zero point of the spatial domain, where the fixed boundary is located. The approximate solution can be applied at the fixed boundary to generate an approximation of the Carrier-Greenspan exact solution using a numerical method as done by a number of authors, such as Johns [31] and Sidén and Lynch [62]. Thus, the numerical solution is affected by two sources of error, namely the error in the boundary condition (at the fixed boundary) and the error introduced by the numerical discretisation. Ideally, when testing a numerical method, we want to

*The results of this chapter have been published [50].

quantify the error introduced by the numerical discretisation. However, testing a numerical method by prescribing the approximate solution at the fixed boundary may be misleading because the error in the boundary condition could be the dominant term. Note that the prescription at the fixed boundary propagates towards the moving boundary (shoreline), so the error at the fixed boundary also propagates towards the shoreline.

Our main point is that, in general, the approximate solution of Johns [31] is unable to accurately estimate the Carrier-Greenspan exact solution at the zero point of the spatial domain. In addition, the large prescription error at the fixed boundary results in a large error of the solution generated by the numerical method. Therefore, we propose new approximations (which are more accurate than the approximate solution of Johns [31]) of the Carrier-Greenspan exact solution at the zero point of the spatial domain.

In this chapter we rederive the formulation of Johns [31] for the Carrier-Greenspan periodic solution, as Johns [31] did not explicitly present the derivation. Based on that formulation, we then derive a new formula for the shoreline velocity and new approximate solutions at the zero point of the spatial domain. The new formula for the shoreline velocity is found using l'Hospital's Rule, and the new approximate solutions at the zero point of the spatial domain are found by extending the approximate solution of Johns [31] using either a formal expansion or fixed point iteration.

To clarify our claim that the use of the Johns prescription can lead to large errors, we compare numerical solutions obtained using a finite volume method to simulate the periodic waves generated by the Johns prescription to those found using the same method to simulate the periodic waves generated by the Carrier-Greenspan exact prescription and to those found using the same method to simulate the periodic waves generated by the new approximations. We shall confirm that the Johns prescription may lead to a large error. In contrast, the new approximations presented in this chapter produce a significantly smaller error.

The remainder of this chapter is organised as follows. Section 5.2 recalls the shallow water wave equations in dimensional and dimensionless systems. Section 5.3 is devoted to the analytical work on the Carrier-Greenspan solution for periodic waves. In Section 5.4, two test cases are investigated, which verify our claim that the use of the Johns prescription can lead to large errors, and in addition, our new approximations are indeed more accurate. In Section 5.5, we

present the rate of convergence of the numerical method used in the simulations. Finally, some concluding remarks are stated in Section 5.6.

5.2 Governing equations

The shallow water wave equations can be written in the standard dimensional system as well as the non-standard dimensionless system. In this section, we recall the shallow water wave equations in both systems. Equations in the dimensionless system are used for simplicity in the analytical work in Section 5.3, while equations in the dimensional system are utilised to easily understand the solution, physically, in the numerical experiments in Section 5.4 and Section 5.5. Note that for our reference in the rest of this chapter, dimensional quantities are denoted by starred variables, while dimensionless quantities are denoted by unstarred variables for brevity of our analytical work. That is, this notational convention is used so that the exposition of our analytical work is clear in terms of technical writing. This notational convention is used only in this chapter.

In the standard Cartesian coordinate system, the conservative shallow water wave equations consist of the mass and momentum equations

$$h^*_{t^*} + (h^*u^*)_{x^*} = 0\,, \tag{5.1}$$

$$(h^*u^*)_{t^*} + \left(h^*u^{*2} + \frac{1}{2}gh^{*2}\right)_{x^*} = -gh^*z^*_{x^*}\,. \tag{5.2}$$

Here, x^* represents the coordinate in one-dimensional space, t^* represents the time variable, $u^* = u^*(x^*, t^*)$ denotes the water velocity, $z^* = z^*(x^*)$ denotes the water bed topography, $h^* = h^*(x^*, t^*)$ denotes the water height, that is, the distance from the free surface to the water bed topography, and g is the acceleration due to gravity.

Consider the situation illustrated in Figure 5.1. The topography changes linearly with x^*

$$z^* = (h^*_0/L^*)x^* - h^*_0\,, \tag{5.3}$$

in which h^*_0 is the vertical distance from the origin O to the topography at any time, and L^* is the horizontal distance from the origin O to the topography when the water is still. This implies that when the water is still: $z^* = -h^*$ over the spatial domain, $z^* = -h^*_0$ at $x^* = 0$, and the position of the shoreline is $x^* = L^*$.

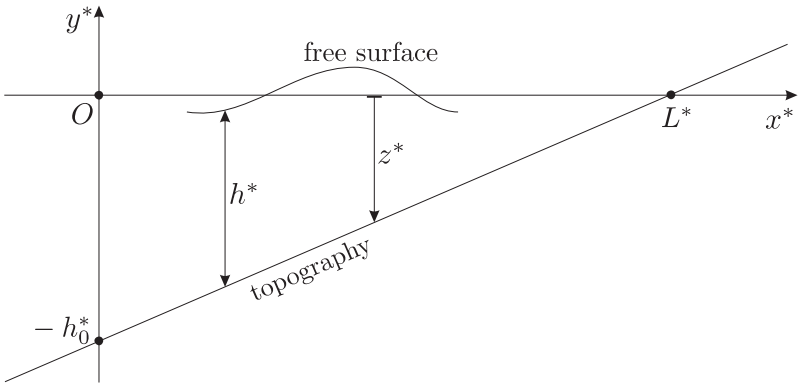

Figure 5.1: Cross section of a sloping beach.

We introduce a new variable called the stage $w^* := h^* + z^*$, which specifies the free surface. Scaling the horizontal distance by L^*, the vertical distance by h_0^*, the time by $L^*/\sqrt{gh_0^*}$, and the velocity by $\sqrt{gh_0^*}$, we can rewrite (5.1) and (5.2) as the nonconservative dimensionless shallow water wave equations

$$w_t + \left[(w + 1 - x)\, u\right]_x = 0\,, \tag{5.4}$$

$$u_t + uu_x + w_x = 0\,. \tag{5.5}$$

Unstarred variables denote dimensionless quantities, and starred variables denote dimensional quantities. Equations (5.4) and (5.5) were used by Johns [31] in developing a finite difference numerical technique to simulate shallow water flows on a sloping beach.

Remark 5.1. For smooth solutions, equations (5.4) and (5.5) are equivalent to the conservative dimensionless shallow water wave equations

$$h_t + (hu)_x = 0\,, \tag{5.6}$$

$$(hu)_t + \left(hu^2 + \frac{1}{2}h^2\right)_x = -hz_x\,. \tag{5.7}$$

5.3 Periodic waves on a sloping beach

In this section, we review the solutions for periodic waves on a sloping beach presented by Carrier and Greenspan [12]. Five subsections are given. In Subsection 5.3.1, we recall the hodograph transformation applied by Carrier and Greenspan [12] to solve the shallow water equations analytically. This solution

in the hodograph variables is then transformed back to the physical variables in Subsection 5.3.2 to obtain the formulation of Johns [31] for the Carrier-Greenspan periodic solution. We then present a new formula for the shoreline velocity in Subsection 5.3.3. In Subsection 5.3.4, we review the Johns approximation, which can be used as boundary conditions for numerical simulations, to the Carrier-Greenspan periodic solution at $x = 0$. Finally, Subsection 5.3.5 is devoted to new (more accurate) approximations of the Carrier-Greenspan periodic solution at $x = 0$.

5.3.1 Carrier-Greenspan solution

Carrier and Greenspan [12] applied the classical hodograph transformation to solve the shallow water wave equations. Two dimensionless hodograph variables

$$\sigma = 4c\,, \tag{5.8}$$

$$\lambda = 2(u + t)\,, \tag{5.9}$$

were used. Here,

$$c = \sqrt{w + 1 - x} \tag{5.10}$$

is the wave speed relative to the water velocity u. In the hodograph system, the variables σ and λ are respectively a space-like and a time-like coordinate [10]. Note that the value of $w+1-x$ is actually the water height h in our dimensionless system. The dimensionless variables are related to the hodograph variables as

$$x = \frac{1}{4}\phi_\lambda - \frac{1}{16}\sigma^2 - \frac{1}{2}u^2 + 1\,, \quad t = \frac{1}{2}\lambda - u\,, \tag{5.11}$$

$$w = \frac{1}{4}\phi_\lambda - \frac{1}{2}u^2\,, \quad u = \sigma^{-1}\phi_\sigma\,, \tag{5.12}$$

where $\phi = \phi(\sigma, \lambda)$ is a potential function satisfying

$$(\sigma\phi_\sigma)_\sigma - \sigma\phi_{\lambda\lambda} = 0\,. \tag{5.13}$$

Equations for stage w and velocity u given by (5.12) are the Carrier-Greenspan exact solution. The choice of $\phi(\sigma, \lambda)$ satisfying (5.13) depends on the conditions of the investigated problem.

Carrier and Greenspan [12] showed that a periodic oscillation of water is formed if we take

$$\phi(\sigma, \lambda) = AJ_0(\omega\sigma)\cos(\omega\lambda) \tag{5.14}$$

as long as the Jacobian $\partial(x,t)/\partial(\sigma,\lambda)$ does not vanish for $\sigma > 0$. This means that the implicit functions $w(x,t)$ and $u(x,t)$ are single-valued, that is, the waves represented by those functions do not break. Here, J_0 is the Bessel function of the first kind of order 0. The constant ω is given by π/T instead of the usual value $2\pi/T$ since a coefficient of two has appeared in the definition of λ in (5.9), where T is the dimensionless period of oscillation. According to (5.13) and (5.14), we can infer that

$$\phi(\sigma,\lambda) = AJ_0(\omega\sigma)\sin(\omega\lambda) \tag{5.15}$$

is also a potential function satisfying (5.13).

5.3.2 The formulation of Johns

In this subsection, we transform the solution (5.12) from the hodograph variables σ, λ to the usual variables x, t.

Considering the potential function (5.15), Johns [31] presented the corresponding Carrier-Greenspan periodic solution and prescribed an approximation of the Carrier-Greenspan periodic solution at $x = 0$. Note that the approximation of the Carrier-Greenspan periodic solution at $x = 0$ was needed by Johns [31] in developing a finite difference numerical technique to simulate shallow water flows on a sloping beach. Here, we derive the formulation of Johns [31] for the Carrier-Greenspan periodic solution, so that in the next subsections we can propose a new formula for the shoreline velocity, review the prescription of Johns at $x = 0$, and propose new approximations of the Carrier-Greenspan periodic solution at $x = 0$. The motivation here is to provide the missing derivation of the solution presented by Johns [31].

Let us consider the potential function (5.15). Its partial derivatives are

$$\phi_\sigma = -\omega A J_1(\omega\sigma)\sin(\omega\lambda), \tag{5.16}$$

$$\phi_\lambda = \omega A J_0(\omega\sigma)\cos(\omega\lambda), \tag{5.17}$$

where J_1 and J_0 are Bessel functions of the first kind of order 1 and 0 respectively. Substituting (5.16) and (5.17) into (5.12), we obtain

$$w = -\frac{1}{2}u^2 + \frac{1}{4}\omega A J_0(\omega\sigma)\cos(\omega\lambda), \tag{5.18}$$

$$u = -\frac{\omega A J_1(\omega\sigma)}{\sigma}\sin(\omega\lambda). \tag{5.19}$$

Letting $\mathcal{A} = \frac{1}{4}\omega A$ and recalling $\omega = \pi/T$, we can write equations (5.18) and (5.19) as

$$w = -\frac{1}{2}u^2 + \mathcal{A}J_0\left(\frac{4\pi\alpha}{T}\right)\cos\left(\frac{2\pi\beta}{T}\right), \tag{5.20}$$

$$u = -\frac{\mathcal{A}J_1\left(\frac{4\pi\alpha}{T}\right)}{\alpha}\sin\left(\frac{2\pi\beta}{T}\right), \tag{5.21}$$

where $\alpha = c$ and $\beta = \frac{1}{2}\lambda$. Here, α and β have the same meaning as that used by Johns [31], but is different from that used by Carrier and Greenspan [12]. Equations (5.20) and (5.21) are the Carrier-Greenspan exact solution corresponding to the potential function (5.15).

For convenience, we rewrite the Carrier-Greenspan exact solution (5.20) and (5.21) as

$$w = -\frac{1}{2}u^2 + \mathcal{A}J_0\left(\frac{4\pi\sqrt{w+1-x}}{T}\right)\cos\left(\frac{2\pi\,(u+t)}{T}\right), \tag{5.22}$$

$$u = -\frac{\mathcal{A}J_1\left(\frac{4\pi\sqrt{w+1-x}}{T}\right)}{\sqrt{w+1-x}}\sin\left(\frac{2\pi\,(u+t)}{T}\right). \tag{5.23}$$

5.3.3 Calculating the stage and velocity

Let us recall some properties of the shoreline before presenting how to calculate the stage w and velocity u over the whole domain. The shoreline is a moving boundary and its position is defined at any time by $c = 0$, so that, introducing the dimensionless horizontal displacement ξ of the shoreline, by (5.10) we have

$$\xi(t) = w(1 + \xi(t), t). \tag{5.24}$$

Differentiating (5.24) with respect to t, we have

$$\frac{d\xi}{dt} = w_x\frac{d\xi}{dt} + w_t. \tag{5.25}$$

Using equation (5.4) and assuming that $w_x(1 + \xi(t), t) < 1$, we obtain the kinematical condition of the shoreline

$$u = \frac{d\xi}{dt} \quad \text{at} \quad x = 1 + \xi. \tag{5.26}$$

A statement of zero depth $c = 0$ at $x = 1 + \xi$ and the kinematical condition (5.26) are the boundary conditions at the shoreline [31]. Note that since the

slope of the topography in the dimensionless system is unity, we have $\xi = w$ at the shoreline, as described by Dietrich, Kolar, and Luettich [19]. This means that the horizontal displacement of the shoreline is equal to the vertical displacement of the shoreline. Since the instantaneous shoreline is fixed by the statement of zero depth $c = 0$ at $x = 1 + \xi$, the horizontal displacement of the shoreline is

$$\xi = -\frac{1}{2}u^2 + \mathcal{A}\cos\left(\frac{2\pi(u+t)}{T}\right), \tag{5.27}$$

according to (5.22).

To test a numerical method, Dietrich et al. [19] used the Carrier-Greenspan solution by referring to the formulation of Johns [31]. Dietrich et al. [19] determined the solution in two steps. First, the system of equations consisting of the horizontal displacement ξ and the velocity u of the shoreline

$$\xi = -\frac{1}{2}u^2 + \mathcal{A}\cos\left(\frac{2\pi}{T}(u+t)\right), \tag{5.28}$$

$$u = \frac{d\xi}{dt} = -u\frac{du}{dt} - \frac{2\mathcal{A}\pi}{T}\left(1 + \frac{du}{dt}\right)\sin\left(\frac{2\pi}{T}(u+t)\right) \tag{5.29}$$

were solved. Equation (5.29) was solved for velocity u using a finite difference approximation of the du/dt terms as well as using the information that the velocity of the shoreline at maximum inundation is zero. The shoreline displacement was found by substituting the shoreline velocity u into (5.28). Second, the stage w and velocity u at the interior points in the wet region (on the left side of the shoreline) were calculated using (5.22) and (5.23).

Here, we propose a different approach for the first step to find the shoreline velocity. Let us consider the velocity formulation (5.21) at the wet areas, that is, on the interval $\alpha \geq 0$. We use the limit of the velocity formulation (5.21) as α goes to zero and take l'Hospital's Rule to obtain

$$u = -\frac{2\pi}{T}\mathcal{A}\sin\left(\frac{2\pi}{T}(u+t)\right), \tag{5.30}$$

which is our new formula for the shoreline velocity. Note that we take (5.21), instead of (5.23), into consideration in the derivation of (5.30) since it is simpler to work with in this case. Then the shoreline displacement is found by substituting the shoreline velocity u into (5.28). The second step is similar to the work of Dietrich et al. [19]. To be specific, we use the Newton-Raphson method to solve (5.22) and (5.23) to obtain the stage w and velocity u of interior points in the

wet region, with a note that the solution at a point closer to the shoreline is the initial approximation for the Newton-Raphson method in obtaining the solution for a point further away from the shoreline.

5.3.4 The Johns approximate solution

In this subsection, we focus on the solution at spatial point $x = 0$, and review the prescription of Johns [31] defined at that point.

Let us assume that $w, u \ll 1$ at $x = 0$. At $x = 0$, Johns [31] prescribed the stage

$$w = \epsilon \cos\left(\frac{2\pi t}{T}\right), \tag{5.31}$$

where ϵ is the dimensionless wave amplitude, and fixed the amplitude factor $\mathcal{A}$ in terms of ϵ, which can be explained as follows. Let

$$w = w_0 + \delta w \quad , \quad u = u_0 + \delta u \tag{5.32}$$

be defined, where $w = w_0$, $u = u_0$ is a reference state, while δw and δu are perturbation terms. Substituting (5.32) into the right hand side of (5.22) and (5.23) with a sea at rest $w_0 = 0$, $u_0 = 0$ as the reference state leads to

$$w = -\frac{1}{2}(\delta u)^2 + \mathcal{A} J_0\left(\frac{4\pi\sqrt{\delta w + 1}}{T}\right) \cos\left(\frac{2\pi(\delta u + t)}{T}\right), \tag{5.33}$$

$$u = -\frac{\mathcal{A} J_1\left(\frac{4\pi\sqrt{\delta w+1}}{T}\right)}{\sqrt{\delta w + 1}} \sin\left(\frac{2\pi(\delta u + t)}{T}\right) \tag{5.34}$$

at $x = 0$. Johns [31] took the closed-form approximations

$$w = \mathcal{A} J_0\left(\frac{4\pi}{T}\right) \cos\left(\frac{2\pi t}{T}\right), \tag{5.35}$$

$$u = -\mathcal{A} J_1\left(\frac{4\pi}{T}\right) \sin\left(\frac{2\pi t}{T}\right), \tag{5.36}$$

which are explicit functions of time t and linear with respect to the amplitude $\mathcal{A}$. This means that all contributions of perturbation terms δw and δu on the right hand side of (5.33) and (5.34) are neglected.

Matching (5.35) with (5.31), Johns [31] fixed

$$\mathcal{A} = \frac{\epsilon}{J_0\left(\frac{4\pi}{T}\right)}, \tag{5.37}$$

which is the amplitude factor $\mathcal{A}$ in terms of ϵ. We note that the assumption made on w and u in the linearisation of Johns ($w, u \ll 1$ at $x = 0$) implies $\mathcal{A} \ll 1$. However, the amplitude factor $\mathcal{A}$ given by (5.37), which implies the quality of the approximations (5.35) and (5.36), is determined by two elements. The first is, rather intuitively, the magnitude of ϵ, while the second is the denominator $J_0(4\pi/T)$. As a result, we can have significant nonlinear effects even for moderate values of ϵ, which will be demonstrated in Section 5.4.

For our reference, equation (5.35) is called "the Johns approximate solution" of the Carrier-Greenspan exact solution for the stage w at $x = 0$, or "the Johns prescription" when it is applied at a fixed boundary to generate a periodic wave using a numerical method. Note that the value of the amplitude factor $\mathcal{A}$ corresponds to the maximum shoreline displacement (see the explanation of Carrier and Greenspan [12] for more details). That is, the shoreline horizontal position varies from $1 - |\mathcal{A}|$ to $1 + |\mathcal{A}|$.

5.3.5 More accurate approximations

In this subsection, we extend the Johns approximate solution, which is defined at $x = 0$, to get more accurate approximations. We describe two ways to implement this extension. The first is by formal expansion of stage w and velocity u with respect to the amplitude $\mathcal{A}$, and the second is by a fixed point iteration with a sea at rest ($w_0 = 0$, $u_0 = 0$) as the initial approximation of the solution. (Note that (5.22) and (5.23) are single valued, as the waves do not break. If the fixed point iteration converges, then it converges to the unique solution to the problem. Note also that one may also use other standard methods, such as the Newton-Raphson method, for solving a system of equations to implement an extension of the Johns approximate solution.)

The extension by formal expansion follows. Suppose that we are interested in obtaining an approximation that is quadratic with respect to the amplitude $\mathcal{A}$. The motivation is that we want to add an extra term to the approximate prescription (5.35) of Johns [31], so that it results in a new approximation that is a second order of accuracy. Let

$$w = w(\mathcal{A}) = W_0 + W_1\mathcal{A} + W_2\mathcal{A}^2 + O\left(\mathcal{A}^3\right) , \tag{5.38}$$

$$u = u(\mathcal{A}) = U_0 + U_1\mathcal{A} + U_2\mathcal{A}^2 + O\left(\mathcal{A}^3\right) \tag{5.39}$$

be defined for some functions $W_0, W_1, W_2, \ldots$ and $U_0, U_1, U_2, \ldots$. Substituting (5.38) and (5.39) into (5.22) and (5.23), and neglecting the $O(\mathcal{A}^3)$ terms that are the cubic and higher order terms, we find the quadratic approximations of the stage w and the velocity u in the following explicit forms:

$$\begin{aligned} w &= \mathcal{A}J_0\left(\frac{4\pi}{T}\right)\cos\left(\frac{2\pi t}{T}\right) \\ &\quad -\mathcal{A}^2\left[\frac{2\pi}{T}J_0\left(\frac{4\pi}{T}\right)J_1\left(\frac{4\pi}{T}\right)\cos\left(\frac{4\pi t}{T}\right)+\frac{1}{2}J_1^2\left(\frac{4\pi}{T}\right)\sin^2\left(\frac{2\pi t}{T}\right)\right], \end{aligned} \tag{5.40}$$

$$\begin{aligned} u &= -\mathcal{A}J_1\left(\frac{4\pi}{T}\right)\sin\left(\frac{2\pi t}{T}\right) \\ &\quad +\mathcal{A}^2\left[\frac{\pi}{T}J_1^2\left(\frac{4\pi}{T}\right)-\frac{\pi}{T}J_0^2\left(\frac{4\pi}{T}\right)+\frac{1}{2}J_0\left(\frac{4\pi}{T}\right)J_1\left(\frac{4\pi}{T}\right)\right]\sin\left(\frac{4\pi t}{T}\right). \end{aligned} \tag{5.41}$$

It should be stressed that the linearised w, given by (5.35), of Johns [31] can be derived using the same process but neglecting the $O(\mathcal{A}^2)$ terms that is the quadratic and higher order terms of the expansion (5.38) and (5.39).

The extension of the Johns approximate solution through a fixed point iteration follows. Based on (5.22) and (5.23), we define kth level approximations of w and u at $x = 0$

$$w_k = -\frac{1}{2}u_{k-1}^2 + \mathcal{A}J_0\left(\frac{4\pi\sqrt{w_{k-1}+1}}{T}\right)\cos\left(\frac{2\pi\left(u_{k-1}+t\right)}{T}\right), \tag{5.42}$$

and

$$u_k = -\frac{\mathcal{A}J_1\left(\frac{4\pi\sqrt{w_{k-1}+1}}{T}\right)}{\sqrt{w_{k-1}+1}}\sin\left(\frac{2\pi\left(u_{k-1}+t\right)}{T}\right), \tag{5.43}$$

for $k = 1, 2, \ldots$, where $w_0 = 0$, $u_0 = 0$. These approximations are constructed recursively with a sea at rest ($w_0 = 0$, $u_0 = 0$) as the initial approximation of the solution. As long as the Jacobian $\partial(x,t)/\partial(\sigma,\lambda)$ does not vanish for $\sigma > 0$ (as mentioned in Subsection 5.3.1), we know that (5.22) and (5.23) are single valued. Therefore, if the fixed point iteration converges, then it converges to the unique solution of the problem. Notice here that the first level recursive approximation w_1 of w is the approximate prescription (5.35) of Johns [31]. The second level recursive approximation w_2 of w and the second level recursive approximation u_2

of u are explicitly given by

$$\begin{aligned} w_2 &= -\frac{1}{2}\left[\mathcal{A}J_1\left(\frac{4\pi}{T}\right)\sin\left(\frac{2\pi t}{T}\right)\right]^2 \\ &\quad +\mathcal{A}J_0\left(\frac{4\pi\sqrt{\mathcal{A}J_0\left(\frac{4\pi}{T}\right)\cos\left(\frac{2\pi t}{T}\right)+1}}{T}\right)\cos\left(\frac{2\pi\left[t-\mathcal{A}J_1\left(\frac{4\pi}{T}\right)\sin\left(\frac{2\pi t}{T}\right)\right]}{T}\right), \quad (5.44) \\ u_2 &= -\frac{\mathcal{A}J_1\left(\frac{4\pi\sqrt{\mathcal{A}J_0\left(\frac{4\pi}{T}\right)\cos\left(\frac{2\pi t}{T}\right)+1}}{T}\right)}{\sqrt{\mathcal{A}J_0\left(\frac{4\pi}{T}\right)\cos\left(\frac{2\pi t}{T}\right)+1}}\sin\left(\frac{2\pi\left(t-\mathcal{A}J_1\left(\frac{4\pi}{T}\right)\sin\left(\frac{2\pi t}{T}\right)\right)}{T}\right). \quad (5.45) \end{aligned}$$

As mentioned by Johns [31], the exact solutions for w, u can be computed by use of (5.22), (5.23). However, it is impossible to explicitly write the exact solutions for w, u. Therefore, if an explicit (closed-form) formulation of w is needed, such as for developing a numerical technique [31], we can take an approximation. We can take either the approximate solution (5.35) of Johns [31], our quadratic approximation (5.40), or our second level recursive approximation (5.44). Of course, we can have more accurate explicit approximations than the quadratic approximation (5.40) and the second level recursive approximation (5.44) by extending the approximate solution (5.35) of Johns [31] using either the formal expansion technique or fixed point iteration, but the formulations will be more complicated to write. Indeed, our approximate solutions (5.40) and (5.44) are more accurate than the approximate solution (5.35) of Johns [31].

5.4 Computational experiments

In this section, we present the main results of the computational experiments to achieve one of the goals of this chapter. Based on these numerical experiments, we see that in some cases the Johns approximate solution (5.35) produces a large error. The numerical experiments are done using the Python 2.4 programming language.

Johns [31] and Sidén and Lynch [62] applied the approximate prescription (5.35) to generate Carrier-Greenspan periodic waves. We claim that the Johns prescription (5.35) is not always a good approximation of the Carrier-Greenspan exact solution at $x^* = 0$, and applying that approximate prescription at the fixed boundary to generate periodic waves using a numerical method may lead to a large error. A discrepancy between the Carrier-Greenspan exact solution and

the Johns approximate solution (prescription) at $x^* = 0$ must exist due to the linearisation of (5.22) to obtain (5.37). To verify our claim, which is the goal of this chapter, we investigate the discrepancy in two test cases: the first shows that the Johns prescription (5.35) is successful, and the second shows that the Johns prescription (5.35) fails to accurately approximate the Carrier-Greenspan exact solution at $x^* = 0$. Note that, in this section, quantities are given in their dimensional values and measured in SI units.

Furthermore, for each test case we compare three numerical solutions with respect to the exact solution in order to investigate the propagation of the prescription error. The first numerical solution is produced by a finite volume method using a well-balanced scheme with the approximate prescription (5.35) of Johns [31] at $x^* = 0$. The second numerical solution is produced by the same method using the same scheme but with the exact prescription (5.18) of Carrier and Greenspan at $x^* = 0$. The third numerical solution is produced by the same method using the same scheme but with our proposed approximate prescription (5.44) at $x^* = 0$.

In the finite volume method, we use the numerical discretisation based on the reconstruction of stage w^*, height h^*, and velocity u^*. We use the second order source, second order spatial (except at the prescribed cell where a first order discretisation is taken), and second order temporal discretisations. The minmod limiter is used for quantity reconstruction. We use the central upwind formulation developed by Kurganov, Noelle, and Petrova [36] to compute the numerical fluxes. The acceleration due to gravity is $g = 9.81$. The minimum fluid height allowed in the flux computation is $h^*_{\text{min}} = 10^{-6}$. The uniform cell length is fixed and given by $\Delta x^* = 100$ (except for testing the rate of convergence given in Section 5.5, in which we take various uniform cell lengths). The CFL number applied is 1.0. The discrete L^1 absolute error is used to quantify numerical error (see equation (2.12)).

The prescribed cell is the first cell containing $x^* = 0$ as its centroid. To be consistent with the work of Johns [31] at the first cell, if the linearised stage (5.35) of Johns is prescribed, we prescribe (5.36) for the velocity. If the exact stage (5.18) of Carrier and Greenspan is prescribed, we take the exact velocity (5.19) as the velocity prescription. If the second level recursive approximation (5.44) of the stage is prescribed, (5.45) is used as the prescription for the velocity.

The numerical prescription is done as follows. Suppose that the linearised

Table 5.1: Average absolute discrepancies (errors) E at $x^* = 0$ when the setting of the first test case is taken. Here, the time interval $[0, T^*]$ is discretised into 1000 nodes. Subscripts w^*, and u^* of E denote the average absolute discrepancy for stage w^*, and velocity u^* respectively.

Stage w prescription at $x^* = 0$	E_{w^*}	E_{u^*}
Johns approximation, Eq. (5.35)	$1.35 \cdot 10^{-3}$	$1.20 \cdot 10^{-6}$
Quadratic approximation, Eq. (5.40)	$2.29 \cdot 10^{-5}$	$1.78 \cdot 10^{-8}$
Second level recursive approximation, Eq. (5.44)	$2.28 \cdot 10^{-5}$	$2.39 \cdot 10^{-8}$

stage (5.35) of Johns [31] is prescribed (the prescription for (5.18) and (5.44) are done similarly). Suppose that we are given time t^*. We compute the value $\bar{w}$ of the stage $w^*(t^*)$ and the value $\bar{u}$ of the velocity $u^*(t^*)$ at $x^* = 0$ using the approximate prescriptions (5.35) and (5.36) of Johns [31]. Then we approximate the stage w^* and the velocity u^* for each spatial point x^* in the first cell using these values $\bar{w}$, and $\bar{u}$. This means that for this first cell, we take an approximation of the stage w^* and that of the velocity u^* that are constants with respect to spatial variable x^*. As a first order discretisation of the bed topography is taken, we have constant (with respect to spatial variable x^*) approximations for all quantities (stage w^*, momentum p^*, velocity u, height h^*, and bed topography z^*) as our reconstruction for this first cell.

5.4.1 First test case: the Johns prescription is successful

In this subsection, we present a test case where the Johns prescription (5.35) successfully approximates the Carrier-Greenspan exact solution at $x^* = 0$. We consider a spatial domain given by the interval $[-50, 55050]$ discretised into 551 cells. The dimensional length $L^* = 50,000$, dimensional height $h_0^* = 500$, and dimensional period $T^* = 900$ are taken. Johns [31] took that at $x^* = 0$ the dimensional amplitude was $\epsilon^* = 1.0$, and we also take this value of ϵ^* in this test case. This setting implies that the shoreline position at any time lies in the interval $[49590.88, 50409.12]$. In a half of the period of oscillation, the shoreline travels a distance about 818.24.

When the Johns approximation (5.35), the quadratic approximation (5.40), and the second level recursive approximation (5.44) are prescribed at position $x^* = 0$ for time t^* on the interval $[0, T^*]$, discrepancies between each of those approximations and the Carrier-Greenspan exact solution occur. If we discretise

the time interval $[0, T^*]$ into 1000 nodes, the average absolute discrepancy at $x^* = 0$ for stage w^* and velocity u^* are as given in Table 5.1. Those discrepancies are very small, but obviously the quadratic approximation (5.40) and the second level recursive approximation (5.44) results in much smaller discrepancies. The results for the quadratic approximation (5.40) and the results for the second level recursive approximation (5.44) are about the same order.

Figure 5.2 illustrates the Carrier-Greenspan exact solution, the Johns approximate solution, and the second level recursive approximation for stage w^* and velocity u^* at position $x^* = 0$ for time t^* on the interval $[0, T^*]$. The discrepancies, in this case, are seen as negligible. We do not graphically show the results for the quadratic approximation since they are similar to the results for the second level recursive approximation.

Now, we investigate whether the negligible discrepancy between the Carrier-Greenspan exact solution and the Johns approximate solution at $x^* = 0$ leads to a negligible discrepancy of any flow quantity when those solutions at $x^* = 0$ are prescribed in numerical simulations to generate periodic waves. We compare here the performance of the Johns approximate solution (5.35), and that of the second level recursive approximation (5.44). Starting from a quiescent state, the numerical method generates a periodic solution after four periods of oscillation. The error comparison is presented in Table 5.2. In general, the method with the Carrier-Greenspan exact prescription results in smaller error. This is because the prescription discrepancy at $x^* = 0$ propagates towards the shoreline as the time evolves and consequently the error produced by the numerical method with the approximate prescription is larger than that produced by the numerical method with the exact prescription. However, we see that the discrepancies of the errors produced using the Johns prescription and Carrier-Greenspan exact prescription are small, as are the discrepancies of the errors produced using the second level recursive approximation and Carrier-Greenspan exact prescription. Figure 5.3 shows the stage w^*, momentum p^*, and velocity u^* at time $t^* = 14T^*$. A large error in terms of the velocity occurs around the wet/dry interface: this is called the wet/dry interface, or wetting and drying problem. It should be stressed that this problem is caused by the inaccuracy of the numerical method that we use at the wet/dry interface, and does not relate to whether the prescription applied in the numerical simulation is exact or approximate. This difficulty of resolving the wet/dry interface problem has been studied in Chapter 2.

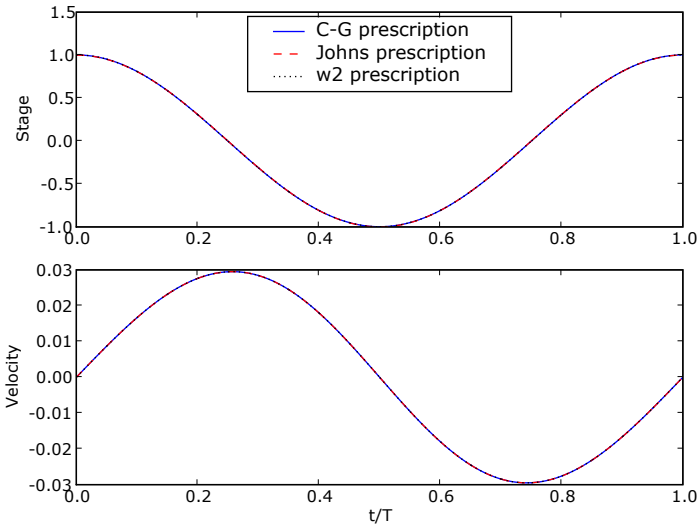

Figure 5.2: Prescriptions for w^* and u^* at $x^* = 0$. Here, $L^* = 50,000$, $h_0^* = 500$, $\epsilon^* = 1.0$, and $T^* = 900$. 'C-G prescription' stands for the Carrier-Greenspan exact prescription (5.18); 'Johns prescription' means the Johns prescription (5.35); '$w2$ prescription' means the prescription of w_2 that is the second level recursive approximation (5.44).

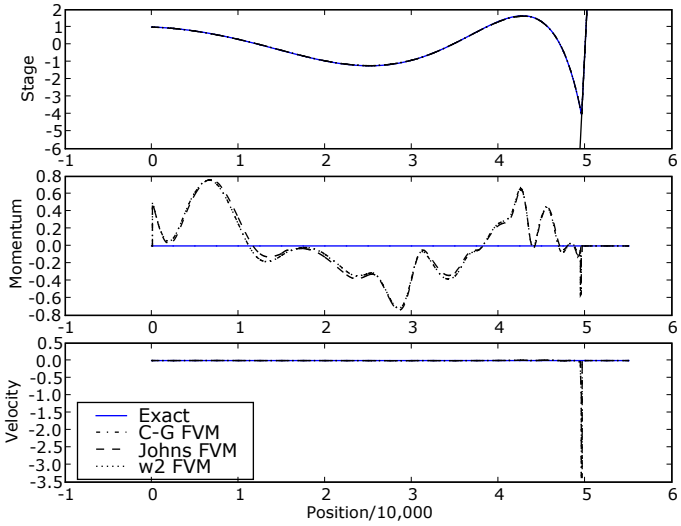

Figure 5.3: Solutions for w^*, p^*, and u^* at $t^* = 14T^*$. Here, $L^* = 50,000$, $h_0^* = 500$, $\epsilon^* = 1.0$, and $T^* = 900$. 'Exact' means the Carrier-Greenspan exact solution; 'C-G FVM' is the numerical solution by FVM with the exact prescription (5.18); 'Johns FVM is the numerical solution by FVM with the Johns prescription (5.35); 'w2 FVM' is the numerical solution by FVM with the prescription of w_2 that is the second level recursive approximation (5.44).

Table 5.2: Errors E for various time. Here, $L^* = 50,000$, $h_0^* = 500$, $\epsilon^* = 1.0$, and $T^* = 900$. Subscripts w^*, p^*, and u^* of E denote the error for stage w^*, momentum p^*, and velocity u^* respectively. Superscript J of E denotes that the computation uses the Johns prescription, while superscript CG denotes that the computation uses Carrier-Greenspan exact prescription, and superscript w_2 denotes that the computation uses our w_2 approximate prescription.

Time (T^*)	$E^J_{w^*}$	$E^{CG}_{w^*}$	$E^{w_2}_{w^*}$	$E^J_{p^*}$	$E^{CG}_{p^*}$	$E^{w_2}_{p^*}$	$E^J_{u^*}$	$E^{CG}_{u^*}$	$E^{w_2}_{u^*}$
...	...	...	...	...	...	...	...	...	...
4	0.0130	0.0126	0.0127	0.686	0.679	0.679	0.0117	0.0114	0.0114
$4 + 1/3$	0.0138	0.0138	0.0138	0.693	0.693	0.694	0.0092	0.0090	0.0091
$4 + 2/3$	0.0161	0.0161	0.0161	0.500	0.480	0.481	0.0123	0.0122	0.0122
5	0.0119	0.0114	0.0114	0.643	0.636	0.636	0.0111	0.0109	0.0109
$5 + 1/3$	0.0117	0.0117	0.0117	0.648	0.648	0.649	0.0066	0.0065	0.0065
$5 + 2/3$	0.0119	0.0119	0.0119	0.393	0.376	0.376	0.0106	0.0106	0.0106
6	0.0076	0.0074	0.0074	0.413	0.409	0.409	0.0094	0.0092	0.0092
...	...	...	...	...	...	...	...	...	...
12	0.0072	0.0069	0.0070	0.244	0.246	0.246	0.0090	0.0088	0.0088
$12 + 1/3$	0.0053	0.0051	0.0051	0.360	0.364	0.365	0.0057	0.0056	0.0055
$12 + 2/3$	0.0084	0.0084	0.0084	0.220	0.226	0.226	0.0102	0.0103	0.0103
13	0.0072	0.0069	0.0070	0.245	0.246	0.246	0.0090	0.0088	0.0088
$13 + 1/3$	0.0053	0.0051	0.0051	0.360	0.364	0.365	0.0057	0.0056	0.0055
$13 + 2/3$	0.0084	0.0084	0.0084	0.220	0.225	0.226	0.0102	0.0103	0.0103
14	0.0072	0.0069	0.0070	0.245	0.246	0.246	0.0090	0.0088	0.0088
...	...	...	...	...	...	...	...	...	...

It is worth questioning why the discrepancy of the solutions at $x^* = 0$ in this test case is negligible. This error is due to the small magnitude of the amplitude factor $\mathcal{A}$ in this test case. Recall that the amplitude factor $\mathcal{A}$ is found from the process of linearisation of an equation, discussed in Subsection 5.3.4. The linear approximation matches exactly with the exact solution when $\mathcal{A} = 0$. In addition, a small magnitude of $\mathcal{A}$ leads to a small error of the linear approximation; a larger magnitude of $\mathcal{A}$ results in a larger error of the linear approximation.

Recalling the specified values of the dimensional length $L^* = 50,000$, dimensional height $h_0^* = 500$, and dimensional amplitude $\epsilon^* = 1.0$, we can plot a graph relating the dimensional period T^* and the amplitude factor $\mathcal{A}$ as given in Figure 5.4 using (5.37). The vertical lines in the figure are the asymptotes which are the singularities of $\mathcal{A}$, that is, the zeros of the denominator in (5.37). For $T^* = 900$, the amplitude factor is $\mathcal{A} = -8.18 \cdot 10^{-3}$.

Roughly speaking, using the specified values of the dimensional length L^*,

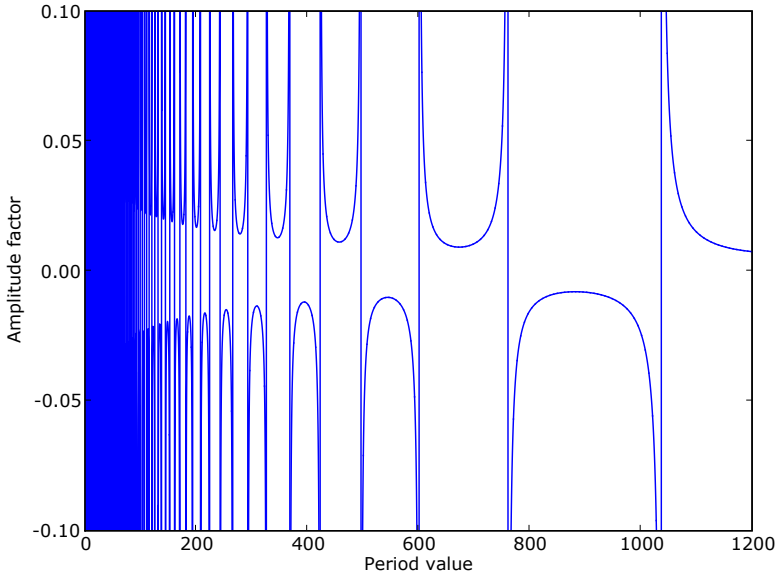

Figure 5.4: Relation of the dimensional period T^* and the amplitude factor $\mathcal{A}$ for $L^* = 50,000$, $h_0 = 500$, and $\epsilon^* = 1.0$. The vertical lines are asymptotes.

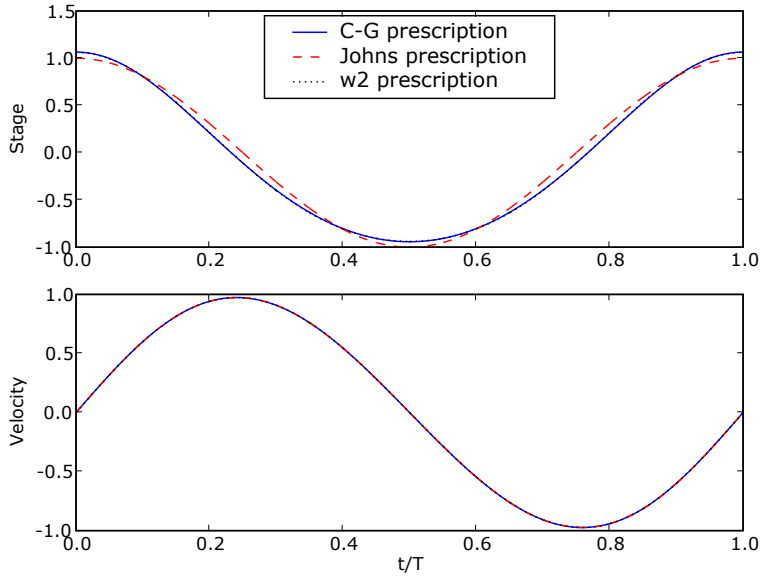

Figure 5.5: Solutions for w^* and u^* at $x^* = 0$. Here, $L^* = 50,000$, $h_0^* = 500$, $\epsilon^* = 1.0$, and $T^* = 1020$. 'C-G prescription' stands for the Carrier-Greenspan exact prescription (5.18); 'Johns prescription' means the Johns prescription (5.35); '$w2$ prescription' means the prescription of w_2 that is the second level recursive approximation (5.44).

dimensional height h_0^*, and dimensional amplitude ϵ^* in this first test case, the Johns approximate solution (found by involving a linearisation of an equation) at $x^* = 0$ is accurate on some intervals of the dimensional period T^*, such as $[800, 1000]$, where all points in this interval are far enough away from asymptotes. This is illustrated in Figure 5.4 in which the tangent lines on the interval $[800, 1000]$, especially for points around $T^* = 900$, are almost horizontal.

Using the same values of the dimensional length L^*, dimensional height h_0^*, and dimensional amplitude ϵ^*, but taking the dimensional period $T^* = 1020$, we find a larger discrepancy between the approximate and the exact solutions at $x^* = 0$, as shown in Figure 5.5. Now, we have $\mathcal{A} = -5.26 \cdot 10^{-2}$. When we discretise the time interval $[0, T^*]$ into 1000 nodes, the average absolute discrepancy at $x^* = 0$ for stage w^* and velocity u^* are $5.65 \cdot 10^{-2}$ and $1.30 \cdot 10^{-4}$ respectively for the Johns approximate solution, and $3.16 \cdot 10^{-3}$ and $6.83 \cdot 10^{-6}$ respectively for our second level approximation. These discrepancies for the Johns approximate solution are still relatively small. Unfortunately, if we take a larger value of T^* closer to the asymptote lying on the interval $[1000, 1200]$ to get a larger value of $\mathcal{A}$, the Jacobian $\partial(x,t)/\partial(\sigma,\lambda)$ may vanish for $\sigma > 0$, that is, a breaking wave occurs. The vanishing of the Jacobian $\partial(x,t)/\partial(\sigma,\lambda)$ can be verified analytically from (5.11), (5.15), (5.16), and (5.17).

5.4.2 Second test case: the Johns prescription fails

In this subsection, we present a test case where the Johns prescription (5.35) fails to accurately approximate the Carrier-Greenspan exact solution at $x^* = 0$. We consider a spatial domain given by the interval $[-50, 65050]$ discretised into 651 cells. The dimensional length $L^* = 50,000$, dimensional height $h_0^* = 500$, and dimensional period $T^* = 3600$ are taken. We fix $\epsilon^* = 5.0$ in this test case. We consider these values in order to obtain a larger value of amplitude factor $\mathcal{A}$ than the value of $\mathcal{A}$ in the first test case and that the Jacobian $\partial(x,t)/\partial(\sigma,\lambda)$ does not vanish for $\sigma > 0$. Hence, the error of the Johns prescription (5.35) in this test case is larger than that in the first test case.

The setting here implies that the shoreline position at any time lies in the interval $[38745.65, 61254.35]$ since $\mathcal{A} = -2.25 \cdot 10^{-1}$, and that no breaking wave occurs. In a half of the period of oscillation, the shoreline travels a distance more than $22.5 \cdot 10^3$. This distance is more than 27 times of the distance traveled by the shoreline in the first test case. Recalling the specified values of the dimen-

Table 5.3: Average absolute discrepancies (errors) E at $x^* = 0$ when the setting of the second test case is taken. Here the time interval $[0, T^*]$ is discretised into 1000 nodes. Subscripts w^*, and u^* of E denote the average absolute discrepancy for stage w^*, and velocity u^* respectively.

Stage w prescription at $x^* = 0$	E_{w^*}	E_{u^*}
Johns approximation, Eq. (5.35)	1.83	$2.69 \cdot 10^{-2}$
Quadratic approximation, Eq. (5.40)	$3.19 \cdot 10^{-1}$	$4.26 \cdot 10^{-3}$
Second level recursive approximation, Eq. (5.44)	$2.88 \cdot 10^{-1}$	$3.85 \cdot 10^{-3}$

sional length L^*, dimensional height h_0^*, and dimensional amplitude ϵ^*, we plot the relation between the dimensional period T^* and the amplitude factor $\mathcal{A}$ in Figure 5.6.

When the Johns approximation (5.35), the quadratic approximation (5.40), and the second level recursive approximation (5.44) are prescribed at position $x^* = 0$ for time t^* on the interval $[0, T^*]$, discrepancies between each of those approximations and the Carrier-Greenspan exact solution occur. Discretising the time interval $[0, T^*]$ into 1000 nodes, we obtain that the average absolute discrepancy at $x^* = 0$ for stage w^* and velocity u^* are as given in Table 5.3. We see that the quadratic approximation (5.40), and the second level recursive approximation (5.44) results in much smaller discrepancies than the discrepancies that result from the Johns approximate solution (5.35). The results for the quadratic approximation (5.40) and the results for the second level recursive approximation (5.44) are again of around the same order.

Figure 5.7 illustrates the Carrier-Greenspan exact solution, the Johns approximate solution, and the second level recursive approximation for stage w^* and velocity u^* at position $x^* = 0$ for time t^* on the interval $[0, T^*]$. The discrepancies that result from the Johns approximate solution are now large, while the discrepancies from the second level recursive approximation are much smaller. We do not graphically show the results for the quadratic approximation since they are similar to the results for the second level recursive approximation.

The method with the linear Johns prescription produces very large errors, as shown in Table 5.4, due to the low order of accuracy of the approximation. Large errors can also be observed graphically for the stage w^*, momentum p^*, and velocity u^* at time $t^* = 14T^*$, as illustrated in Figure 5.8. A magnification of Figure 5.8, depicting the stage w^* at cells around the wet/dry interfaces on the interval $[38400, 39400]$, is shown in Figure 5.9. Notice that in Figure 5.9, the

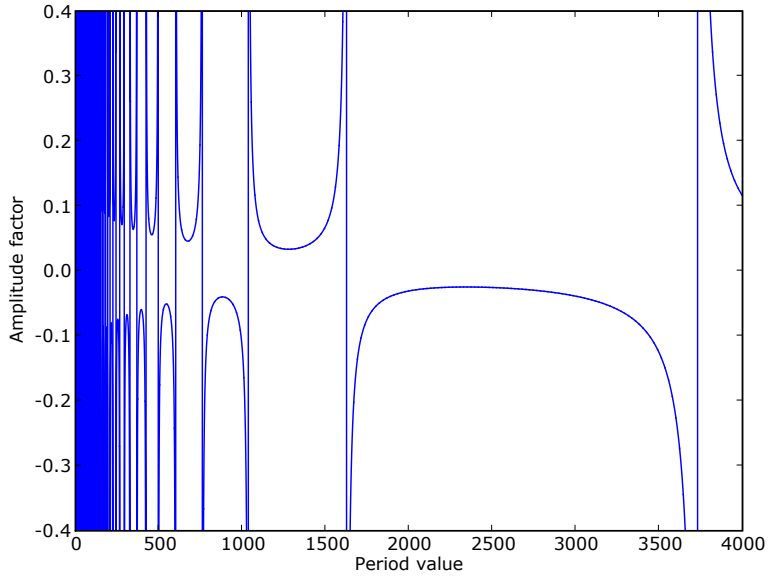

Figure 5.6: Relation of the dimensional period T^* and the amplitude factor $\mathcal{A}$ for $L^* = 50,000$, $h_0 = 500$, and $\epsilon^* = 5.0$. The vertical lines are asymptotes.

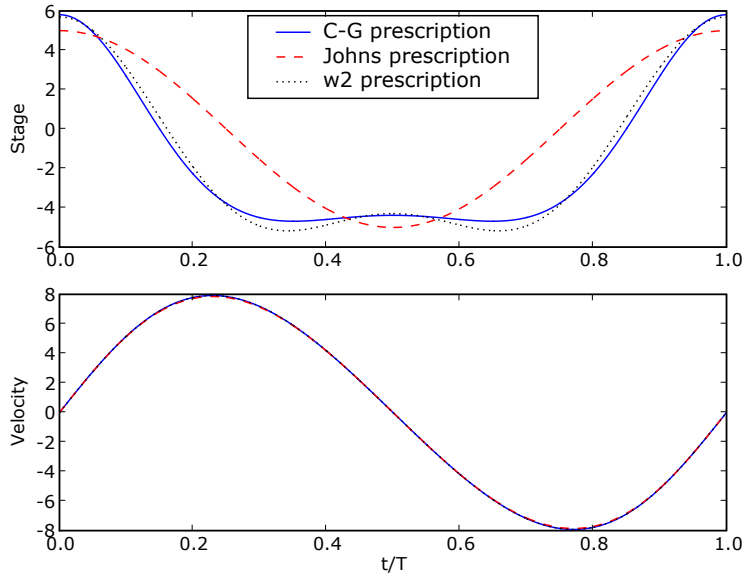

Figure 5.7: Solutions for w^* and u^* at $x^* = 0$. Here, $L^* = 50,000$, $h_0^* = 500$, $\epsilon^* = 5.0$, and $T^* = 3600$. 'C-G prescription' stands for the Carrier-Greenspan exact prescription (5.18); 'Johns prescription' means Johns prescription (5.35); '$w2$ prescription' means the prescription of w_2 that is the second level recursive approximation (5.44).

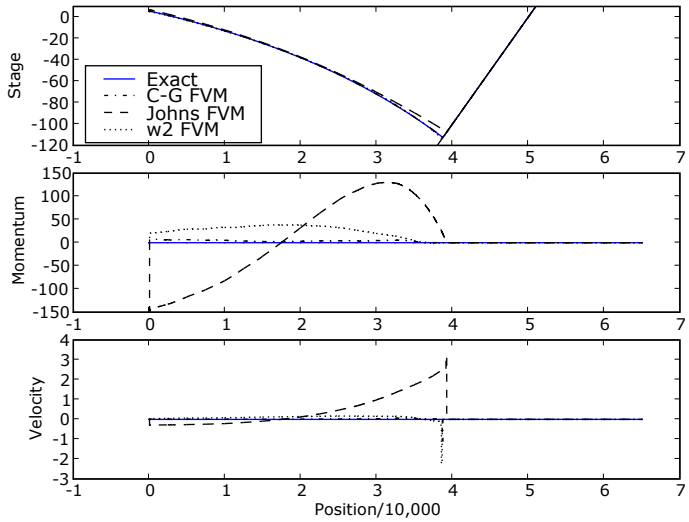

Figure 5.8: Solutions for w^*, p^*, and u^* at $t^* = 14T^*$. Here, $L^* = 50,000$, $h_0^* = 500$, $\epsilon^* = 5.0$, and $T^* = 3600$. 'Exact' means the Carrier-Greenspan exact solution; 'C-G FVM' is the numerical solution by FVM with the exact prescription (5.18); 'Johns FVM is the numerical solution by FVM with the Johns prescription (5.35); 'w2 FVM' is the numerical solution by FVM with the prescription of w_2 that is the second level recursive approximation (5.44).

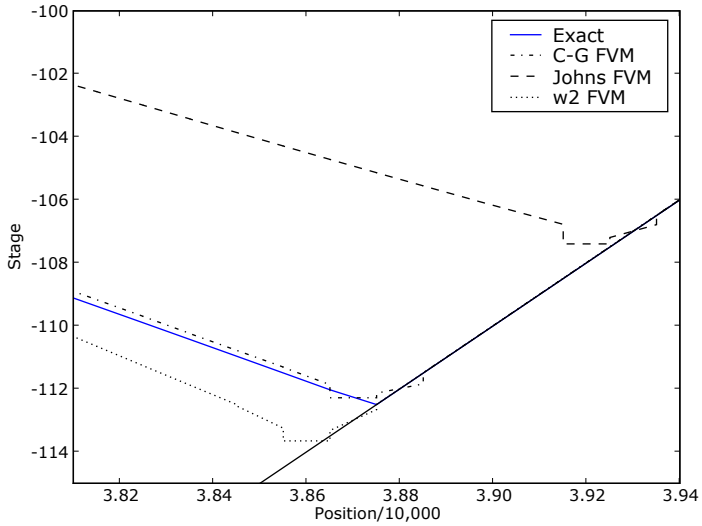

Figure 5.9: A magnification of Figure 5.8 for w^* on the interval $[38400, 39400]$. Here, $t^* = 14T^*$, $L^* = 50,000$, $h_0^* = 500$, $\epsilon^* = 5.0$, and $T^* = 3600$. 'Exact' means the Carrier-Greenspan exact solution; 'C-G FVM' is the numerical solution by FVM with the exact prescription; 'Johns FVM is the numerical solution by FVM with the Johns prescription; 'w2 FVM' is the numerical solution by FVM with the prescription of w_2 that is the second level recursive approximation.

Table 5.4: Errors E for various time. Here, $L^* = 50,000$, $h_0^* = 500$, $\epsilon^* = 5.0$, and $T^* = 3600$. Subscripts w^*, p^*, and u^* of E denote the error for stage w^*, momentum p^*, and velocity u^* respectively. Superscript J of E denotes that the computation uses the Johns prescription, while superscript CG denotes that the computation uses Carrier-Greenspan exact prescription, and superscript w_2 denotes that the computation uses our w_2 approximate prescription.

Time (T^*)	$E^J_{w^*}$	$E^{CG}_{w^*}$	$E^{w_2}_{w^*}$	$E^J_{p^*}$	$E^{CG}_{p^*}$	$E^{w_2}_{p^*}$	$E^J_{u^*}$	$E^{CG}_{u^*}$	$E^{w_2}_{u^*}$
...	...	...	...	...	...	...	...	...	...
13	0.999	0.048	0.238	50.077	2.459	15.752	0.376	0.014	0.069
$13 + 1/6$	1.083	0.065	0.262	46.711	0.902	5.305	0.459	0.009	0.090
$13 + 2/6$	2.187	0.030	0.320	22.999	3.626	8.844	0.266	0.046	0.078
$13 + 3/6$	0.841	0.041	0.240	47.976	3.038	15.831	0.373	0.017	0.071
$13 + 4/6$	0.872	0.066	0.218	42.886	1.075	5.827	0.438	0.066	0.147
$13 + 5/6$	2.124	0.044	0.276	29.172	3.411	8.404	0.288	0.139	0.147
14	1.001	0.048	0.237	50.230	2.433	15.712	0.377	0.014	0.069
...	...	...	...	...	...	...	...	...	...

horizontal and the vertical distances from the wet/dry interface for the Carrier-Greenspan exact solution to the wet/dry interface for the numerical solution generated using the Johns prescription are about 500 and 5 respectively.

In this test case, the linearisation of (5.22) done by Johns [31] results in a poor approximation of the exact solution at $x^* = 0$. This poor approximation then leads to a very large error when it is prescribed in place of the Carrier-Greenspan exact solution at $x^* = 0$ to generate periodic waves in the numerical simulation. According to the simulation results, our second level recursive approximation (5.44) indeed produces smaller errors than the Johns approximate solution (5.35).

Note that in the simulations of periodic waves on a sloping beach, we consider the following remarks.

Remark 5.2. The computer program can be run as long as the waves do not break, that is, the Jacobian $\partial(x,t)/\partial(\sigma,\lambda)$ does not vanish for $\sigma > 0$. Here $\sigma > 0$ represents the wet region.

Remark 5.3. The generated waves propagate from the Origin of the spatial domain (where the Origin is located at a point on the surface of the sea) to the shoreline on the beach.

Table 5.5: Errors E for various uniform cell length (Δx) of spatial discretisation. Here, $L^* = 50,000$, $h_0^* = 500$, $\epsilon^* = 1.0$, and $T^* = 900$. Subscripts w^*, p^*, and u^* of E denote the error for stage w^*, momentum p^*, and velocity u^* respectively. Superscript CG of E denotes that the computation uses Carrier-Greenspan exact prescription. Domain means the interval of spatial domain to be considered and discretised. The errors are computed at $t = 14T^*$.

Cell length	Domain	$E_{w^*}^{CG}$ in 10^{-3}	$E_{p^*}^{CG}$ in 10^{-2}	$E_{u^*}^{CG}$ in 10^{-4}
200	$[-100, 55100]$	23.84	88.19	254.05
100	$[-50, 55050]$	6.95	24.64	88.12
50	$[-25, 55025]$	2.13	13.19	35.25
25	$[-12.5, 55012.5]$	1.36	9.36	8.42
12.5	$[-6.25, 55006.25]$	1.26	7.24	6.23

5.5 Rate of convergence

In this section, we present the rate of convergence of the numerical solution to the analytical solution using the exact boundary condition when the computational mesh is refined.

We expect that the numerical method leads to a first order of convergence since we take a first order discretisation at the prescribed cell. Due to the wet/dry interface problem, the expected rate of convergence is not achieved, as can be observed in Table 5.5. However, if we truncate the spatial domain in such a way that the computation does not involve the wet/dry interface problem, the numerical method indeed results in a first order of convergence, as shown in Table 5.6. This first order of convergence is observed, since the errors produced by the numerical method are halved as the cell length is halved.

The results in Table 5.5 and Table 5.6 are found from the simulations using the setting of the first test case given in Subsection 5.4.1. Recall that the shoreline position at any time lies in the interval $[49590.88, 50409.12]$. Therefore, the truncated domains in Table 5.6 obviously do not include the moving boundary (shoreline). Consequently, all computations presented in Table 5.6 do not involve the wet/dry interface problem. Note that a simulation with truncated domain here means that we prescribe the corresponding Carrier-Greenspan exact solution at cells located at both ends of the truncated domain; in addition, the domain is taken such that the centroid of the first cell is at $x^* = 0$.

Table 5.6: Errors E for various uniform cell length (Δx) of spatial discretisation. Here, $L^* = 50,000$, $h_0^* = 500$, $\epsilon^* = 1.0$, and $T^* = 900$. Subscripts w^*, p^*, and u^* of E denote the error for stage w^*, momentum p^*, and velocity u^* respectively. Superscript CG of E denotes that the computation uses Carrier-Greenspan exact prescription. Domain means the interval of spatial domain to be considered and discretised. The errors are computed at $t = T^*$.

Cell length	Domain	$E_{w^*}^{CG}$ in 10^{-5}	$E_{p^*}^{CG}$ in 10^{-2}	$E_{u^*}^{CG}$ in 10^{-5}
200	$[-100, 10100]$	97.17	48.94	110.98
100	$[-50, 10050]$	46.42	25.13	56.99
50	$[-25, 10025]$	22.68	12.73	28.87
25	$[-12.5, 10012.5]$	11.55	6.39	14.49
12.5	$[-6.25, 10006.25]$	5.80	3.20	7.26

5.6 Concluding remarks

We have reviewed a special type of the Carrier-Greenspan solution, which can be used to test the performance of a numerical method for the shallow water wave equations. A new formula for the shoreline velocity has been derived. The new formula is very simple to use, as it involves no derivatives in calculating the shoreline velocity. We have also proposed some new approximations (a quadratic approximation and a second level recursive approximation) of the Carrier-Greenspan periodic solution, which are more accurate than the Johns approximate solution at the zero point of the spatial domain. In addition, results of a finite volume method with the approximate prescriptions applied at the fixed boundary to generate periodic waves on a sloping beach have been compared to those of the same method with the Carrier-Greenspan exact prescription.

We have found that if the discrepancy between the approximate and the exact prescription is negligible, then the errors of both numerical solutions are similar. If the discrepancy is very large, the error of the numerical solution with the approximate prescription is much larger than that of the numerical solution with the exact prescription. This means that the prescription at the fixed boundary significantly affects the error of the numerical solution. Therefore, we suggest that the exact, instead of the approximate prescription, should be applied when the Carrier-Greenspan periodic waves are used to assess the performance of a numerical method.

However, if an explicit formulation of the stage at the zero point of the spatial domain is needed, such as for developing a numerical technique, an approximation

of it can be taken. We can take either the approximate solution of Johns, the quadratic approximation, the second level recursive approximation, or another approximation as long as it is guaranteed that the error produced at the zero point of the spatial domain is negligible.

This point is the end of Part II, covering the importance of analytical work relating to numerical work, of this thesis. Obviously, the analytical solutions we derived can be used to test the performance of numerical methods for Saint-Venant models. In Part III, we shall discuss the numerical entropy production and weak local residuals as refinement indicators for adaptive finite volume methods.

PART III:
INDICATORS FOR ADAPTIVE METHODS

This page was intentionally left blank.

Chapter 6

Numerical entropy production*

6.1 Introduction

Recall that systems of shallow water equations are hyperbolic, and they admit discontinuous solutions even when the initial condition is smooth. It is well-known that a numerical method to solve these systems usually produces diffusion and dispersion around discontinuities. To get a more accurate numerical solution, we could refine the whole computational grid up to certain level of refinement. However, doing so definitely results in a very expensive computation. Instead, we use an adaptive numerical method. The adaptive numerical method employs a smoothness indicator which produces large values of the indicator around discontinuities. The adaptive numerical method then takes some actions around the discontinuities to produce a more accurate solution. In our adaptive finite volume method, the grids in smooth regions are coarsened to reduce the computational costs and the grids in nonsmooth regions are refined to get more accurate solutions.

Numerical entropy production (NEP) can be used as a smoothness indicator of a numerical solution to balanced laws. It was introduced for conservation laws by Puppo [54]. Its numerical theory for conservation laws has so far been developed by Puppo and Semplice [54, 55, 56, 57], where in their work the NEP was mainly implemented for gas dynamics. Other implementations of NEP for conservation laws and mainly gas dynamics are the work of Golay et al. [22, 25].

In this chapter, we propose the NEP as a smoothness indicator or a shock

*Preliminary results of this chapter have been published [47]. The main results are in preparation for a publication submission.

detector for shallow water flows in one, one-and-a-half, and two dimensions. This new application of the numerical entropy production is adapted from its application to gas dynamics, as presented by Golay [25] and Puppo [54]. The performance of the numerical entropy production as a smoothness indicator is compared with that of weak local residuals proposed by Karni, Kurganov, and Petrova [33] and Constantin and Kurganov [16].

The rest of this chapter is structured as follows. NEP in one, one-and-a-half, and two dimensions are presented in Sections 6.2, 6.3, 6.4 respectively. Then we draw some concluding remarks in Section 6.5. We use the shorthand notation 1D for one dimension, 1.5D for one-and-a-half dimensions, and 2D for two dimensions.

6.2 Numerical entropy production in 1D

In this section, we present a numerical scheme for the evolution of the entropy and a definition of the numerical entropy production for the one-dimensional shallow water equations (2.1). We note that to apply the numerical entropy production as a smoothness indicator or shock detector, we do not have to use a well-balanced scheme. However, in this work we choose a well-balanced scheme because it is more robust than a standard scheme for solving the shallow water wave equations, in that it preserves the steady state of "a lake at rest" [53]. For this reason, we recall the hydrostatic reconstruction (2.3)–(2.5) and the semi-discrete well-balanced scheme (2.6) used to solve the shallow water equations (2.1).

This section is organised as follows. We present an existing numerical entropy scheme and its properties in Subsection 6.2.1. An alternative numerical entropy scheme and its properties are covered in Subsection 6.2.2. Finally, we present one-dimensional numerical results in Subsection 6.2.3.

6.2.1 An existing numerical entropy scheme

In this subsection, an existing numerical entropy scheme is presented. We use the term "existing" to distinguish between the scheme already published [47] and another scheme with the term "alternative" that shall be discussed in Subsection 6.2.2.

An entropy inequality can be derived from the shallow water wave equations (2.1) by simple algebraic operations, as shown by Bouchut [7]. The entropy

inequality is

$$\eta_t + \psi_x \leq 0\,, \tag{6.1}$$

where

$$\eta\left(\mathbf{q}(x,t), z(x)\right) = \frac{1}{2}hu^2 + \frac{1}{2}gh^2 + ghz\,, \tag{6.2}$$

$$\psi\left(\mathbf{q}(x,t), z(x)\right) = \left(\frac{1}{2}hu^2 + gh^2 + ghz\right)u \tag{6.3}$$

are the entropy and the entropy flux respectively for the shallow water wave equations (2.1). For smooth solutions, the entropy inequality (6.1) becomes an equality, called the entropy equation. For solutions with discontinuities, the entropy inequality (6.1) becomes a strict inequality in the weak sense.

The evolution of the entropy η together with the evolution of the conserved quantity $\mathbf{q}$ can be used to detect the location of shock waves accurately. For the evolution of the entropy η, we adopt the semi-discrete scheme (2.6) with the numerical entropy Θ, the numerical entropy fluxes Ψ^r, Ψ^l, and the numerical entropy source 0 in place of the numerical quantity $\mathbf{Q}$, the numerical quantity fluxes $\mathcal{F}^r$, $\mathcal{F}^l$, and the numerical quantity source $\mathbf{S}_i^{(j)}$ respectively. Therefore, given the value of $\Theta_i^{n-1} := \eta\left(\mathbf{Q}_i^{n-1}\right)$, we take a semi-discrete scheme

$$\Delta x_i \frac{d}{dt}\Theta_i + \Psi^r(\mathbf{Q}_i, \mathbf{Q}_{i+1}, z_{i,r}, z_{i+1,l}) - \Psi^l(\mathbf{Q}_{i-1}, \mathbf{Q}_i, z_{i-1,r}, z_{i,l}) = 0 \tag{6.4}$$

to obtain the value of Θ_i^n, where

$$\Psi^r(\mathbf{Q}_i, \mathbf{Q}_{i+1}, z_{i,r}, z_{i+1,l}) := \Psi(\mathbf{Q}^*_{i,r}, \mathbf{Q}^*_{i+1,l}, z^*_{i+1/2}) \tag{6.5}$$

and

$$\Psi^l(\mathbf{Q}_{i-1}, \mathbf{Q}_i, z_{i-1,l}, z_{i,r}) := \Psi(\mathbf{Q}^*_{i-1,r}, \mathbf{Q}^*_{i,l}, z^*_{i-1/2}) \tag{6.6}$$

are the right and left numerical entropy fluxes of the ith cell calculated at $x_{i+1/2}$ and $x_{i-1/2}$ respectively. Here, Θ is the approximation of the entropy η, and Ψ is a consistent numerical entropy flux in the sense that $\Psi(\mathbf{Q}, \mathbf{Q}) = \Psi(\mathbf{Q})$ (see Tadmor [68] for more details on a consistent numerical entropy flux). As in scheme (2.6), we use the auxiliary values $\mathbf{Q}^*$ instead of the true values $\mathbf{Q}$. Note that at the $(i + \frac{1}{2})$th interface, the transferred entropy is accounted for by the heights $h^*_{i,r}$ and $h^*_{i+1,l}$.

The numerical entropy production is then defined by

$$E_i^n = \frac{1}{\Delta t}\left(\eta\left(\mathbf{Q}_i^n\right) - \Theta_i^n\right), \tag{6.7}$$

which is the local truncation error of the entropy. Here, Θ_i^n is obtained from the numerical entropy scheme (6.4) with $\eta\left(\mathbf{Q}^{n-1}\right)$ as the input; $\mathbf{Q}_i^n$ is calculated from the finite volume scheme with $\mathbf{Q}^{n-1}$ as the input; and Δt is the time step used in solving the semi-discrete ordinary differential equations (2.6) and (6.4).

The order of accuracy for the numerical entropy production (6.7) in a rough region (nonsmooth solution) is lower than the order of accuracy in a smooth region [55]. As a result, the values of the numerical entropy production in the region of a shock discontinuity are larger than the values in smooth regions. This property makes the numerical entropy production a good candidate as a smoothness indicator or shock detector.

In the following theorem, we present properties of the numerical entropy scheme described above related to the steadiness of a lake at rest and its consistency to the entropy equation on smooth regions.

Theorem 6.1. *The semi-discrete scheme (6.4) with fluxes (6.5) and (6.6)*

1. *preserves the entropy steady state of a lake at rest, and*
2. *is consistent with the entropy equation, which is expression (6.1) restricted with an equality sign.*

Proof. Assume that we are given a steady state of a lake at rest. Then we have, $w_t = 0$ and $u = 0$ everywhere. Now, we consider an arbitrary ith cell. The hydrostatic reconstruction (2.3)–(2.5) and the discrete version of the flux function (6.2) together with $u_i = 0$ imply that

$$\Psi^r(\mathbf{Q}_i, \mathbf{Q}_{i+1}, z_{i,r}, z_{i+1,l}) = \Psi^l(\mathbf{Q}_{i-1}, \mathbf{Q}_i, z_{i-1,r}, z_{i,l}) = 0\,. \tag{6.8}$$

Equation (6.8) is a consequence of the use of a consistent numerical flux Ψ. Therefore, the entropy is constant with respect to time. This completes the proof for preserving the entropy steady state of a lake at rest.

To prove that the scheme (6.4) is consistent, we need to show that the numerical fluxes are consistent with the exact flux, as specified by Bouchut [6]. The conserved quantities are reconstructed in the first order framework. The consistency with the exact flux

$$\Psi^r(\mathbf{Q}, \mathbf{Q}, z, z) = \Psi^l(\mathbf{Q}, \mathbf{Q}, z, z) = \psi\left(\mathbf{Q}, z\right) \tag{6.9}$$

is straightforward, as for $z_{i,r} = z_{i+1,l}$ we have $z^*_{i+\frac{1}{2}} = z_{i,r} = z_{i+1,l}$, $\mathbf{Q}^*_{i,r} = \mathbf{Q}_{i,r}$, and $\mathbf{Q}^*_{i+1,l} = \mathbf{Q}_{i+1,l}$. □

6.2.2 An alternative numerical entropy scheme

In the previous subsection, we have discussed the existing scheme for the NEP. Now, an alternative numerical entropy scheme shall be given in this subsection. In addition, we shall see which scheme is better in producing the NEP.

An alternative form of the entropy inequality for the shallow water equations (2.1) is [7]

$$\tilde{\eta}_t + \tilde{\psi}_x \leq \tilde{\sigma}\,, \tag{6.10}$$

where

$$\tilde{\eta}\left(\mathbf{q}(x,t)\right) = \frac{1}{2}hu^2 + \frac{1}{2}gh^2\,, \tag{6.11}$$

$$\tilde{\psi}\left(\mathbf{q}(x,t)\right) = \left(\frac{1}{2}hu^2 + gh^2\right)u\,, \tag{6.12}$$

$$\tilde{\sigma}\left(\mathbf{q}(x,t), z(x)\right) = -ghuz_x \tag{6.13}$$

are the entropy, entropy flux, and the entropy source respectively for this alternative form of the entropy inequality. This form (6.10) resembles the shallow water equations, that is, if the shallow water equations are nonhomogeneous then the form for the entropy (6.10) is also nonhomogeneous. In addition, if the shallow water equations are homogeneous then the form for the entropy (6.10) is also homogeneous.

Recall the hydrostatic reconstruction (2.3)–(2.5), such that the values for h^* lead to auxiliary values for the conserved quantities $\mathbf{Q}^* = (h^*, h^*u)^T$. We denote the numerical entropy by $\tilde{\Theta}$, and the numerical entropy fluxes on the right and left interface of the ith cell by $\tilde{\Psi}^r$ and $\tilde{\Psi}^l$ respectively. Given the value of $\tilde{\Theta}_i^{n-1} := \tilde{\eta}\left(\mathbf{Q}_i^{n-1}\right)$, we use the semi-discrete scheme

$$\Delta x_i \frac{d}{dt}\tilde{\Theta}_i + \tilde{\Psi}^r(\mathbf{Q}_i, \mathbf{Q}_{i+1}, z_{i,r}, z_{i+1,l}) - \tilde{\Psi}^l(\mathbf{Q}_{i-1}, \mathbf{Q}_i, z_{i-1,r}, z_{i,l}) = \tilde{\Sigma}_i^{(j)} \tag{6.14}$$

to obtain the value of $\tilde{\Theta}_i^n$, where

$$\tilde{\Psi}^r(\mathbf{Q}_i, \mathbf{Q}_{i+1}, z_{i,r}, z_{i+1,l}) := \tilde{\Psi}(\mathbf{Q}^*_{i,r}, \mathbf{Q}^*_{i+1,l}, z^*_{i+\frac{1}{2}}) + \tilde{\Sigma}_{i,r}\,, \tag{6.15}$$

and

$$\tilde{\Psi}^l(\mathbf{Q}_{i-1}, \mathbf{Q}_i, z_{i-1,r}, z_{i,l}) := \tilde{\Psi}(\mathbf{Q}^*_{i-1,r}, \mathbf{Q}^*_{i,l}, z^*_{i-\frac{1}{2}}) + \tilde{\Sigma}_{i,l} \tag{6.16}$$

are the right and left numerical entropy fluxes of the ith cell calculated at $x_{i+\frac{1}{2}}$ and $x_{i-\frac{1}{2}}$ respectively. Here, $\tilde{\Theta}$ is the approximation of the entropy $\tilde{\eta}$, and $\tilde{\Psi}$ is a

consistent numerical entropy flux in the sense that $\tilde{\Psi}(\mathbf{Q}, \mathbf{Q}, z, z) = \tilde{\Psi}(\mathbf{Q}, z)$. In addition,

$$\tilde{\Sigma}_{i,r} := \frac{g}{2} h_{i,r}^2 u_{i,r} - \frac{g}{2}(h_{i,r}^*)^2 u_{i,r}\,, \quad \tilde{\Sigma}_{i,l} := \frac{g}{2} h_{i,l}^2 u_{i,l} - \frac{g}{2}(h_{i,l}^*)^2 u_{i,l} \tag{6.17}$$

are the corrections due to the water height modification in the hydrostatic reconstruction. Furthermore, the index j of $\Sigma_i^{(j)}$ in equation (6.14) denotes the order of the numerical source term. The first and second order numerical source terms are

$$\tilde{\Sigma}_i^{(1)} := 0 \quad \text{and} \quad \tilde{\Sigma}_i^{(2)} := -g \left(\frac{h_{i,r} + h_{i,l}}{2} \right) \left(\frac{u_{i,r} + u_{i,l}}{2} \right) (z_{i,r} - z_{i,l})\,. \tag{6.18}$$

The NEP is then defined by

$$E_i^n = \frac{1}{\Delta t} \left(\tilde{\eta}\left(\mathbf{Q}_i^n\right) - \tilde{\Theta}_i^n \right). \tag{6.19}$$

Here, $\tilde{\Theta}_i^n$ is obtained from the numerical entropy scheme (6.14) with $\tilde{\eta}\left(\mathbf{Q}^{n-1}\right)$ as the input; $\mathbf{Q}_i^n$ is calculated from the finite volume scheme with $\mathbf{Q}^{n-1}$ as the input; and Δt is the time step used in solving the semi-discrete ordinary differential equations (2.6) and (6.14).

In the following theorem, we present properties of the alternative numerical entropy scheme described above related to the steadiness of a lake at rest and its consistency to the entropy equation on smooth regions.

Theorem 6.2. *The semi-discrete numerical scheme (6.14) with fluxes given by (6.15) and (6.16)*

1. *preserves the entropy steady state of a lake at rest, and*
2. *is consistent with the entropy equation, which is expression (6.10) restricted with an equality sign.*

Proof. Assume that we are given a steady state of a lake at rest. Similar to the proof of Theorem 6.1, we have $w_t = 0$ and $u = 0$ everywhere. Now, we consider an arbitrary ith cell. The hydrostatic reconstruction (2.3)–(2.5) and the discrete version of the flux function (6.12) together with $u_i = 0$ imply that

$$\tilde{\Psi}^r(\mathbf{Q}_i, \mathbf{Q}_{i+1}, z_{i,r}, z_{i+1,l}) = \tilde{\Psi}^l(\mathbf{Q}_{i-1}, \mathbf{Q}_i, z_{i-1,r}, z_{i,l}) = \tilde{\Sigma}_i = 0\,. \tag{6.20}$$

Equation (6.20) is a consequence of the use of a consistent numerical flux $\tilde{\Psi}$. Therefore, the entropy is constant with respect to time. Consequently, the entropy steady state of a lake at rest is preserved.

To prove that the scheme (6.14) is consistent, we need to show that the numerical fluxes satisfy the consistency with the exact flux and consistency with the source, as specified by Bouchut et al [2, 6], where the conserved quantities are reconstructed in the first order framework. The proof for consistency with the exact flux

$$\tilde{\Psi}^r(\mathbf{Q},\mathbf{Q},z,z)=\tilde{\Psi}^l(\mathbf{Q},\mathbf{Q},z,z)=\tilde{\psi}\,(\mathbf{Q}) \tag{6.21}$$

is straightforward, as for $z_{i,r}=z_{i+1,l}$ we have $z^*_{i+\frac{1}{2}}=z_{i,r}=z_{i+1,l}\,,\ \mathbf{Q}^*_{i,r}=\mathbf{Q}_{i,r}\,,$ and $\mathbf{Q}^*_{i+1,l}=\mathbf{Q}_{i+1,l}\,.$ For consistency with the source, we need to show that

$$\begin{aligned}\tilde{\Psi}^l(\mathbf{Q}_i,\mathbf{Q}_{i+1},z_{i,r},z_{i+1,l})-\tilde{\Psi}^r(\mathbf{Q}_i,\mathbf{Q}_{i+1},z_{i,r},z_{i+1,l})= &- ghu\Delta z_{i+\frac{1}{2}}\\ &+ o\left(\Delta z_{i+\frac{1}{2}}\right)\end{aligned} \tag{6.22}$$

as $\mathbf{Q}_i,\mathbf{Q}_{i+1}\to\mathbf{Q}$ and $\Delta z_{i+\frac{1}{2}}\to 0\,,$ where $\Delta z_{i+\frac{1}{2}}=z_{i+1}-z_i\,.$ Recalling the fluxes (6.15) and (6.16), at the interface between the ith and $(i+1)$th cell we have

$$\begin{aligned}\tilde{\Psi}^l-\tilde{\Psi}^r &= \tilde{\Psi}^l(\mathbf{Q}_i,\mathbf{Q}_{i+1},z_{i,r},z_{i+1,l})-\tilde{\Psi}^r(\mathbf{Q}_i,\mathbf{Q}_{i+1},z_{i,r},z_{i+1,l})\\ &= \tilde{\Sigma}_{i+1,l}-\tilde{\Sigma}_{i,r}\\ &= \frac{g}{2}h^2_{i+1,l}u_{i+1,l}-\frac{g}{2}(h^*_{i+1,l})^2u_{i+1,l}-\frac{g}{2}h^2_{i,r}u_{i,r}+\frac{g}{2}(h^*_{i,r})^2u_{i,r}\end{aligned} \tag{6.23}$$

As stated by Audusse et al. [2], the maxima in (2.4) and (2.5) do not influence the computations if $h_i-h\,,\ h_{i+1}-h$ and $\Delta z_{i+\frac{1}{2}}$ are small enough, where h is assumed to be positive. Assuming that the velocity u_i and u_{i+1} at the ith and the $(i+1)$th cells are constant denoted by $u\,,$ we then have

$$\frac{g}{2}h^2_{i+1,l}u_{i+1,l}-\frac{g}{2}(h^*_{i+1,l})^2u_{i+1,l} = ghu(z_{i+\frac{1}{2}}-z_{i+1})+o\left(\Delta z_{i+\frac{1}{2}}\right), \tag{6.24}$$

$$-\frac{g}{2}h^2_{i,r}u_{i,r}+\frac{g}{2}(h^*_{i,r})^2u_{i,r} = ghu(z_i-z_{i+\frac{1}{2}})+o\left(\Delta z_{i+\frac{1}{2}}\right). \tag{6.25}$$

Therefore, (6.22) holds. □

6.2.3 Numerical tests

While in Subsections 6.2.1 and 6.2.2 we have discussed numerical schemes for the NEP, this subsection is devoted to numerical tests for the performance of the NEP. The numerical tests are carried out using the Python 2.7 programming language. Before we proceed to the numerical results, we present the numerical setting and flux functions as follows.

In all simulations in this subsection, the numerical setting is as follows. Quantities are measured in SI units. The acceleration due to gravity is taken as $g = 9.81$. The minimum fluid height allowed in the flux computation is $h_{\min} = 10^{-6}$. The minmod limiter is used for quantity reconstruction. The CFL number is 1.0.

In the tests, we use the flux function due to Kurganov et al. [36] for the numerical evolution of the conserved quantity $\mathbf{q}$ and the entropy η. This flux function is defined for homogeneous conservation laws. Since Kurganov et al. [36] have explicitly presented the flux for the numerical evolution of the conserved quantity $\mathbf{q}$, here we write only the flux for the numerical evolution of the entropy η. The flux for the numerical evolution of the entropy η at the $\left(i+\frac{1}{2}\right)$th interface is

$$\Psi_{i+\frac{1}{2}} = \frac{a^+_{i+\frac{1}{2}}\psi(\mathbf{q}^-_{i+\frac{1}{2}}) - a^-_{i+\frac{1}{2}}\psi(\mathbf{q}^+_{i+\frac{1}{2}})}{a^+_{i+\frac{1}{2}} - a^-_{i+\frac{1}{2}}} + \frac{a^+_{i+\frac{1}{2}}a^-_{i+\frac{1}{2}}\left[\eta\left(\mathbf{q}^+_{i+\frac{1}{2}}\right) - \eta\left(\mathbf{q}^-_{i+\frac{1}{2}}\right)\right]}{a^+_{i+\frac{1}{2}} - a^-_{i+\frac{1}{2}}} \tag{6.26}$$

for the evolution of the entropy η if we want to use the numerical entropy scheme (6.4), and numerical flux $\tilde{\Psi}_{i+\frac{1}{2}}(t)$ as

$$\tilde{\Psi}_{i+\frac{1}{2}} = \frac{a^+_{i+\frac{1}{2}}\tilde{\psi}(\mathbf{q}^-_{i+\frac{1}{2}}) - a^-_{i+\frac{1}{2}}\tilde{\psi}(\mathbf{q}^+_{i+\frac{1}{2}})}{a^+_{i+\frac{1}{2}} - a^-_{i+\frac{1}{2}}} + \frac{a^+_{i+\frac{1}{2}}a^-_{i+\frac{1}{2}}\left[\tilde{\eta}\left(\mathbf{q}^+_{i+\frac{1}{2}}\right) - \tilde{\eta}\left(\mathbf{q}^-_{i+\frac{1}{2}}\right)\right]}{a^+_{i+\frac{1}{2}} - a^-_{i+\frac{1}{2}}} \tag{6.27}$$

for the evolution of the entropy $\tilde{\eta}$ if we want to use the numerical entropy scheme (6.14). Here,

$$a^+_{i+\frac{1}{2}} = \max\left\{u^-_{i+\frac{1}{2}} + \sqrt{g\left(h^-_{i+\frac{1}{2}}\right)^*}, u^+_{i+\frac{1}{2}} + \sqrt{g\left(h^+_{i+\frac{1}{2}}\right)^*}, 0\right\}, \tag{6.28}$$

$$a^-_{i+\frac{1}{2}} = \min\left\{u^-_{i+\frac{1}{2}} - \sqrt{g\left(h^-_{i+\frac{1}{2}}\right)^*}, u^+_{i+\frac{1}{2}} - \sqrt{g\left(h^+_{i+\frac{1}{2}}\right)^*}, 0\right\}, \tag{6.29}$$

and the starred variables follow from the hydrostatic reconstruction (2.3)–(2.5). In addition,

$$\mathbf{q}^+_{i+\frac{1}{2}} = \mathbf{p}_{i+1}(x_{i+\frac{1}{2}}, t) \quad \text{and} \quad \mathbf{q}^-_{i+\frac{1}{2}} = \mathbf{p}_i(x_{i+\frac{1}{2}}, t) \tag{6.30}$$

are the right and the left values at $x = x_{i+\frac{1}{2}}$ of a conservative non-oscillatory piecewise polynomial interpolated vector

$$\tilde{\mathbf{q}}(x,t) \;=\; \sum_i \mathbf{p}_i(x,t)\mathcal{X}_i\,, \tag{6.31}$$

reconstructed at each time step based on the previously computed cell averages, $\{\mathbf{Q}_i^n(t)\}$, where

$$\mathbf{Q}_i^n(t) = \frac{1}{\Delta x}\int_{x_{i-\frac{1}{2}}}^{x_{i+\frac{1}{2}}} \mathbf{q}(x, t^n)dx\,. \tag{6.32}$$

The set $\{\mathbf{p}_i(\cdot, t)\}$ consists of vectors with polynomials of a given degree as their components, and $\mathcal{X}_i$ is the characteristic function for the ith cell.

Now, we proceed to the results of the numerical tests. We present the results in three parts: (a) existing NEP scheme versus alternative NEP scheme, (b) NEP versus other indicators called weak local residuals, and (c) NEP in adaptive methods.

(a) Existing scheme versus alternative scheme

To begin the tests, we compare the performance of the NEP produced by the existing scheme with that by the alternative scheme. We use the second order source, second order spatial, and second order temporal discretisations. Two test problems are considered.

As the first test problem, we consider the collapse of a reservoir on a horizontal topography

$$z(x) = 0\,, \quad \text{for} \quad 0 < x < 2000\,, \tag{6.33}$$

and an initial condition

$$u(x,0) = 0\,, \quad w(x,0) = \begin{cases} 0 & \text{if} \quad 0 < x < 500\,, \\ 10 & \text{if} \quad 500 < x < 1500\,, \\ 5 & \text{if} \quad 1500 < x < 2000\,. \end{cases} \tag{6.34}$$

The simulation is done to illustrate the motion of the water at any point x in the domain and at any time $t > 0$ with respect to the initial condition (6.34). Note that the condition (6.34) means that two dam walls (at $x = 500$ and $x = 1500$) are given initially. Here the spatial domain is descretised into 400 cells uniformly.

Figure 6.1 shows the simulation result at time $t = 20$. A shock occurs and moves to the right (see Chapter 4 for an analytical work relating to this kind of shock). In this simulation, we name NEP_E for the NEP defined by (6.7) and NEP_A for the NEP defined by (6.19). For this simulation with horizontal bed topography, both NEP_E and NEP_A have exactly the same value of indicators. This means that their performance are the same in this case.

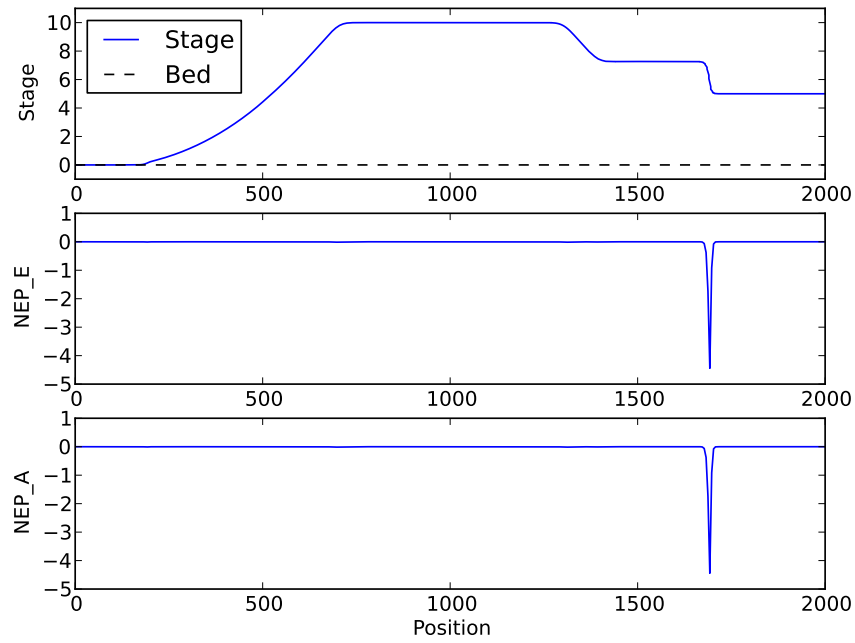

Figure 6.1: A moving shock after dam break at $t = 20$ using the second order method. Stage w is the free surface; NEP_E is as in (6.7); and NEP_A is as in (6.19).

As the second test problem, we consider a channel of length 25 with topography (having a parabolic bump)

$$z(x) = \begin{cases} 0.2 - 0.05\,(x-10)^2 & \text{if} \quad 8 \le x \le 12\,, \\ 0 & \text{otherwise}\,, \end{cases} \tag{6.35}$$

and an initial condition

$$u(x,0) = 0\,, \quad w(x,0) = 0.33 \tag{6.36}$$

together with the Dirichlet boundary conditions

$$[w, hu, z, h, u] = [0.42, 0.18, 0.0, 0.42, 0.18/0.42] \quad \text{at} \quad x = 0^-\,, \tag{6.37}$$

$$[w, hu, z, h, u] = [0.33, 0.18, 0.0, 0.33, 0.18/0.33] \quad \text{at} \quad x = 25^+\,. \tag{6.38}$$

Physically, the boundary conditions mean that there is a source of flow upstream quantified by (6.37) at the point $x = 0^-$ and at the same time there exists a sink of flow downstream quantified by (6.38) at the point $x = 25^+$. Here the spatial domain is descretised into 400 cells uniformly.

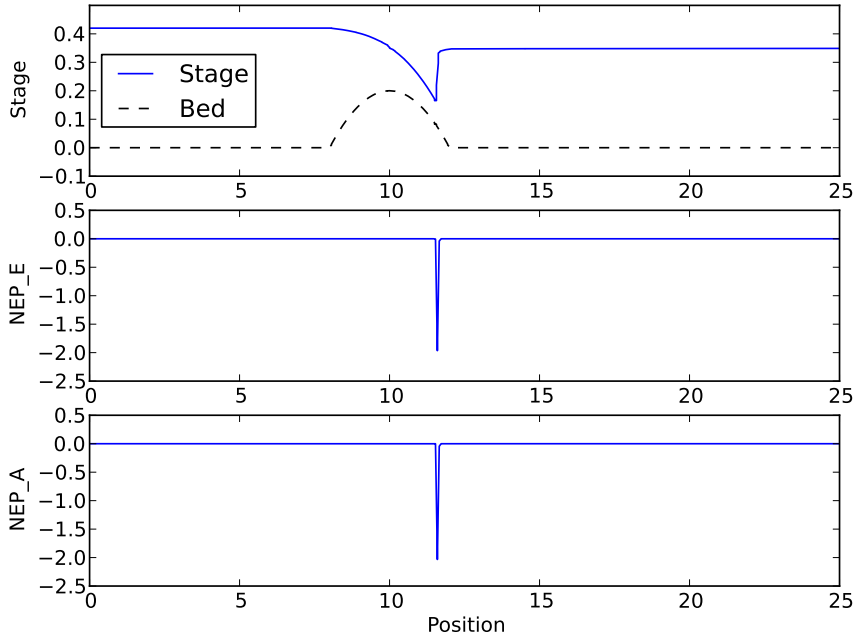

Figure 6.2: A stationary shock over a parabolic obstruction at $t = 50$ using the second order method. Stage w is the free surface; NEP_E is as in (6.7); and NEP_A is as in (6.19).

Figure 6.2 shows the simulation result at time $t = 50$. A stationary shock occurs on the parabolic obstruction. The same as in the previous simulation, we name NEP_E for the NEP defined by (6.7) and NEP_A for the NEP defined by (6.19). We see that NEP_E and NEP_A perform the same for this test case.

Based on the two representatives of test problems above, NEP defined by (6.7) and that by (6.19) produce the same behaviour. In the next tests of this section (Section 6.2), we use (6.7) to compute the NEP because the formulation is simpler than (6.19).

(b) Numerical entropy production versus weak local residuals

Now, we shall compare the performance of the numerical entropy production (NEP) to Karni, Kurganov, and Petrova's (KKP) weak local residual [33] of the mass of water and Constantin and Kurganov's (CK) weak local residual [16] of

the mass of water. The KKP indicator is defined at $(x,t) = (x_i, t^n)$ by

$$\begin{aligned} E_i^n &= (1/12)\left\{\Delta x\left[h_{i+1}^{n+1} - h_{i+1}^{n-1} + 4\left(h_i^{n+1} - h_i^{n-1}\right) + h_{i-1}^{n+1} - h_{i-1}^{n-1}\right]\right. \\ &\quad +\Delta t\left[h_{i+1}^{n+1}u_{i+1}^{n+1} - h_{i-1}^{n+1}u_{i-1}^{n+1} + 4\left(h_{i+1}^{n}u_{i+1}^{n} - h_{i-1}^{n}u_{i-1}^{n}\right)\right. \\ &\quad \left.\left. + h_{i+1}^{n-1}u_{i+1}^{n-1} - h_{i-1}^{n-1}u_{i-1}^{n-1}\right]\right\}, \end{aligned} \tag{6.39}$$

whereas the CK indicator is defined at $(x,t) = (x_{i+1/2}, t^{n-1/2})$ by

$$\begin{aligned} E_{i+1/2}^{n-1/2} &= (1/2)\left\{\Delta x\left[h_i^n - h_i^{n-1} + h_{i+1}^n - h_{i+1}^{n-1}\right]\right. \\ &\quad \left.+\Delta t\left[h_{i+1}^{n-1}u_{i+1}^{n-1} - h_i^{n-1}u_i^{n-1} + h_{i+1}^n u_{i+1}^n - h_i^n u_i^n\right]\right\}. \end{aligned} \tag{6.40}$$

The order of accuracy for the KKP indicator (6.39) in a rough region is lower than the order of accuracy in a smooth region [33], and the same is true [16] for the CK indicator (6.40). Therefore, the KKP and CK indicators can also be used as smoothness indicators or shock detectors. We shall discuss weak local residuals (the KKP and CK indicators) in more detail in Chapter 7.

We consider one test involving a moving shock and another test involving a stationary shock in order to judge the performance of the numerical entropy production in detecting shocks. We use the second order source, second order spatial, and second order temporal discretisations.

As the first test problem, we consider the collapse of a reservoir on a horizontal topography

$$z(x) = 0\,, \quad 0 < x < 2000\,, \tag{6.41}$$

and an initial condition

$$u(x,0) = 0\,, \quad w(x,0) = \begin{cases} 0 & \text{if} \quad 0 < x < 500\,, \\ 10 & \text{if} \quad 500 < x < 1500\,, \\ 5 & \text{if} \quad 1500 < x < 2000\,. \end{cases} \tag{6.42}$$

The simulation is done to illustrate the motion of the water at any point x in the domain and at any time $t > 0$ with respect to the initial condition (6.42). Note that the condition (6.42) means that two dam walls (at $x = 500$ and $x = 1500$) are given initially.

The simulated water surface (stage) at time $t = 20$ is shown in Figure 6.3. Also shown in Figure 6.3 are the corresponding CK, KKP, and NEP indicators. Here the spatial domain is uniformly discretised into 400 cells. These results indicate the superiority of the numerical entropy production as a shock detector when

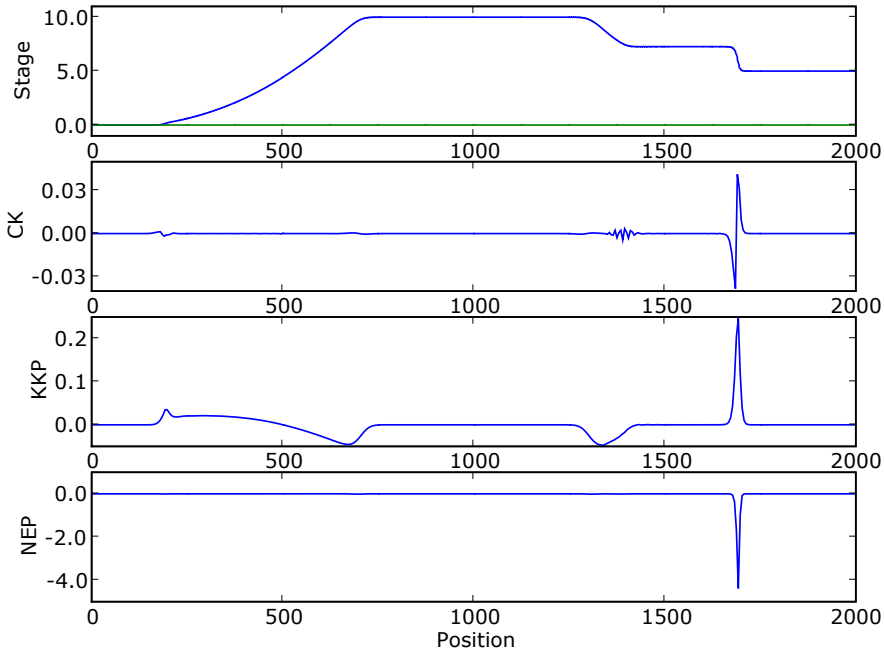

Figure 6.3: A moving shock after dam break at $t = 20$ using the second order method. Stage w is the free surface; CK is as in (6.40); KKP is as in (6.39); NEP is as in (6.7).

the problem has an unsteady state solution. We see that the magnitude of the NEP is large around the location of the shock and almost zero on the rest of the spatial domain, whereas the CK and the KKP indicators, although large around the location of the shock, also exhibit obvious ripples away from the shock in this simulation. Note that sharp curves of the CK, KKP, and NEP indicators occur only on the region corresponding to the shock, because, as mentioned above, the orders of accuracy of the indicators are lower at the region of the shock than in smooth regions. The supplementary file[†] *moving-shock.avi* contains a movie of this first simulation for time $t \in [0, 20]$.

As the second test problem, we consider a channel of length 25 with topography (having a parabolic bump)

$$z(x) = \begin{cases} 0.2 - 0.05\,(x-10)^2 & \text{if} \quad 8 \le x \le 12\,, \\ 0 & \text{otherwise}\,, \end{cases} \tag{6.43}$$

[†]The supplementary file is available at `http://journal.austms.org.au/ojs/index.php/ANZIAMJ/rt/suppFiles/3786/0`.

and an initial condition

$$u(x,0) = 0\,, \quad w(x,0) = 0.33 \tag{6.44}$$

together with the Dirichlet boundary conditions

$$[w, hu, z, h, u] = [0.42, 0.18, 0.0, 0.42, 0.18/0.42] \quad \text{at} \quad x = 0^-\,, \tag{6.45}$$

$$[w, hu, z, h, u] = [0.33, 0.18, 0.0, 0.33, 0.18/0.33] \quad \text{at} \quad x = 25^+\,. \tag{6.46}$$

Physically, the boundary conditions mean that there is a source of flow upstream quantified by (6.45) at the point $x = 0^-$ and at the same time there exists a sink of flow downstream quantified by (6.46) at the point $x = 25^+$.

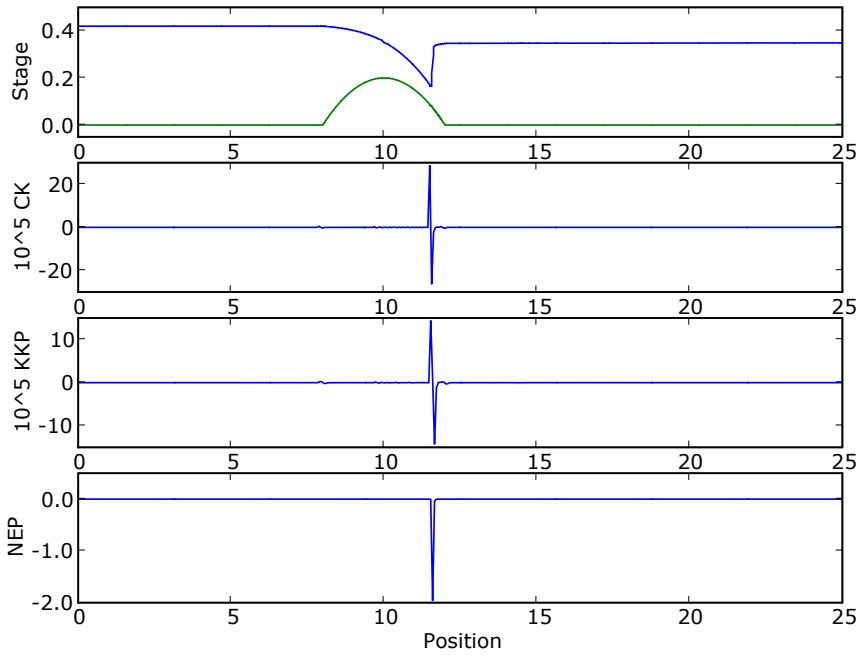

Figure 6.4: A stationary shock over a parabolic obstruction at $t = 50$ using the second order method. Stage w is the free surface; NEP is as in (6.7). The notation 10^5 CK and 10^5 KKP mean 10^5 times CK and 10^5 times KKP respectively, where CK is as in (6.40) and KKP is as in (6.39).

Figure 6.4 shows the steady state water surface as well as the corresponding CK, KKP, and NEP indicators at time $t = 50$. Here the spatial domain is uniformly discretised into 400 cells. These results demonstrate the superiority of

the numerical entropy production as a shock detector when the problem has a steady state solution. We see that the magnitude of the NEP is large around the location of the shock and approximately zero on the rest of the spatial domain, whereas the CK and the KKP indicators, although large around the location of the shock, also exhibit small ripples on the location of the parabolic bump in this test case. The supplementary file[‡] *steady-shock.avi* contains a movie of this second simulation for time $t \in [0, 100]$.

In relation to this flow over a parabolic obstruction, we note the following remark.

Remark 6.3. In our simulation, the upstream flow is subcritical and a shock is formed on the parabolic obstruction. However, in general, for large time a shock may or may not be formed, depending on the boundary conditions on both the left and the right ends of the domain. This was described by Houghton and Kasahara [29] as well as Goutal and Maurel [26]. As the boundary conditions are fixed as Dirichlet-type, for large time, the flow gets steady regardless the upstream and downstream Froude numbers, and there is not a train of waves.

Based on the two representatives of test problems above, the NEP performs slightly better than weak local residuals in detecting smoothness of solutions.

(c) Numerical entropy production in adaptive methods

Now, we shall implement NEP into adaptive-mesh finite volume methods used to solve a one-dimensional problem. We use the first order source, first order spatial, and first order temporal discretisations.

Recall that NEP is $O(1/\Delta x)$ around a shock and $O((\Delta x)^r)$ at smooth regions, where r is the order of accuracy of the numerical method at smooth regions [56, 57]. Note that the adaptive method we implement is first order. We introduce the term *normalised NEP* and define it as

$$\epsilon_i^n = \frac{E_i^n}{\Delta x_i}\,, \tag{6.47}$$

where E_i^n is the NEP at the ith cell at time $t = t^n$. The normalised NEP (6.47) or nNEP in short is then $O(1)$ around a shock and $O((\Delta x)^2)$ at smooth regions.

[‡]The supplementary file is uploaded at `http://journal.austms.org.au/ojs/index.php/ANZIAMJ/rt/suppFiles/3786/0`.

The one-dimensional flow problem to be solved adaptively is as follows. This problem was used by Felcman and Kadrnka [23] as a test case for their adaptive method. Consider a channel of length 25 with topography

$$z(x) = \begin{cases} 0.2 - 0.05\,(x-10)^2 & \text{if} \quad 8 \le x \le 12\,, \\ 0 & \text{otherwise}\,, \end{cases} \tag{6.48}$$

and an initial condition

$$u(x,0) = 0\,, \quad w(x,0) = 0.66 \tag{6.49}$$

together with the Dirichlet boundary conditions

$$h(25,t) = 0.66\,, \quad hu(0,t) = hu(25,t) = 1.53\,. \tag{6.50}$$

The spatial domain is discretised into 100 cells initially. The tolerance of the normalised NEP indicator is

$$\mathrm{nNEP}_{\mathrm{tol}} = 0.05 \max |\epsilon|\,, \tag{6.51}$$

where ϵ is the nNEP, that is, NEP normalised locally by the cell width as defined in (6.47). Cells with $|\mathrm{nNEP}| > \mathrm{nNEP}_{\mathrm{tol}}$ are refined, whereas those with $|\mathrm{nNEP}| \le 0.1\,\mathrm{nNEP}_{\mathrm{tol}}$ are coarsened. Two neighbouring cells are coarsened as long as they have the same parent and are at the same level. The maximum level of binary refinement is 10 and the width of the coarsest cell allowed is 0.25.

Figure 6.5 shows the flow over a parabolic obstruction at time $t = 2.67$, where at this time, the number of cells is 149. We see that refinements are apparent around the shock moving to the right passing the bump and the shock next to the right boundary. The later shock is artificial due to the enforced right boundary condition. Obviously, a very sharp moving shock passing the bump is achieved in the numerical solution shown in Figure 6.5.

In comparison, we simulate the same problem using 298 uniform cells with a nonadaptive method. The fixed number of cells is two times the number of cells of the result shown in Figure 6.5. However, we find that the nonadaptive method cannot resolve the sharpness of the moving shock, as shown in Figure 6.6. This is because the nonadaptive method distributes the cells uniformly over the whole domain. On the other hand, the adaptive method has a coarse discretisation at smooth regions and a very fine discretisation at rough (nonsmooth) regions. Note that smooth regions do not need a fine discretisation.

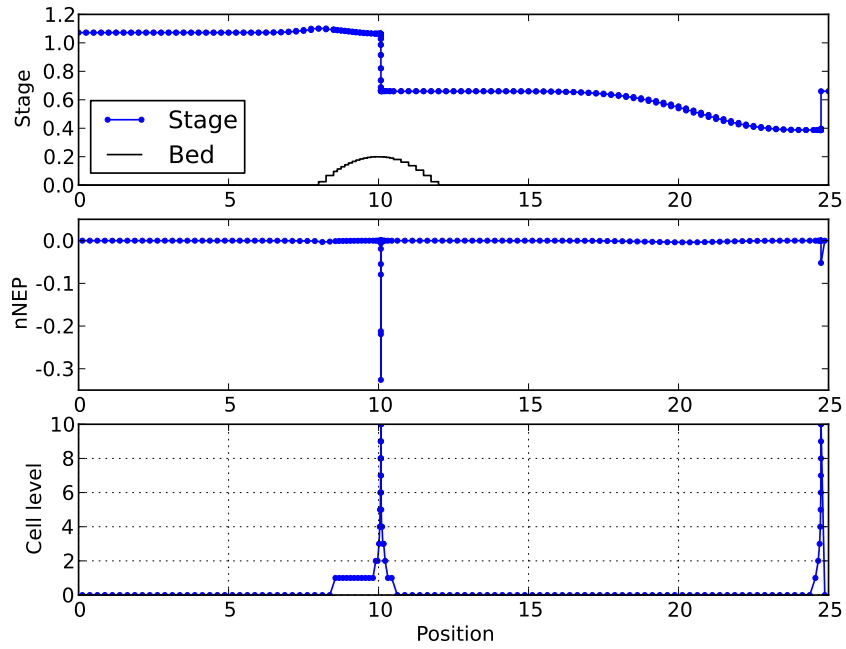

Figure 6.5: Flow over a parabolic obstruction at time $t = 2.67$ using the first order adaptive method with the NEP indicator. At this time the number of cells is 149. nNEP is defined as in (6.47). Here $\text{nNEP}_{\text{tol}} = 0.05 \max |\text{nNEP}|$.

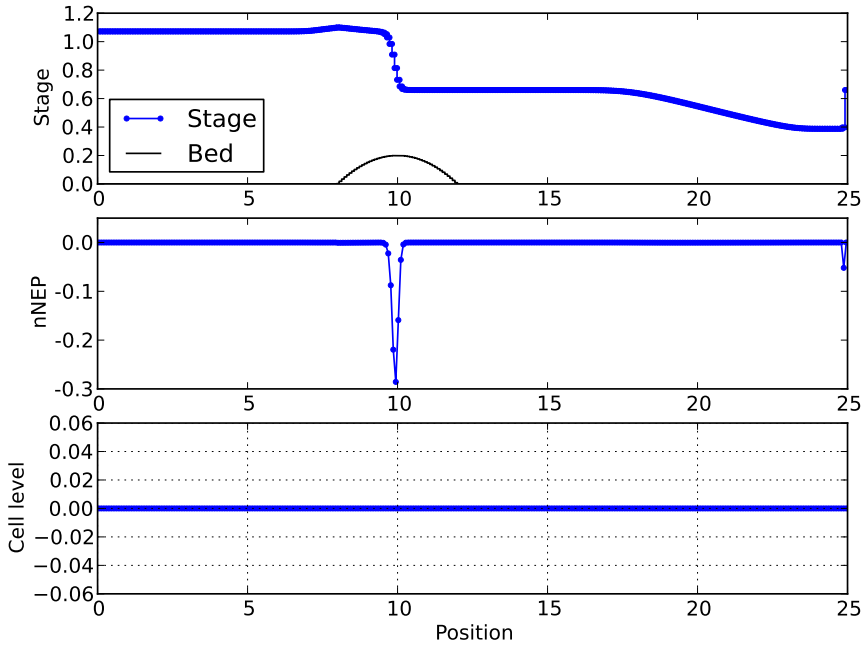

Figure 6.6: Flow over a parabolic obstruction at time $t = 2.67$ using 298 uniform cells with the first order nonadaptive method. nNEP is defined as in (6.47).

In summary of this section, NEP is successful to be a smoothness or refinement indicator in one dimension.

6.3 Numerical entropy production in 1.5D

Now, we shall extend the NEP definition for one-and-a-half dimensions following from the NEP definition given in the previous section for one dimension. We present governing equations and explain numerical schemes we use in Subsection 6.3.1. Then numerical results are given in Subsection 6.3.2.

6.3.1 Governing equations and numerical schemes

The shallow water equations involving shear velocity or transverse velocity are usually called the one-and-a-half-dimensional shallow water equations [7]. These equations can also be understood as a model for water flows with a passive tracer. The dynamics of the passive tracer are governed by an additional transport or advection equation. The transverse velocity is actually the concentration of the passive tracer, which does not influence the fluid dynamics of the one-dimensional shallow water equations. The one-and-a-half-dimensional equations are

$$\mathbf{q}_t + \mathbf{f}(\mathbf{q})_x = \mathbf{s}\,, \tag{6.52}$$

where the conserved quantity $\mathbf{q}$, flux $\mathbf{f}$, and source $\mathbf{s}$ are

$$\mathbf{q} = \begin{bmatrix} h \\ hu \\ hv \end{bmatrix}, \quad \mathbf{f} = \begin{bmatrix} hu \\ hu^2 + \frac{1}{2}gh^2 \\ huv \end{bmatrix}, \quad \text{and} \quad \mathbf{s} = \begin{bmatrix} 0 \\ -ghz_x \\ 0 \end{bmatrix}. \tag{6.53}$$

respectively. Here $v(x)$ is the horizontal velocity orthogonal to the x-axis. For the passive tracer model, $v(x)$ is the concentration of the passive tracer.

The entropy inequality for (6.52) is [7]

$$\eta_t + \psi_x \leq 0\,, \tag{6.54}$$

where

$$\eta\left(\mathbf{q}(x,t), z(x)\right) = \frac{1}{2}h(u^2+v^2) + \frac{1}{2}gh^2 + ghz\,, \tag{6.55}$$

$$\psi\left(\mathbf{q}(x,t), z(x)\right) = \left(\frac{1}{2}h(u^2+v^2) + gh^2 + ghz\right)u\,, \tag{6.56}$$

are the entropy and the entropy flux.

We can use the existing numerical entropy scheme described in Subsection 6.2.1 where the variables involved are (6.53). This is because the form of the entropy inequality (6.54) is the same as that of (6.1).

To solve the one-and-a-half-dimensional shallow water system numerically, we may use a standard numerical solver for balance laws by considering the system as a single-coupled system. However, to get a more accurate solution around contact discontinuities, we choose to decouple the advection equation from the system. This means that we solve the one-dimensional shallow water part independent from the advection part. The advection part is solved using upwind flux computation based on the sign of the mass flux, where the mass flux is the flux of the mass equation $h_t + (hu)_x = 0$. This technique was introduced by Larrouturou [37] for gas dynamics and was used by Bouchut [6, 7] for shallow water models. We implement this technique in numerical tests for one-and-a-half-dimensional problems.

6.3.2 Numerical tests

Now, we shall do two numerical tests in one-and-a-half dimensions. One test is to verify the ability of NEP to detect the smoothness of solutions. Another test is to confirm that NEP is applicable to adaptive methods. The numerical tests are carried out using the Python 2.7 programming language.

As the first test, we consider a dam break with a passive tracer and obstruction. We consider a channel of length 2000 with topography (having a parabolic bump)

$$z(x) = \begin{cases} 2 - 0.005\,(x - 1050)^2 & \text{if} \quad 1030 \leq x \leq 1070\,, \\ 0 & \text{otherwise}\,. \end{cases} \tag{6.57}$$

The initial condition is

$$u(x,0) = 0\,, \quad v(x,0) = \begin{cases} 1 & \text{if} \quad 0 < x < 1000\,, \\ 0 & \text{if} \quad 1000 < x < 2000\,, \end{cases} \tag{6.58}$$

$$w(x,0) = \begin{cases} 10 & \text{if} \quad 0 < x < 1000\,, \\ 5 & \text{if} \quad 1000 < x < 2000\,. \end{cases} \tag{6.59}$$

Here the spatial domain is descretised into 1600 cells uniformly.

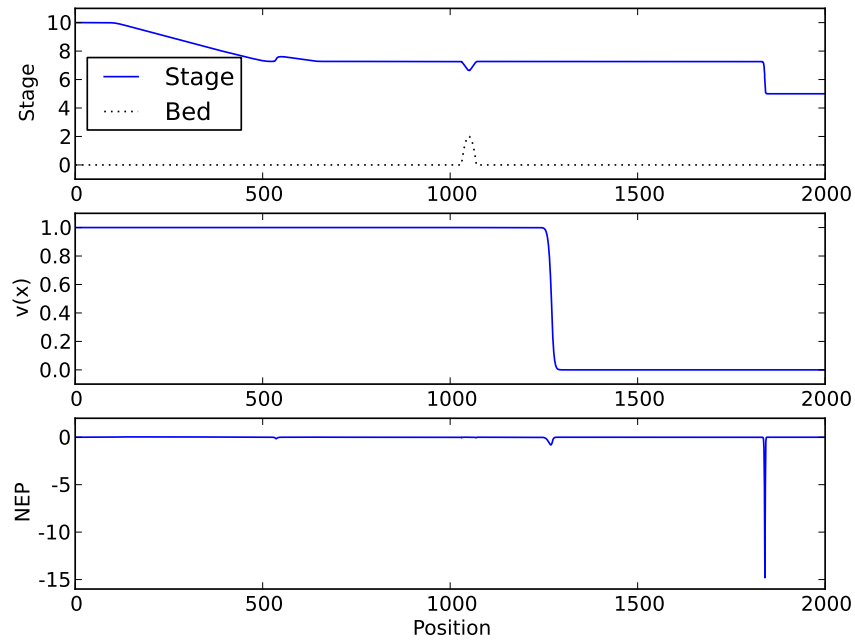

Figure 6.7: The dam-break problem with a parabolic obstruction at $t = 90.0$ using the second order method and 1600 cells.

Figure 6.7 shows the simulation results at time $t = 90$ using the second order method. The NEP clearly detects the positions of the shock and contact discontinuity moving to the right.

As the second test, we solve the following one-and-a-half flow problem adaptively. The second problem is similar to the first, but here we use horizontal topography for simplicity and a different initial condition as follows. We consider a dam break problem involving a passive tracer with horizontal topography

$$z(x) = 0\,, \quad \text{for} \quad x \in [-2000, 2000]\,. \tag{6.60}$$

The initial condition is

$$u(x,0) = 0\,, \quad v(x,0) = \begin{cases} 3 & \text{if} \quad -2000 < x < 0\,, \\ 0 & \text{if} \quad 0 < x < 2000\,, \end{cases} \tag{6.61}$$

$$w(x,0) = \begin{cases} 10 & \text{if} \quad -2000 < x < 0\,, \\ 4 & \text{if} \quad 0 < x < 2000\,. \end{cases} \tag{6.62}$$

We vary the initial condition in this second problem from the first one to show

that the NEP can still detect the smoothness of the solution regardless of the variations.

The setting parameters are as follow. The spatial domain is discretised uniformly at time $t = 0$ into 16 cells, and we consider that all initial cells have cell level of 0. The maximum level of binary refinement allowed is 10, which means that an initial cell is allowed to be binary refined ten times. One refinement on a cell (parent) generates two new cells (children) having one level up from the level of the parent, that is, the widths of the child-cells are a half width of the parent-cell. The NEP tolerance is taken as $\mathrm{nNEP}_{\mathrm{tol}} = 0.01 \max |\mathrm{nNEP}|$.

The cell adaptation is performed at each time step as follows. If a cell has NEP absolute value larger than 10 times $\mathrm{NEP}_{\mathrm{tol}}$ and its level is less than the maximum level allowed then we do refinement. If two neighbouring cells have NEP absolute values less than $\mathrm{NEP}_{\mathrm{tol}}$, are at the same level, and have the same parents then we do coarsening.

To solve this problem numerically, we may use the same numerical flux formulation for all three (mass, momentum, and transport) equations. However, to get a more accurate solution at the contact discontinuity of the tracer solution, we choose to apply the standard flux formulation only to mass and momentum equations (In particular, we choose the flux function due to Kurganov, Noelle and Petrova [36]). For the passive transport flux, we choose an upwind flux based on $v(x)$ as suggested by Bouchut [7]. The passive transport flux is

$$F^{hv}_{i+1/2} = \begin{cases} F^{h}_{i+1/2} v_i & \text{if} \quad F^{h}_{i+1/2} \geq 0 \,, \\ F^{h}_{i+1/2} v_{i+1} & \text{otherwise} \,, \end{cases} \tag{6.63}$$

where $F^{h}_{i+1/2}$ is the mass flux at $x = x_{i+1/2}$.

A representative of the simulation results is given in Figure 6.8 for time $t = 90$. The cell levels at the rarefaction and the contact discontinuity decrease as the time evolves. We note that if we decrease $\mathrm{NEP}_{\mathrm{tol}}$ to a smaller value, the cell levels at the rarefaction and the contact discontinuity can remain at the highest level. We see that the adaptive method can resolve the sharpness of shock and contact discontinuities. We conclude from these results that the contact discontinuity is more diffusive than the shock. This is consistent with the theory [28] and results in gas dynamics [56, 57]. Furthermore, we notice in Figure 6.8 that, small positive overshoots of the NEP occur around the contact discontinuity. We shall not discuss this positive overshoot phenomenon in detail in this thesis, as this is research in progress. Some related results have been submitted for

publication [51], but again, they are not part of this thesis. In the following two remarks we mention some notes about positive overshoots of the NEP in one-and-a-half dimensions.

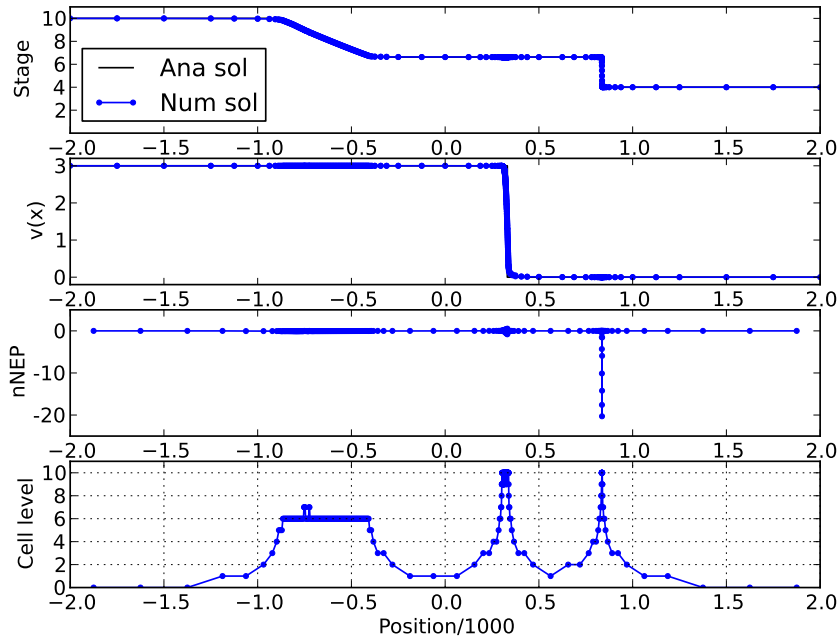

Figure 6.8: The dam-break problem with passive tracer at $t = 90$ using the first order adaptive method with the NEP indicator. The water surface and concentration $v(x)$ of tracer is viewed based on the values at vertices of cells, while the others are at centroids of cells. "Ana sol" and "Num sol" stand for analytical solution and numerical solution.

Remark 6.4. Note that we use the flux function due to Kurganov, Noelle, and Petrova [36] for mass and momentum equations and we choose to use an upwind flux based on $v(x)$ for solving the transport equation in the one-and-a-half dimensional problem as suggested by Bouchut [7]. This choice (technique) indeed leads to a more accurate tracer solution and sharper contact discontinuity. With this choice we notice that positive overshoots of the NEP occur around the contact discontinuity. Puppo and Semplice [56, 57] have developed a theory on this positive overshoot phenomenon, but only for the scalar conservation law and only for the Lax-Friedrichs flux.

Remark 6.5. For some experiments we see that if the Lax-Friedrichs flux is

used instead, the occuring positive overshoots are very much smaller in the case of solving the one-and-a-half dimensional problem.

To conclude this section, the NEP is successful in indicating the smoothness of solutions and applicable in adaptive methods in one-and-a-half dimensions.

6.4 Numerical entropy production in 2D

In the previous two sections we have discussed the NEP in one and one-and-a-half dimensions respectively. In this section, we extend the formulation of NEP to two dimensions. Numerical tests shall also be performed to investigate the performance of NEP in two dimensions.

6.4.1 Numerical entropy scheme

The two-dimensional shallow water equations are

$$\mathbf{q}_t + \mathbf{f}(\mathbf{q})_x + \mathbf{g}(\mathbf{q})_y = \mathbf{s}\,, \tag{6.64}$$

where $\mathbf{q} = [h\ uh\ vh]^T$ is the vector of conserved quantities consisting of water depth h, x-momentum uh, and y-momentum vh. Here, u and v are velocities in the x- and y-direction; $\mathbf{f}(\mathbf{q})$ and $\mathbf{g}(\mathbf{q})$ are flux functions in the x- and y-direction given by

$$\mathbf{f}(\mathbf{q}) = \begin{bmatrix} uh \\ u^2h + \frac{1}{2}gh^2 \\ uvh \end{bmatrix} \tag{6.65}$$

and

$$\mathbf{g}(\mathbf{q}) = \begin{bmatrix} vh \\ vuh \\ v^2h + \frac{1}{2}gh^2 \end{bmatrix}; \tag{6.66}$$

the source term is

$$\mathbf{s} = \begin{bmatrix} 0 \\ -ghz_x \\ -ghz_y \end{bmatrix} \tag{6.67}$$

where $z(x, y)$ is the bed topography and g is the acceleration due to gravity. Note that the stage (absolute water level) w is given by $w := z + h$. We describe how to solve (6.64) in Appendix A.

The entropy inequality for equations (6.64) is [7]

$$\eta_t + \psi_x + \phi_y \leq 0\,, \tag{6.68}$$

where the entropy is

$$\eta\left(\mathbf{q}(x,y,t), z(x,y)\right) = \frac{1}{2}h(u^2+v^2) + \frac{1}{2}gh^2 + ghz\,, \tag{6.69}$$

and entropy fluxes are

$$\psi\left(\mathbf{q}(x,y,t), z(x,y)\right) = \left(\frac{1}{2}h(u^2+v^2) + gh^2 + ghz\right)u\,, \tag{6.70}$$

$$\phi\left(\mathbf{q}(x,y,t), z(x,y)\right) = \left(\frac{1}{2}h(u^2+v^2) + gh^2 + ghz\right)v\,. \tag{6.71}$$

For a smooth solution, (6.68) becomes an equality and is called the entropy equation.

To compute the NEP we need to numerically evolve the entropy based on entropy inequality (6.68) at the same time as the evolution of the conserved quantities. For two-dimensional problems, we choose to discretise the spatial domain into polygonal grids. Then for an arbitrary cell i, we have a semi-discrete scheme for the entropy evolution

$$\frac{d\Theta_i}{dt} + \frac{1}{A_i}\sum_{j\in\mathcal{N}(i)} \Psi_{ij}\, l_{ij} \leq 0\,. \tag{6.72}$$

The notation ij is the edge (interface) between the i and j cells. Here Θ_i is an approximation of the averaged entropy over the i cell, Ψ_{ij} is the outward normal entropy flux across the edge ij, and l_{ij} is the length of the edge ij. In addition, $\mathcal{N}(i)$ is the set of neighbouring cells of the i cell. The flux Ψ_{ij} is evaluated using a consistent numerical flux function $\Psi(\cdot,\cdot)$ such that for all values of Θ

$$\Psi(\Theta,\Theta) = \Psi(\Theta)\,. \tag{6.73}$$

Furthermore,

$$\Psi_{ij} = \Psi(\Theta_i(m_{ij}), \Theta_j(m_{ij})) \tag{6.74}$$

where m_{ij} is the midpoint of the ij edge.

Again the NEP is computed as

$$E_i^n = \frac{1}{\Delta t}\left(\eta\left(\mathbf{Q}_i^n\right) - \Theta_i^n\right). \tag{6.75}$$

Here, Θ_i^n is obtained from the numerical entropy scheme (6.72) with $\eta\left(\mathbf{Q}^{n-1}\right)$ as the input; $\mathbf{Q}_i^n$ is calculated from the finite volume scheme with $\mathbf{Q}^{n-1}$ as the input; and Δt is the time step used in solving the semi-discrete ordinary differential equations (A.5) and (6.72).

6.4.2 Numerical tests

Now, we shall implement the NEP to an adaptive mesh finite volume method used to solve the two-dimensional shallow water equations on unstructured triangular grids. Recall that NEP has a lower degree of accuracy around nonsmooth regions than smooth ones [56, 57]. The difference between the degree of accuracy between smooth and nonsmooth regions makes the NEP able to detect the smoothness of the numerical solution. Therefore, we are confident to implement the NEP as a smoothness indicator in the adaptive mesh finite volume method.

The numerical tests in this subsection are performed using the MATLAB programming language. Our adaptive mesh finite volume method uses *i*FEM (an innovative finite element method package in MATLAB) as the underlying data structure. We stress that *i*FEM and its data structure are not of our work, but they were developed by Chen [13]. Even though *i*FEM was originally developed for finite element methods, we can still use it for finite volume methods. This is because what we need is actually the data structure of *i*FEM. Therefore, we can adapt the original *i*FEM into our finite volume problems. A brief description of *i*FEM's data structure is given in Appendix B. We shall consider two numerical tests using a first order method.

As the first test problem, we consider a planar dam break problem. This is a one-dimensional flow simulated in two-dimensional framework. We take a spatial domain defined by $(x, y) \in [-1, 1] \times [-1, 1]$. The domain is discretised into 2048 triangular cells initially. The initial condition is

$$u(x, y, 0) = 0\,, \quad v(x, y, 0) = 0\,, \tag{6.76}$$

$$w(x, y, 0) = \begin{cases} 0.5 & \text{if} \quad x < 0\,, \\ 0.2 & \text{otherwise}\,. \end{cases} \tag{6.77}$$

We take a fixed time step $\Delta t = 0.002$ with 100 iterations. The maximum level of refinement or coarsening is 2, which leads to five different areas of cells after refinement or coarsening. This is because an original initial triangular cell can be refined or coarsened up to two levels finer or two levels coarser. The NEP tolerance is $\mathrm{NEP}_{\mathrm{tol}} = 0.25 \max |\mathrm{NEP}|$.

Representative simulation results are shown in Figure 6.9 and Figure 6.10. We see that fine grids occur around shock and rarefaction regions in order to get accurate solutions at those regions. Coarser grids occur in smooth regions having flat water surface in this case. At this time ($t = 0.2$), the number of cells is 1544.

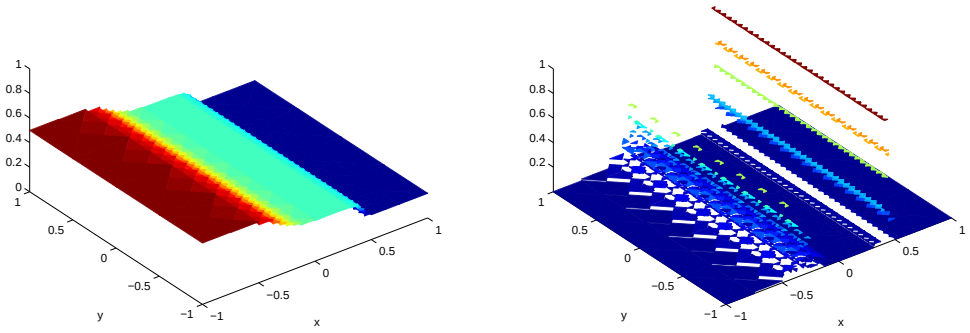

Figure 6.9: The stage and error indicator of the planar dam-break problem at $t = 0.2$ using the first order adaptive method with the NEP indicator. The subfigure on the left is the water surface, while on the right is $-\text{NEP}/\max|\text{NEP}|$. The base planes are the xy-plane.

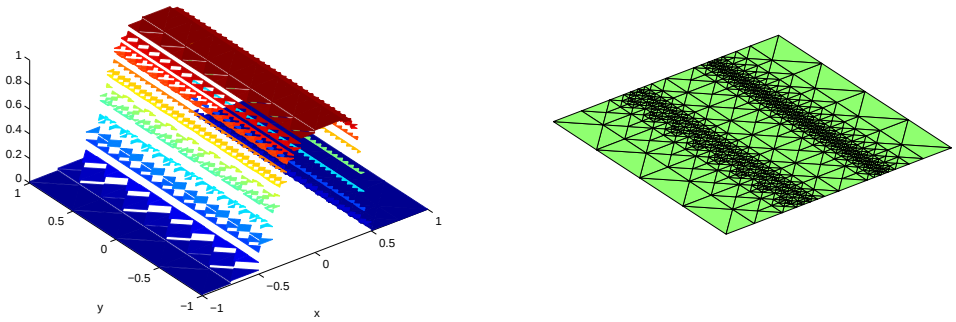

Figure 6.10: The x-momentum and mesh of the planar dam-break problem at $t = 0.2$ using the first order adaptive method with the NEP indicator. The subfigure on the left is the x-momentum, while on the right is the corresponding mesh. The base planes are the xy-plane.

As the second test problem, we consider a planar dam break problem. We take a spatial domain defined by $(x, y) \in [-1, 1] \times [-1, 1]$. The initial condition is

$$u(x, y, 0) = 0\,, \quad v(x, y, 0) = 0\,, \tag{6.78}$$

$$w(x, 0) = \begin{cases} 1 & \text{if} \quad x^2 + y^2 < 0.25\,, \\ 0.5 & \text{otherwise}\,. \end{cases} \tag{6.79}$$

The domain is discretised into 2048 triangular cells initially. We take a fixed time step $\Delta t = 0.002$ with 25 iterations. The maximum level of refinement or coarsening is 2. The NEP tolerance is $\text{NEP}_{\text{tol}} = 0.25 \max |\text{NEP}|$. Cells having absolute NEP larger than NEP_{tol} are candidates for refinement, and the rest are candidates for coarsening.

Representative simulation results are shown in Figure 6.11 and Figure 6.12. Similar to the previous simulation, we see that the grids are small around the shock and rarefaction in order to get accurate solutions, and large at the flat water surface. At this time ($t = 0.05$), the number of cells is 1968. In this simulation we use the flux function due to Kurganov et al. [36] for each flux of the conserved quantity and entropy evolutions to avoid positive overshoots of the NEP. In the following remark we mention a recommendation and research in progress about positive overshoots of the NEP in two dimensions.

Remark 6.6. For a two-dimensional problem, we can consider the flux passing an edge of a cell as a one-and-a-half dimensional flux. In this case, we do not recommend the use of the upwind flux technique for solving the passive transport component. Rather, the same flux function formulation should be used for each of mass, momentum, and passive transport equations. Through the numerical experiments, we see that if we use the upwinding technique for computing the passive transport flux on unstructured triangular grids, the positive overshoots could be very large and the NEP could be oscillatory between large positive and negative values. Again by some experiments, we see that: structured rectangular grids, rather than unstructured triangular grids, lead to smaller positive overshoots; and the Lax-Friedrichs flux, rather than the flux due to Kurganov et al. [36], leads to smaller positive overshoots.

To conclude this section, our formulation of the NEP in two dimensions can be implemented in adaptive methods successfully. It can detect smooth and nonsmooth regions. Furthermore, as a smoothness indicator it can initiate coarsening and refinement of the computational mesh in adaptive methods.

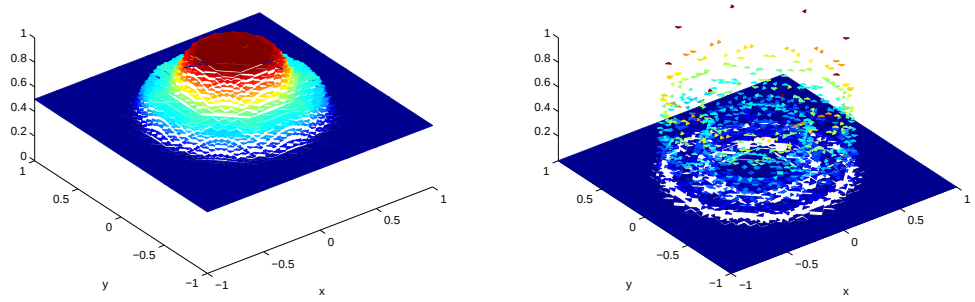

Figure 6.11: The stage and error indicator of the radial dam-break problem at $t = 0.05$ using the first order adaptive method with the NEP indicator. The subfigure on the left is water surface, while on the right is $-\text{NEP}/\max|\text{NEP}|$. The base planes are the xy-plane.

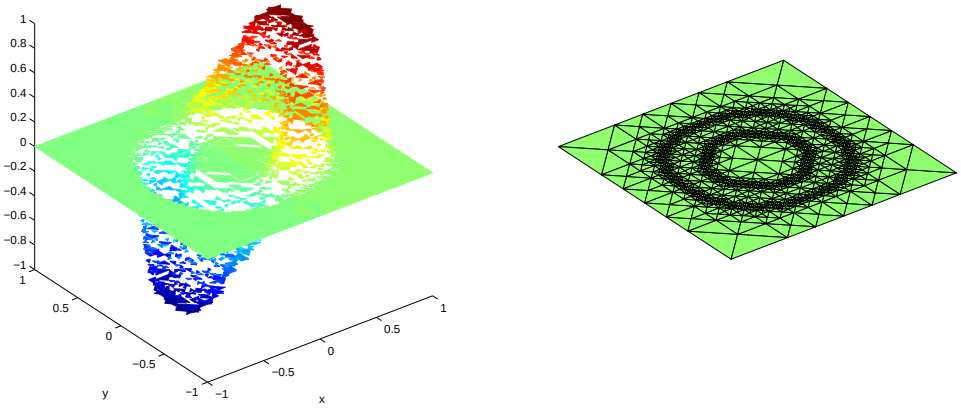

Figure 6.12: The x-momentum and mesh of the radial dam-break problem at $t = 0.05$ using the first order adaptive method with the NEP indicator. The subfigure on the left is x-momentum, while on the right is the corresponding mesh. The base planes are the xy-plane.

6.5 Concluding remarks

Numerical entropy production (NEP) as a smoothness indicator has been proposed for shallow water flows. We have also implemented the NEP as the refinement indicator in adaptive finite volume methods for one, one-and-a-half, and two dimensions. Overall, the NEP is successful as a smoothness or refinement indicator due to different orders of accuracy of the NEP in smooth and nonsmooth regions.

We note that if the solution is steepening up without a shock, then analytically the entropy production is zero. However, numerically the entropy production (the NEP) is nonzero, but very small. This is the reason why refinement can be performed even though there is not a shock. That is, if the tolerance is sufficiently smaller than the NEP, refinement can be performed even on a supposed smooth region. This is because numerically, we have jumps between cells. These jumps generate nonzero NEP even though the values of the NEP are very small.

From this chapter, we find that the performance of NEP is better than that of weak local residuals. However, weak local residuals as a smoothness indicator have an advantage in that they are cheaper to compute, based on their formulation. To complete our study, we shall discuss weak local residuals in more detail in the next chapter.

This page was intentionally left blank.

Chapter 7

Weak local residuals*

7.1 Introduction

As stated in Chapter 6, weak local residuals as smoothness indicators for conservation laws were originally proposed by Karni, Kurganov, and Petrova [32, 33]. In their work, weak local residuals were called weak local truncation errors, but in this thesis we follow the term "weak local residuals" used by Kurganov et al. [15, 35]. Based on the definition given in the next section, this term is more appropriate.

The theory supporting weak local residuals as smoothness indicators is so far available only for the scalar conservation law, but by numerical experiments, weak local residuals as smoothness indicators were seen to be also valid for systems of conservation laws [32, 33]. Note that a conservation law does not have any source term. The point of the theory is that the order of accuracy of weak local residuals in a rough region is lower than the order of accuracy in a smooth region [16, 32, 33]. This difference in the order of accuracy gives weak local residuals the ability to detect the smoothness of solutions.

In this chapter, we are interested in measuring the smoothness of solutions of the shallow water equations using weak local residuals. The nonhomogeneous shallow water equations form a system of balance laws, which is a system of conservation laws with an additional nonzero source term. Depending on whether we define the weak local residuals based on mass or momentum equations, we may or may not need to deal with the source term in order to compute the residuals. We shall see in the experiments that the available theory supporting weak local

*The results of this chapter are in preparation for two publication submissions.

residuals as smoothness indicators is also valid to a system of balance laws. A weak local residual can be implemented as a refinement indicator in an adaptive method, due to the ability of the residual to detect the smoothness of solutions.

The rest of this chapter is organised as follows. We derive weak local residual formulations for the scalar balance law in Section 7.2. Then in Section 7.3, we present a numerical technique for computing the weak local residuals of the shallow water equations. We implement weak local residuals as refinement indicators in adaptive methods in Section 7.4. Some concluding remarks are drawn in Section 7.5.

7.2 Weak local residuals of balance laws

Kurganov et al. [32, 33] formulated the weak local residuals of the scalar conservation law. In this section, we extend the work of Kurganov et al. [32, 33] to get the formulation of weak local residuals of balance laws. We limit our discussion to one dimension.

Consider the scalar balance law with an initial condition

$$\begin{cases} q_t + f(q)_x = s\,, & -\infty < x < \infty\,, \\ q(x,t) = q_0(x)\,, & t = 0\,. \end{cases} \tag{7.1}$$

Here x is a one-dimesional space variable, t is the time variable, q is the conserved quantity, f is the flux function, s is the source function and q_0 is an arbitrary function defined for an initial condition. The weak form of the initial value problem (7.1) is

$$\int_0^\infty \int_{-\infty}^\infty [q(x,t)T_t(x,t) + f(q(x,t))T_x(x,t) + s(x,t)T(x,t)]\,dx\,dt + \int_{-\infty}^\infty q_0(x)T(x,0)\,dx = 0, \tag{7.2}$$

where $T(x,t)$ is an arbitrary test function. A mathematical derivation of this weak form can be found in some textbooks, such as those written by Knobel [34] and Smoller [63].

We take uniform grids ($x_j := j\Delta x\,,\ t^n := n\Delta t$) and let q_j^n be approximate values of $q(x_j, t^n)$ computed by a conservative method. Similar to the notations of Karni and Kurganov [32], we denote by $q^\Delta(x,t)$ the corresponding piecewise constant approximation,

$$q^\Delta(x,t) := q_j^n \quad \text{if} \quad (x,t) \in [x_{j-1/2}, x_{j+1/2}] \times [t^{n-1/2}, t^{n+1/2}] \tag{7.3}$$

where $x_{j\pm1/2} := x_j \pm \Delta x/2$ and $t^{n\pm1/2} := t^n \pm \Delta t/2$. We construct a test function $T_j^n(x,t) := B_j(x)B^n(t)$, where $B_j(x)$ and $B^n(t)$ are quadratic B-splines centered at $x = x_j$ and $t = t^n$ with support of size $3\Delta x$ and $3\Delta t$. That is,

$$B_j(x) = \begin{cases} \frac{1}{2}\left(\frac{x-x_{j-3/2}}{\Delta x}\right)^2 & \text{if } x_{j-3/2} \le x \le x_{j-1/2}\,, \\ \frac{3}{4} - \left(\frac{x-x_j}{\Delta x}\right)^2 & \text{if } x_{j-1/2} \le x \le x_{j+1/2}\,, \\ \frac{1}{2}\left(\frac{x-x_{j+3/2}}{\Delta x}\right)^2 & \text{if } x_{j+1/2} \le x \le x_{j+3/2}\,, \\ 0 & \text{otherwise}\,, \end{cases} \tag{7.4}$$

and

$$B^n(t) = \begin{cases} \frac{1}{2}\left(\frac{t-t^{n-3/2}}{\Delta t}\right)^2 & \text{if } t^{n-3/2} \le t \le t^{n-1/2}\,, \\ \frac{3}{4} - \left(\frac{t-t^n}{\Delta t}\right)^2 & \text{if } t^{n-1/2} \le t \le t^{n+1/2}\,, \\ \frac{1}{2}\left(\frac{t-t^{n+3/2}}{\Delta t}\right)^2 & \text{if } t^{n+1/2} \le t \le t^{n+3/2}\,, \\ 0 & \text{otherwise}\,. \end{cases} \tag{7.5}$$

Then substituting the test function $T_j^n(x,t)$ into (7.2) leads to a weak form of the local residual [32, 33]

$$\begin{aligned} E_j^n \;=\; & -\int_{t^{n-3/2}}^{t^{n+3/2}} \int_{x_{j-3/2}}^{x_{j+3/2}} \Big\{ q^\Delta(x,t)\left[T_j^n(x,t)\right]_t \\ & + f(q^\Delta(x,t))\left[T_j^n(x,t)\right]_x + s^\Delta(x,t)T_j^n(x,t) \Big\}\, dx\, dt, \end{aligned} \tag{7.6}$$

for the balance law. After a straightforward computation, the weak local residual (7.6) can then be expressed as

$$\begin{aligned} E_j^n \;=\; & \frac{\Delta x}{12}\left[q_{j+1}^{n+1} - q_{j+1}^{n-1} + 4\left(q_j^{n+1} - q_j^{n-1}\right) + q_{j-1}^{n+1} - q_{j-1}^{n-1}\right] \\ & + \frac{\Delta t}{12}\left[f(q_{j+1}^{n+1}) - f(q_{j-1}^{n+1}) + 4\left(f(q_{j+1}^n) - f(q_{j-1}^n)\right)\right. \\ & \qquad \left. + f(q_{j+1}^{n-1}) - f(q_{j-1}^{n-1})\right] \\ & - \frac{\Delta x \Delta t}{36}\left[s_{j-1}^{n-1} + 4s_{j-1}^n + s_{j-1}^{n+1} + 4\left(s_j^{n-1} + 4s_j^n + s_j^{n+1}\right)\right. \\ & \qquad \left. + s_{j+1}^{n-1} + 4s_{j+1}^n + s_{j+1}^{n+1}\right]. \end{aligned} \tag{7.7}$$

This taking quadratic B-splines in constructing the test function adapts from the work of Karni, Kurganov, and Petrova [33] on conservation laws. We denote by KKP (Karni-Kurganov-Petrova) indicator the weak local residual (7.7).

Rather than using quadratic B-splines, we choose the localised linear B-splines as the test functions $T_{j+1/2}^{n-1/2}(x,t) := B_{j+1/2}(x)B^{n-1/2}(t)$, where $B_{j+1/2}(x)$ and

$B^{n-1/2}(t)$ are centered at $x = x_{j+1/2}$ and $t = t^{n-1/2}$ with support of size $2\Delta x$ and $2\Delta t$. That is,

$$B_{j+1/2}(x) = \begin{cases} \frac{x - x_{j-1/2}}{\Delta x} & \text{if } x_{j-1/2} \le x \le x_{j+1/2}\,, \\ \frac{x_{j+3/2} - x}{\Delta x} & \text{if } x_{j+1/2} \le x \le x_{j+3/2}\,, \\ 0 & \text{otherwise}\,, \end{cases} \tag{7.8}$$

and

$$B^{n-1/2}(t) = \begin{cases} \frac{t - t^{n-3/2}}{\Delta t} & \text{if } t^{n-3/2} \le t \le t^{n-1/2}\,, \\ \frac{t^{n+1/2} - t}{\Delta t} & \text{if } t^{n-1/2} \le t \le t^{n+1/2}\,, \\ 0 & \text{otherwise}\,. \end{cases} \tag{7.9}$$

This results in a less expensive computation of the weak local residual

$$\begin{aligned} E^{n-1/2}_{j+1/2} &= -\int_{t^{n-3/2}}^{t^{n+1/2}} \int_{x_{j-1/2}}^{x_{j+3/2}} \Big[q^{\Delta}(x,t) \left[T^{n-1/2}_{j+1/2} \right]_t + f(q^{\Delta}(x,t)) \left[T^{n-1/2}_{j+1/2} \right]_x \\ &\quad + s^{\Delta}(x,t) T^{n-1/2}_{j+1/2} \Big]\, dx\, dt, \end{aligned} \tag{7.10}$$

which can be expressed after a straightforward computation as

$$\begin{aligned} E^{n-1/2}_{j+1/2} &= \frac{\Delta x}{2} \left[q^n_j - q^{n-1}_j + q^n_{j+1} - q^{n-1}_{j+1} \right] \\ &\quad + \frac{\Delta t}{2} \left[f\left(q^{n-1}_{j+1}\right) - f\left(q^{n-1}_j\right) + f\left(q^n_{j+1}\right) - f\left(q^n_j\right) \right] \\ &\quad - \frac{\Delta x \Delta t}{4} \left[s^{n-1}_j + s^n_j + s^{n-1}_{j+1} + s^n_{j+1} \right]. \end{aligned} \tag{7.11}$$

This taking linear B-splines in constructing the test function adapts from the work of Constantin and Kurganov [16] on conservation laws. We denote by CK (Constantin-Kurganov) indicator the weak local residual (7.11).

7.3 Weak local residuals of shallow water equations

Following the presentation given in the previous section, we provide a technique to compute weak local residuals of the one-dimensional shallow water equations in this section.

Recall the one-dimensional shallow water equations

$$h_t + (hu)_x = 0\,, \tag{7.12}$$

$$(hu)_t + \left(hu^2 + \tfrac{1}{2}gh^2\right)_x = -ghz_x\,. \tag{7.13}$$

Here, x represents the coordinate in one-dimensional space, t represents the time variable, $u = u(x,t)$ denotes the water velocity, $h = h(x,t)$ denotes the water height, $z = z(x)$ is the topography, and g is the acceleration due to gravity.

The nonhomogeneous shallow water equations (7.12)–(7.13) are a system of balance laws. The source term occurs only in (7.13). Computing weak local residuals of (7.12) is straightforward based on formulation (7.7) or (7.11). This is because no well-balancing is needed, as there is not a source term in (7.12).

However, implementation of KKP given by (7.7) and/or CK given by (7.11) naïvely as smoothness indicators to (7.13) may result in spurious oscillations of the indicator values. We show a representative of this problem in Subsection 7.3.3. The problem is caused by the non-well-balanced computation of KKP and CK indicators due to the source term involved. To make the indicators work properly, we need to make the computation of the indicators well-balanced.

In the next two subsections, we focus on well-balancing the weak local residual of the nonhomogeneous momentum equation. We limit our discussion to the well-balanced technique for the steady state of a lake at rest.

7.3.1 Well-balancing the weak local residual

We propose a well-balanced technique for computing weak local residuals KKP (7.7) and CK (7.11) relating to the nonhomogeneous momentum equation (7.13).

Well-balancing KKP indicator

Consider the weak local residual KKP (7.7). For steady state of a lake at rest, the weak local residual (7.7) is simplified to

$$\begin{aligned} E_j^n \;=\; & \frac{\Delta t}{12}\left[f(q_{j+1}^{n+1}) - f(q_{j-1}^{n+1})\right] - \frac{\Delta x \Delta t}{36}\left[s_{j+1}^{n+1} + 4s_j^{n+1} + s_{j-1}^{n+1}\right] \\ & + \frac{\Delta t}{3}\left[f(q_{j+1}^{n}) - f(q_{j-1}^{n})\right] - \frac{\Delta x \Delta t}{9}\left[s_{j+1}^{n} + 4s_j^{n} + s_{j-1}^{n}\right] \\ & + \frac{\Delta t}{12}\left[f(q_{j+1}^{n-1}) - f(q_{j-1}^{n-1})\right] - \frac{\Delta x \Delta t}{36}\left[s_{j+1}^{n-1} + 4s_j^{n-1} + s_{j-1}^{n-1}\right], \end{aligned} \tag{7.14}$$

where $f(q_a^b) = \frac{1}{2}g(h_a^b)^2$ for arbitrary indices a and b. The well-balancing is done for computations at each level of time step, that is, we must have

$$\frac{\Delta t}{12}\left[f(q_{j+1}^{n+1}) - f(q_{j-1}^{n+1})\right] = \frac{\Delta x \Delta t}{36}\left[s_{j+1}^{n+1} + 4s_j^{n+1} + s_{j-1}^{n+1}\right], \tag{7.15}$$

$$\frac{\Delta t}{3}\left[f(q^n_{j+1}) - f(q^n_{j-1})\right] = \frac{\Delta x \Delta t}{9}\left[s^n_{j+1} + 4s^n_j + s^n_{j-1}\right], \tag{7.16}$$

$$\frac{\Delta t}{12}\left[f(q^{n-1}_{j+1}) - f(q^{n-1}_{j-1})\right] = \frac{\Delta x \Delta t}{36}\left[s^{n-1}_{j+1} + 4s^{n-1}_j + s^{n-1}_{j-1}\right]. \tag{7.17}$$

Equations (7.15), (7.16), and (7.17) are enforcements based on the first, second, and third two terms of the right hand side of (7.14).

In particular, consider (7.16). The fluxes involved in (7.16) are defined only at the $(j-1)$th and $(j+1)$th cells, but the numerical sources are defined at the $(j-1)$th, jth, and $(j+1)$th cells. For well-balancing (7.16), we need that the source term discretisations and the fluxes involve the same cells. With this reason, we consider two numerical strategies as follow. First, we take $s^n_j = \frac{1}{2}(s^n_{j+1} + s^n_{j-1})$ Second, the formulations of s^n_{j+1} and s^n_{j-1} are defined based on the same value of the topography gradient z_x involving only the $(j-1)$th and $(j+1)$th cells as

$$(z_x)^n_{j+1} = (z_x)^n_{j-1} := \frac{z^n_{j+1} - z^n_{j-1}}{2\Delta x}. \tag{7.18}$$

We then obtain the numerical discretisations for s^n_{j+1}, s^n_{j-1}, and s^n_j respectively as follows:

$$s^n_{j+1} = -gh^n_{j+1}\frac{z^n_{j+1} - z^n_{j-1}}{2\Delta x}, \tag{7.19}$$

$$s^n_{j-1} = -gh^n_{j-1}\frac{z^n_{j+1} - z^n_{j-1}}{2\Delta x}, \tag{7.20}$$

$$s^n_j = \frac{1}{2}(s^n_{j+1} + s^n_{j-1}) = -g\frac{h^n_{j+1} + h^n_{j-1}}{2}\frac{z^n_{j+1} - z^n_{j-1}}{2\Delta x}. \tag{7.21}$$

Noting that $h^n_{j+1} - h^n_{j-1} = z^n_{j-1} - z^n_{j+1}$ for steady state of a lake at rest, we find by a straightforward computation that (7.16) is indeed achieved for the source discretisations (7.19), (7.20), and (7.21). Furthermore, the well-balanced techniques for (7.15) and (7.17) are similar to that for (7.16). A complete source discretisation for the weak local residual KKP (7.7) is shown in the first and second columns of Table 7.1.

Well-balancing CK indicator

Now, consider the weak local residual CK (7.11). For the steady state of a lake at rest, the weak local residual (7.11) is simplified to

$$\begin{aligned} E^n_j &= \frac{\Delta t}{2}\left[f(q^n_{j+1}) - f(q^n_j)\right] - \frac{\Delta x \Delta t}{4}\left[s^n_{j+1} + s^n_j\right] \\ &\quad + \frac{\Delta t}{2}\left[f(q^{n-1}_{j+1}) - f(q^{n-1}_j)\right] - \frac{\Delta x \Delta t}{4}\left[s^{n-1}_{j+1} + s^{n-1}_j\right]. \end{aligned} \tag{7.22}$$

Table 7.1: Discrete values for the source in KKP and CK.

Terms in KKP	Discrete values	Terms in CK	Discrete values
s_{j-1}^{n-1}	$-g\,h_{j-1}^{n-1}\,\frac{z_{j+1}^{n-1}-z_{j-1}^{n-1}}{2\Delta x}$	s_j^{n-1}	$-g\,h_j^{n-1}\,\frac{z_{j+1}^{n-1}-z_j^{n-1}}{\Delta x}$
s_{j-1}^{n}	$-g\,h_{j-1}^{n}\,\frac{z_{j+1}^{n}-z_{j-1}^{n}}{2\Delta x}$	s_j^{n}	$-g\,h_j^{n}\,\frac{z_{j+1}^{n}-z_j^{n}}{\Delta x}$
s_{j-1}^{n+1}	$-g\,h_{j-1}^{n+1}\,\frac{z_{j+1}^{n+1}-z_{j-1}^{n+1}}{2\Delta x}$	s_{j+1}^{n-1}	$-g\,h_{j+1}^{n-1}\,\frac{z_{j+1}^{n-1}-z_j^{n-1}}{\Delta x}$
s_j^{n-1}	$-g\,\frac{h_{j+1}^{n-1}+h_{j-1}^{n-1}}{2}\,\frac{z_{j+1}^{n-1}-z_{j-1}^{n-1}}{2\Delta x}$	s_{j+1}^{n}	$-g\,h_{j+1}^{n}\,\frac{z_{j+1}^{n}-z_j^{n}}{\Delta x}$
s_j^{n}	$-g\,\frac{h_{j+1}^{n}+h_{j-1}^{n}}{2}\,\frac{z_{j+1}^{n}-z_{j-1}^{n}}{2\Delta x}$		
s_j^{n+1}	$-g\,\frac{h_{j+1}^{n+1}+h_{j-1}^{n+1}}{2}\,\frac{z_{j+1}^{n+1}-z_{j-1}^{n+1}}{2\Delta x}$		
s_{j+1}^{n-1}	$-g\,h_{j+1}^{n-1}\,\frac{z_{j+1}^{n-1}-z_{j-1}^{n-1}}{2\Delta x}$		
s_{j+1}^{n}	$-g\,h_{j+1}^{n}\,\frac{z_{j+1}^{n}-z_{j-1}^{n}}{2\Delta x}$		
s_{j+1}^{n+1}	$-g\,h_{j+1}^{n+1}\,\frac{z_{j+1}^{n+1}-z_{j-1}^{n+1}}{2\Delta x}$		

For a well-balanced computation, we must have

$$\frac{\Delta t}{2}\left[f(q_{j+1}^{n})-f(q_j^{n})\right]=\frac{\Delta x\Delta t}{4}\left[s_{j+1}^{n}+s_j^{n}\right], \tag{7.23}$$

$$\frac{\Delta t}{2}\left[f(q_{j+1}^{n-1})-f(q_j^{n-1})\right]=\frac{\Delta x\Delta t}{4}\left[s_{j+1}^{n-1}+s_j^{n-1}\right]. \tag{7.24}$$

In particular, consider (7.23). The fluxes on the right hand side of (7.23) and the numerical sources on the left hand side involve the same cells, which are the jth and $(j+1)$th cells. The well-balancing of (7.23) shall be undertaken based on these two cells. We formulate s_j^n and s_{j+1}^n based on the same value of the topography gradient z_x involving only the jth and $(j+1)$th cells as

$$(z_x)_{j+1}^{n}=(z_x)_j^{n}:=\frac{z_{j+1}^{n}-z_j^{n}}{\Delta x}. \tag{7.25}$$

We then obtain the numerical discretisations for s^n_{j+1} and s^n_j respectively as follows:

$$s^n_{j+1} = -gh^n_{j+1}\frac{z^n_{j+1} - z^n_j}{\Delta x}\,, \tag{7.26}$$

$$s^n_j = -gh^n_j\frac{z^n_{j+1} - z^n_j}{\Delta x}\,. \tag{7.27}$$

A straightforward computation confirms that (7.23) is achieved for the source discretisations (7.26) and (7.27). Furthermore, the well-balanced techniques for (7.24) is similar to that for (7.23). A complete source discretisation for the weak local residual CK (7.11) is shown in the third and fourth columns of Table 7.1.

For our reference, the source term discretisation technique described above adapts from the technique for developing numerical schemes originally proposed by Bermudez and Vazquez [4]. This technique was also used by Audusse et al. [2] and Noelle et al. [53] to develope well-balanced numerical schemes.

7.3.2 Wet/dry interface treatment for weak local residuals

The well-balanced technique describe in Subsection 7.3.1 is valid for all-wet regions, that is, the $(j-1)$th, jth, and $(j+1)$th cells are wet. A numerical treatment at a wet/dry interface is needed. We describe the wet/dry treatment in this subsection. We omit the description of a dry/wet treatment, as it is similar to the treatment of a wet/dry interface.

We solve the shallow water equations using the finite volume method described in our previous work [45] in Chapter 2. We implement the discretisation proposed by Audusse et al. [2]. Quantities are reconstructed based on stage $w := h + z$, height h, and velocity u. We implement the wet/dry interface reconstruction, also proposed by Audusse et al. [2]. The wet/dry interface reconstruction does special treatment on the bed topography z if negative water height occurs, so that the water height h remains nonnegative (see [2, 45] for more details). A second order method with the minmod limiter is used.

Since KKP indicator of the jth cell involves three cells, namely the $(j-1)$th, jth, and $(j+1)$th cells, there are two cases of the wet/dry interface for the KKP indicator: (a) wet-dry-dry, that is, wet for the $(j-1)$th cell, dry for the jth cell, dry for the $(j+1)$th cell; and (b) wet-wet-dry, that is, wet for the $(j-1)$th cell, wet for the jth cell, dry for the $(j+1)$th cell. These two cases are illustrated in Figure 7.1. In the computation of KKP indicator for these cases, the value of z^n_{j+1}

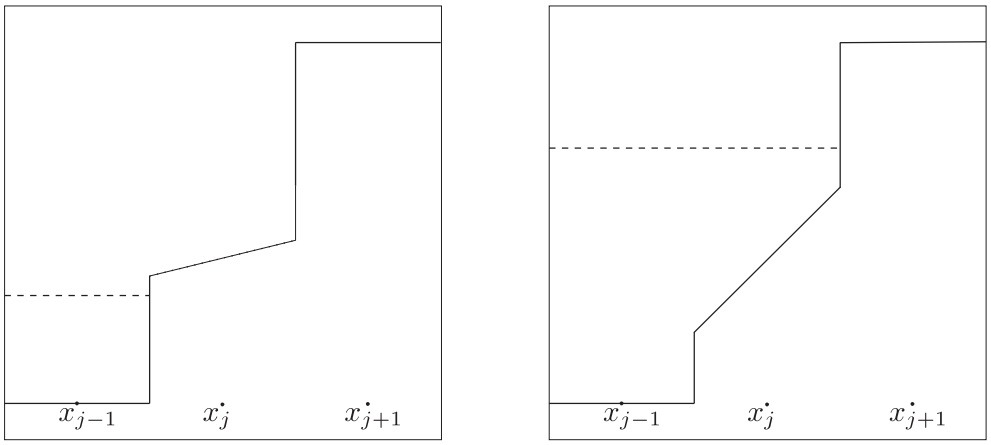

(a) (b)

Figure 7.1: Two cases of the wet/dry interface for the KKP indicator: (a) The wet-dry-dry case. (b) The wet-wet-dry case.

is replaced by w_{j-1}^n. This ensures that the indicator computation at the wet/dry interface remains well-balanced. Other special cases, namely wet-dry-wet and dry-wet-dry, are considered as having zero indicator values.

The treatment of a wet/dry interface computation of the CK indicator is analogous. Since the CK indicator considers only two cells, namely jth and $(j+1)$th cells for computing the weak local residual, there is only one case of a wet/dry interface. That is, the jth cell is wet but the $(j+1)$th cell is dry. In this case the value of z_{j+1}^n is replaced by w_j^n, so that the indicator computation at the wet/dry interface remains well-balanced.

7.3.3 Numerical tests

We test the performance of weak local residuals. We use the second order well-balanced finite volume method [45]. Quantities are measured in SI units. The numerical tests in this subsection are carried out using the Python 2.7 programming language. Three tests are considered: (a) a well-balanced test relating to the steady state of a lake at rest, (b) an unsteady dam break test, and (c) a steady state test with moving water involving a stationary shock.

(a) Well-balanced test

As the first test, we shall show by numerical experiment that our proposed well-balanced technique for computing weak local residuals of the momentum equation (7.13) works properly. Recall a lake at rest with a discontinuous island in the middle of the lake, given in Figure 2.4. In the present computation, the spatial domain is discretised into 800 cells.

At time $t = 2$, four indicators namely CKh, CKuh, KKPh, and KKPuh are depicted in Figure 7.2. Indicators CKh and CKuh are the weak local residuals of the mass and momentum equations based on (7.11), while KKPh and KKPuh are the weak local residuals of the mass and momentum equations based on (7.7). All indicators attain the correct weak local residuals of the steady state of a lake at rest up to the order of 10^{-15} (machine precision).

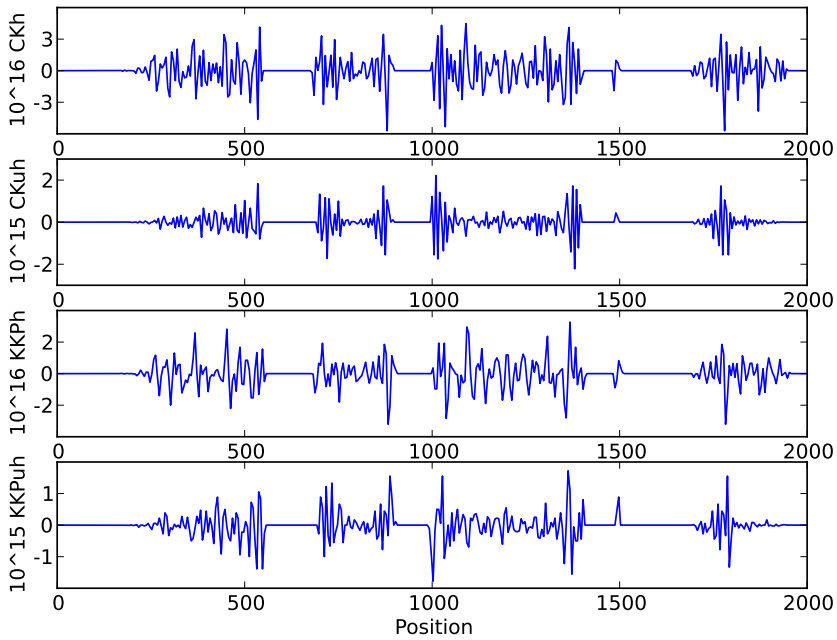

Figure 7.2: The weak local residuals at time $t = 2$. The notation 10^16 CKh means 10^{16} times CKh; the meaning of 10^15 CKuh, 10^16 KKPh, 10^15 KKPuh are inferred in the same way.

In contrast, non-well-balanced computations of weak local residuals could lead to incorrect behaviour of the residuals, as unphysical oscillations may occur. Figure 7.3 shows this incorrect behaviour of weak local residuals. In this Figure 7.3,

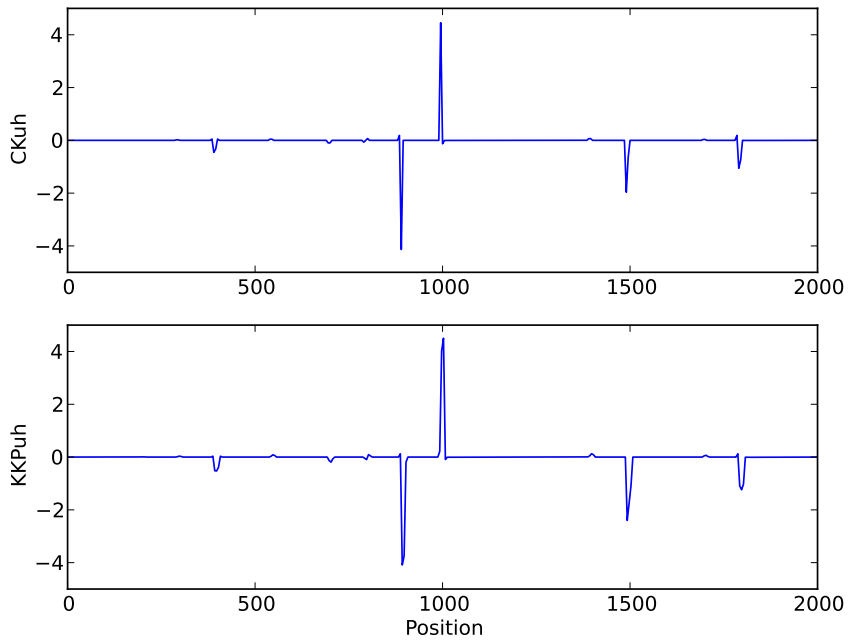

Figure 7.3: Unphysical weak local residuals at time $t = 2$. Here CKuh and KKPuh are computed naïvely using local cell quantity values based on finite volume quantity reconstructions. Both CKuh and KKPuh are shown without scaling.

CKuh and KKPuh are shown without scaling and computed naïvely using local cell quantity values found from finite volume quantity reconstructions. In this case, CKuh and KKPuh have large values of indicators at some points, which should actually be zero.

(b) Dam break with a dry area and moving shock

As the second test, we consider a dam break with a dry area and moving shock as follows.

Consider the collapse of a reservoir on a horizontal topography [47]

$$z(x) = 0\,, \quad 0 < x < 2000\,, \tag{7.28}$$

and an initial condition

$$u(x,0) = 0\,, \quad w(x,0) = \begin{cases} 0 & \text{if} \quad 0 < x < 500\,, \\ 10 & \text{if} \quad 500 < x < 1500\,, \\ 5 & \text{if} \quad 1500 < x < 2000\,. \end{cases} \tag{7.29}$$

The simulation is done to illustrate the motion of the water at any point x in the domain and at any time $t > 0$ with respect to the initial condition (7.29). With the condition (7.29), we have two dam walls (at $x = 500$ and $x = 1500$) given initially. In the computation, the spatial domain is discretised into 800 cells.

The simulation results at time $t = 20$ are depicted in Figures 7.4 and 7.5. Figure 7.4 shows the stage and the corresponding momentum value. The weak local residuals CKh, CKuh, KKPh, and KKPuh are exhibited in Figure 7.5. A moving shock occurs in this simulation. The moving shock is clearly detected by large values of the weak local residuals.

(c) Steady flow with a stationary shock

As the third test, we consider a steady flow with moving water as follows.

Consider a channel of length 25 with topography (having a parabolic bump) [47]

$$z(x) = \begin{cases} 0.2 - 0.05\,(x-10)^2 & \text{if} \quad 8 \le x \le 12\,, \\ 0 & \text{otherwise}\,, \end{cases} \tag{7.30}$$

and an initial condition

$$u(x,0) = 0\,, \quad w(x,0) = 0.33 \tag{7.31}$$

together with the Dirichlet boundary conditions

$$[w, hu, z, h, u] = [0.42, 0.18, 0.0, 0.42, 0.18/0.42] \quad \text{at} \quad x = 0^-\,, \tag{7.32}$$

$$[w, hu, z, h, u] = [0.33, 0.18, 0.0, 0.33, 0.18/0.33] \quad \text{at} \quad x = 25^+\,. \tag{7.33}$$

In the computation, the spatial domain is discretised into 400 cells.

The simulation results at time $t = 100$ are depicted in Figures 7.6 and 7.7. Figures 7.6 shows the stage and the corresponding momentum value. The weak local residuals CKh, CKuh, KKPh, and KKPuh are exhibited in Figure 7.7. A stationary shock is produced in this simulation. The stationary shock is detected by large values of weak local residuals.

To conclude this section, the indicator CKh, that is, the weak local residual of the mass equation based on (7.11) performs better than the other weak local residuals. This indicator is less oscillatory on smooth solutions. In the next section, we shall implement the CK indicator in adaptive methods.

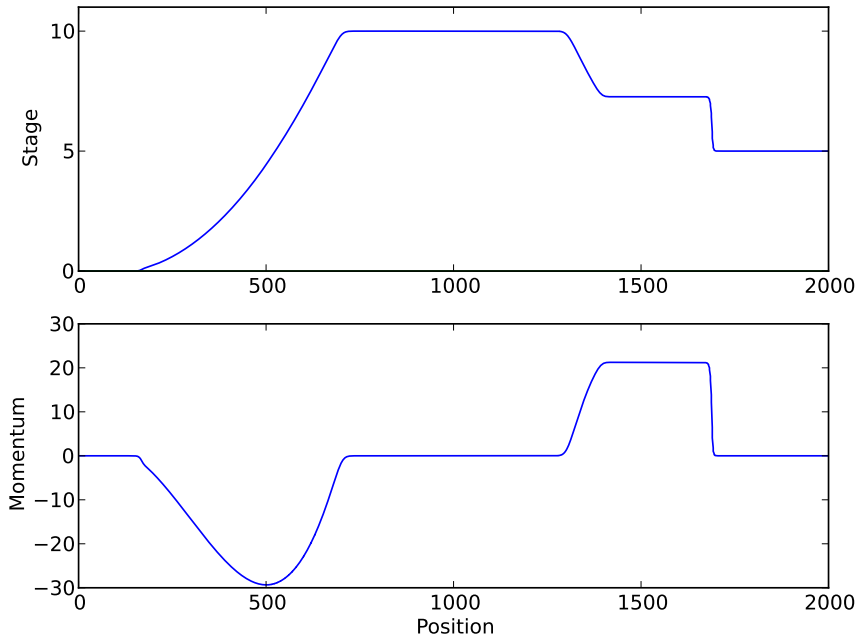

Figure 7.4: The dam break stage and momentum at time $t = 20$.

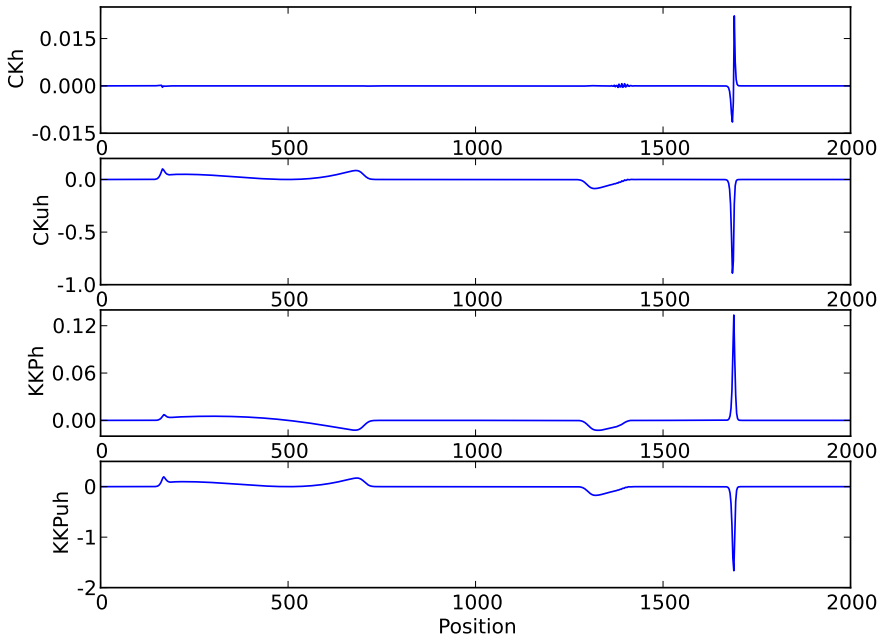

Figure 7.5: The dam break weak local residuals at time $t = 20$.

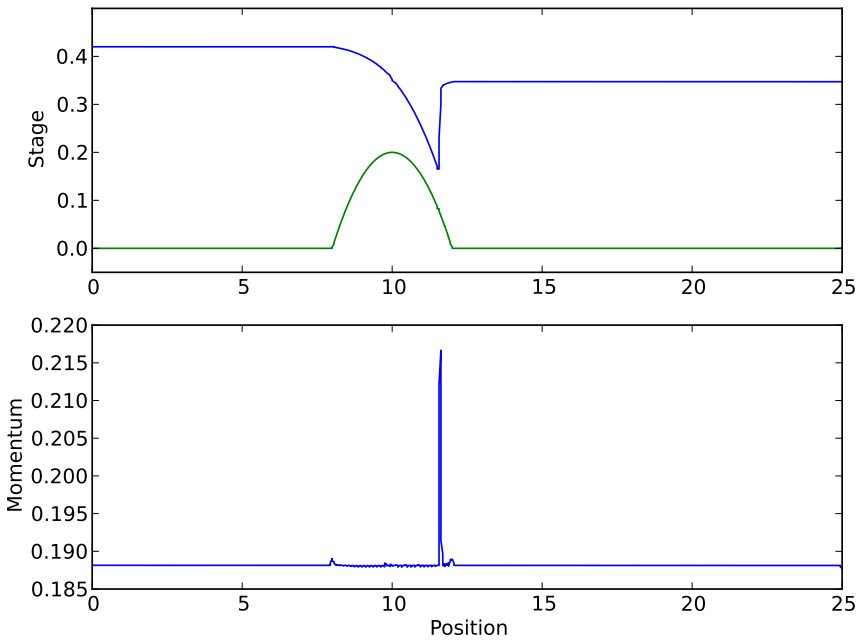

Figure 7.6: The stage and momentum of steady flow over a parabolic obstruction at $t = 100$.

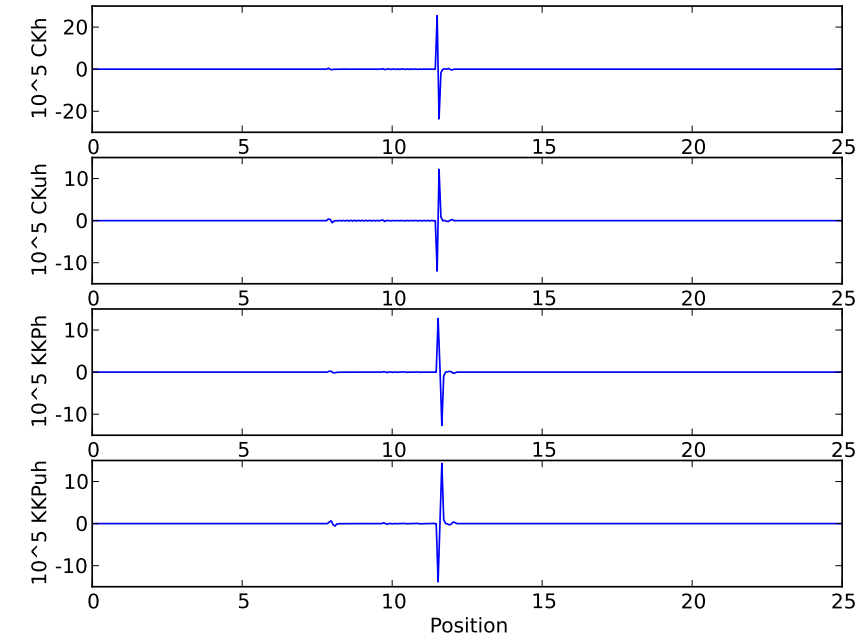

Figure 7.7: The weak local residuals of steady flow over a parabolic obstruction at $t = 100$.

7.4 Weak local residuals in adaptive methods

In this section, we shall present simple formulations of weak local residuals (WLR) for one-, one-and-a-half-, and two-dimensional shallow water equations. We shall also present numerical results relating to the implementation of weak local residuals in adaptive methods.

First, we consider the shallow water equations in one dimension. In the computation of the CK indicator, one may choose to compute it with respect to either the mass equation, momentum equation or a combination between the mass and momentum equations. However, for simplicity we choose to compute the CK indicator with respect to the mass equation as

$$\begin{aligned} E_{i+1/2}^{h,n-1/2} &= (1/2)\left\{\Delta x\left[h_i^n - h_i^{n-1} + h_{i+1}^n - h_{i+1}^{n-1}\right]\right. \\ &\quad \left.+\Delta t\left[h_{i+1}^{n-1}u_{i+1}^{n-1} - h_i^{n-1}u_i^{n-1} + h_{i+1}^n u_{i+1}^n - h_i^n u_i^n\right]\right\} \end{aligned} \tag{7.34}$$

defined at time $t = t^{n-1/2}$ and position $x = x_{i+1/2}$, where the superscript h in $E_{i+1/2}^{h,n-1/2}$ represents the mass quantity (height). Based on the findings given in the previous section, weak local residuals with respect to the mass and momentum equations have approximately the same behaviour. We conjecture that both Δx and Δt in (7.34) can be taken as constants over the whole discretised spatial domain. In particular, for one-dimensional problems we define $\Delta x := \min\{\Delta x_i\}$ as the minimum cell width over the whole discretised spatial domain to be substituted in (7.34) and Δt is the time step, which varies from one time step to another.

Formulation (7.34) is defined at each vertex. To define the CK indicator at the centroids of each cell, we choose one of two available indicators at its cell vertices having the largest magnitude and divide it by the local cell width. That is, the CK indicator at the centroid of the ith cell is

$$E_i^{h,n-1/2} = \frac{1}{\Delta x_i} \times \begin{cases} E_{i-1/2}^{h,n-1/2} & \text{if} \quad \left|E_{i-1/2}^{h,n-1/2}\right| \geq \left|E_{i+1/2}^{h,n-1/2}\right|, \\ E_{i+1/2}^{h,n-1/2} & \text{otherwise}. \end{cases} \tag{7.35}$$

When the numerical method has a formal order r, the order of $\left|E_i^{h,n-1/2}\right|$ is $O(1)$ near discontinuities and $O\left(\Delta^{\min\{3,r+1\}}\right)$ in smooth regions [16]. The order difference between discontinuous and smooth regions makes $\left|E_i^{h,n-1/2}\right|$ able to detect the smoothness of the numerical solution.

Second, we consider the shallow water equations in one-and-a-half dimensions. An extended application of the CK indicator for one-and-a-half-dimensional problems needs special treatment. The one-and-a-half-dimensional shallow water equations model one-dimensional shallow water flows involving a transverse or shear velocity. It can also be considered as a one-dimensional shallow water flow involving a passive tracer. Recall the one-and-a-half-dimensional shallow water equations

$$h_t + (hu)_x = 0\,, \tag{7.36}$$

$$(hu)_t + \left(hu^2 + \frac{1}{2}gh^2\right)_x = -ghz_x\,, \tag{7.37}$$

$$(hv)_t + (huv)_x = 0\,. \tag{7.38}$$

The variables are the same as the one-dimensional model, except for an additional variable v. Here $v := v(x)$ denotes the transverse velocity, that is, the horizontal velocity orthogonal to the x-axis. For the passive tracer model, $v(x)$ is the concentration of the passive tracer.

The concentration $v(x)$ of the passive tracer does not influence the fluid dynamics. Computing WLR based on the mass or momentum equation or a combination of both equations will not detect the smoothness of the tracer solution. For the one-and-a-half dimensional model, the variable $v(x)$ must be incorporated in the computation of WLR, so that WLR is also able to detect the smoothness of the tracer solution. We propose to implement a combination of WLR with respect to the mass and passive transport equations. Using these two equations, we do not need to deal with a source term. One may alternatively consider using a combination of either momentum and passive transport equations or mass, momentum and transport equations. These alternatives need to deal with the source term and the well-balanced WLR should be implemented.

In particular, we compute the WLR of the mass equation denoted by $E_{i+1/2}^{h,n-1/2}$ and of the passive transport equation denoted by $E_{i+1/2}^{hv,n-1/2}$ at the vertices. Here $E_{i+1/2}^{h,n-1/2}$ is given by (7.34). In addition, $E_{i+1/2}^{hv,n-1/2}$ is given by

$$\begin{aligned} E_{i+1/2}^{hv,n-1/2} = (1/2)\,\big\{&\Delta x\left[(hv)_i^n - (hv)_i^{n-1} + (hv)_{i+1}^n - (hv)_{i+1}^{n-1}\right] \\ &+ \Delta t\left[(hv)_{i+1}^{n-1}u_{i+1}^{n-1} - (hv)_i^{n-1}u_i^{n-1} + (hv)_{i+1}^n u_{i+1}^n - (hv)_i^n u_i^n\right]\big\}\,, \end{aligned} \tag{7.39}$$

defined at time $t = t^{n-1/2}$ and position $x = x_{i+1/2}$, where the superscript hv in the notation $E_{i+1/2}^{hv,n-1/2}$ represents the passively transported quantity.

To define the CK indicator at the centroids of each cell, we choose one of four available indicators at its cell vertices having the largest magnitude and divide it by the local cell width. Let

$$M_i = \max\left\{\left|E_{i-1/2}^{h,n-1/2}\right|, \left|E_{i+1/2}^{h,n-1/2}\right|, \left|E_{i-1/2}^{hv,n-1/2}\right|, \left|E_{i+1/2}^{hv,n-1/2}\right|\right\}. \tag{7.40}$$

Then the CK indicator at the centroid of the ith cell is

$$E_i^{h,hv,n-1/2} = \frac{1}{\Delta x_i} \times \begin{cases} E_{i-1/2}^{h,n-1/2} & \text{if} \quad M_i = \left|E_{i-1/2}^{h,n-1/2}\right|, \\ E_{i+1/2}^{h,n-1/2} & \text{if} \quad M_i = \left|E_{i+1/2}^{h,n-1/2}\right|, \\ E_{i-1/2}^{hv,n-1/2} & \text{if} \quad M_i = \left|E_{i-1/2}^{hv,n-1/2}\right|, \\ E_{i+1/2}^{hv,n-1/2} & \text{otherwise}. \end{cases} \tag{7.41}$$

Finally, we consider the shallow water equations in two dimensions. An extended application of the CK indicator for two-dimensional problems is done as follows. Recall the two-dimensional shallow water equations

$$h_t + (hu)_x + (hv)_y = 0\,, \tag{7.42}$$

$$(hu)_t + \left(hu^2 + \frac{1}{2}gh^2\right)_x + (huv)_y = -ghz_x\,, \tag{7.43}$$

$$(hv)_t + (huv)_x + \left(hv^2 + \frac{1}{2}gh^2\right)_y = -ghz_y\,. \tag{7.44}$$

Here, (x, y) represents the coordinate in two-dimensional space, t represents the time variable, $u = u(x, y, t)$ denotes the fluid velocity along the x-axis, $v = v(x, y, t)$ denotes the fluid velocity along the y-axis, $h = h(x, y, t)$ denotes the fluid height, $z = z(x, y)$ is the bed elevation (topography), and g is the acceleration due to gravity. To solve the two-dimensional shallow water equations numerically, we discretise the spatial domain into polygonal cells. In the computation of the CK indicator, we can use the one-dimensional formulation (7.34) locally to define the CK indicator at the middle point of an edge. We have conjectured that both Δx and Δt in (7.34) can be taken as constants over the whole discretised spatial domain for one-dimensional problems. In computing the CK indicator for two-dimensional problems, we take $\Delta x = \Delta t$ over the whole discretised spatial domain and substitute into in (7.34), where Δt is the time step used in the finite volume method evolution. The values of Δt may vary from one time step to another depending on the CFL number, wave propagation velocity, and fluid velocity.

Then the CK indicator at the centroid of a cell is defined by one value of the available indicator values at its edges having the largest magnitude.

Having served the formulations of weak local residuals, we shall test the performance of weak local residuals in the adaptive mesh finite volume method. We use the first order well-balanced finite volume method [45]. Quantities are measured in SI units. The numerical flux due to Kurganov, Noelle, and Petrova [36] is used. Four tests are considered, namely: a one-dimensional flow with topography, a one-dimensional dam break with passive tracer, a planar dam break , and a radial dam break. Note that these tests are the same as some of the tests used in Chapter 6. Python 2.7 is used for programming the first two tests, and MATLAB is used for the later two tests.

7.4.1 A one-dimensional flow with topography

In the following simulation we emphasize that our adaptive method gives an accurate solution around the shock.

Recall the one-dimensional problem with topography considered by Felcman and Kadrnka [23]. Consider a channel of length 25 with topography

$$z(x) = \begin{cases} 0.2 - 0.05\,(x-10)^2 & \text{if} \quad 8 \le x \le 12\,, \\ 0 & \text{otherwise}\,, \end{cases} \tag{7.45}$$

and an initial condition

$$u(x,0) = 0\,, \quad w(x,0) = 0.66 \tag{7.46}$$

together with the Dirichlet boundary conditions

$$h(25,t) = 0.66\,, \quad hu(0,t) = hu(25,t) = 1.53\,. \tag{7.47}$$

The spatial domain is discretised into 100 cells initially. The tolerance of the CK indicator is

$$\mathrm{CK}_{\mathrm{tol}} = 0.05 \max |\mathrm{CK}|\ , \tag{7.48}$$

where CK is defined as in (7.35). Cells with $|\mathrm{CK}| > \mathrm{CK}_{\mathrm{tol}}$ are refined, whereas those with $|\mathrm{CK}| \le 0.1\mathrm{CK}_{\mathrm{tol}}$ are coarsened. Two neighbouring cells are coarsened as long as they have the same parent and are at the same level. The maximum level of binary refinement is 10 and the width of the coarsest cell allowed is 0.25.

Figure 7.8 shows the flow over a parabolic obstruction at time $t = 2.67$, where at this time, the number of cells is 154. We see that refinements are done

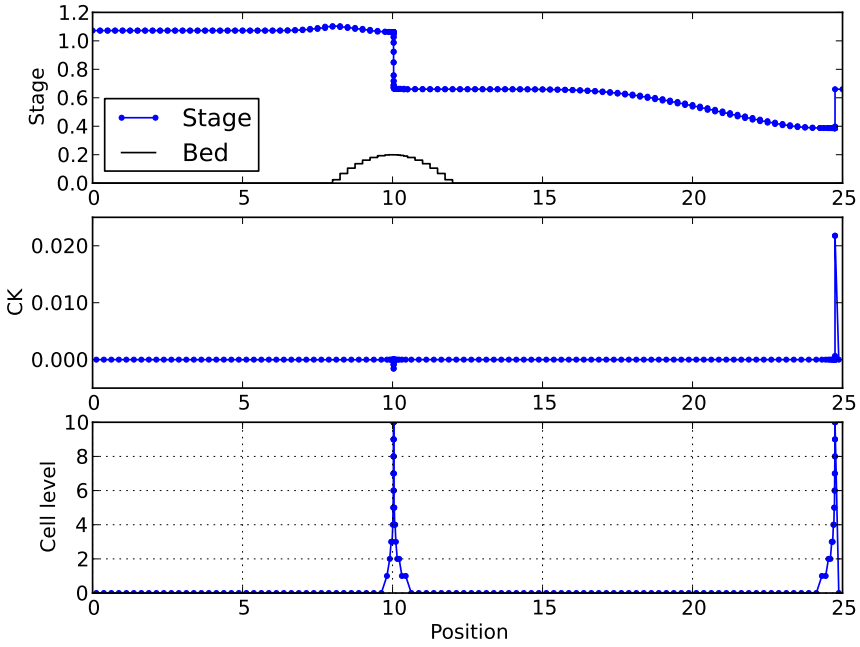

Figure 7.8: Flow over a parabolic obstruction at time $t = 2.67$ using the adaptive method. At this time the number of cells is 154. CK is defined as in (7.35), and $\mathrm{CK}_{\mathrm{tol}} = 0.05 \max |\mathrm{CK}|$.

around the shock moving to the right passing the bump and the shock next to the right boundary. The later shock is artificial due to the enforced right boundary condition. Obviously, a very sharp moving shock passing the bump is achieved in the numerical solution shown in Figure 7.8.

7.4.2 A one-dimensional dam break with passive tracer

In the following simulation, we show that our adaptive method does give an accurate solution around shock, contact discontinuity, and rarefaction.

We consider a one-dimensional dam break problem involving a passive tracer with horizontal topography

$$z(x) = 0\,, \quad \text{for} \quad x \in [-2000, 2000]\,. \tag{7.49}$$

The initial condition is

$$u(x,0) = 0\,, \quad v(x,0) = \begin{cases} 3 & \text{if} \quad -2000 < x < 0\,, \\ 0 & \text{if} \quad 0 < x < 2000\,, \end{cases} \tag{7.50}$$

$$w(x,0) = \begin{cases} 10 & \text{if} \quad -2000 < x < 0\,, \\ 4 & \text{if} \quad 0 < x < 2000\,. \end{cases} \tag{7.51}$$

The spatial domain is discretised into 16 uniform cells initially. We take

$$\mathrm{CK}_{\mathrm{tol}} = 0.01 \max |\mathrm{CK}|\ , \tag{7.52}$$

where CK is defined as in (7.41). The maximum level of binary refinement is 10 and the width of the coarsest cell allowed is 250 .

To solve this problem numerically, we may use the same numerical flux formulation for all three (mass, momentum, and transport) equations. However, to get a more accurate solution at the contact discontinuity of the tracer solution, we choose to apply the standard flux formulation only to the mass and momentum equations. For the passive transport flux, we choose an upwind flux based on $v(x)$ as suggested by Bouchut [7]. The passive transport flux is

$$F^{hv}_{i+1/2} = \begin{cases} F^{h}_{i+1/2} v_i & \text{if} \quad F^{h}_{i+1/2} \geq 0\,, \\ F^{h}_{i+1/2} v_{i+1} & \text{otherwise}\,, \end{cases} \tag{7.53}$$

where $F^{h}_{i+1/2}$ is the mass flux at $x = x_{i+1/2}$.

Cells with $|\mathrm{CK}| > \mathrm{CK}_{\mathrm{tol}}$ are refined, whereas those with $|\mathrm{CK}| \leq 0.1\mathrm{CK}_{\mathrm{tol}}$ are coarsened. Two neighbouring cells are coarsened as long as they have the same parent and are at the same level.

Figure 7.9 shows the flow with passive tracer at time $t = 90$. At this time, the number of cells is 2748 . Our adaptive method indeed results in a very accurate solution over the whole region. The shock and rarefaction occuring in the water surface solution are well-resolved. Moreover, the contact discontinuity remains sharp. Recall that numerical solutions are generally diffusive around contact discontinuities and the sharpness of contact discontinuities are much harder to resolve [28, 56, 57]. Despite the good result in Figure 7.9, we note that if we increase $\mathrm{CK}_{\mathrm{tol}}$ to a larger value, the cell levels at the rarefaction and the contact discontinuity decrease as the time evolves, similar to what happened in Figure 6.8.

7.4.3 A planar dam break

Now we consider a planar dam break problem, which is a one-dimensional flow simulated in two-dimensional framework. A short explanation on how to solve the shallow water equations in two dimensions is given in Appendix A.

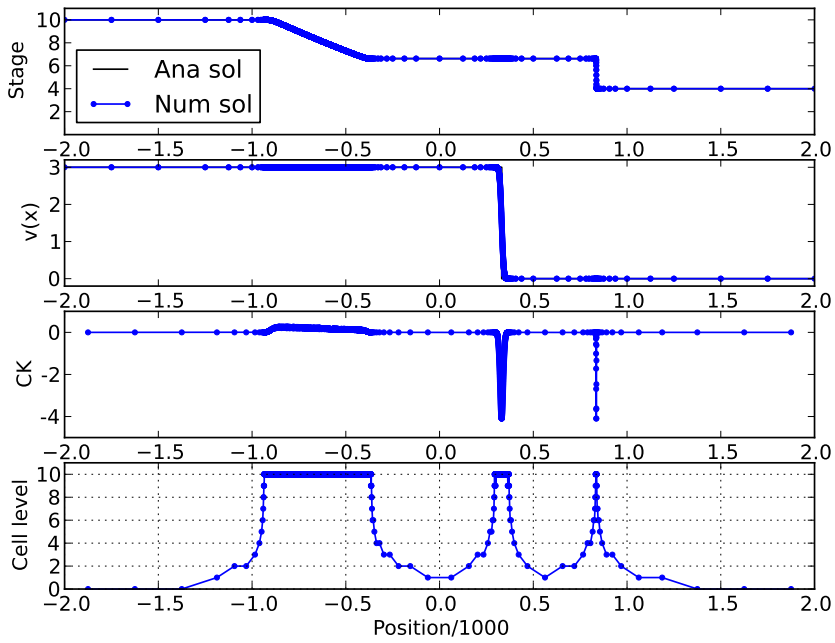

Figure 7.9: The dam-break problem with passive tracer at $t = 90$ using the adaptive method with the CK indicator as defined in (7.41). The water surface and concentration $v(x)$ of tracer is viewed based on the values at vertices of cells, while the others are at centroids of cells. Ana sol and Num sol stand for analytical solution and numerical solution respectively.

We consider a spatial domain defined by $(x, y) \in [-1, 1] \times [-1, 1]$. The domain is discretised into 2048 triangular cells initially. The initial condition is

$$u(x, y, 0) = 0\,, \quad v(x, y, 0) = 0\,, \tag{7.54}$$

$$w(x, y, 0) = \begin{cases} 0.5 & \text{if} \quad x < 0\,, \\ 0.2 & \text{otherwise}\,. \end{cases} \tag{7.55}$$

We take a fixed time step $\Delta t = 0.002$ with 100 iterations. The maximum level of refinement or coarsening is 2, which leads to five different areas of cells after refinement or coarsening. This is because an original initial triangular cell can be refined or coarsened up to two level finer or two level coarser. The CK tolerance is $\mathrm{CK}_{\mathrm{tol}} = 0.5 \max |\mathrm{CK}|$. Cells having $|\mathrm{CK}|$ larger than $\mathrm{CK}_{\mathrm{tol}}$ are candidates for refinement, while otherwise are candidates for coarsening. This simulation uses the *i*FEM data structure and we let the *i*FEM algorithm to do the refinement or coarsening. A description of *i*FEM and its data structure can be found in a

technical report written by Chen [13] and a paper by Chen and Zhang [14]. A summary of *i*FEM's data structure is given in Appendix B.

Representatives of the results are shown in Figure 7.10 and Figure 7.11. Figure 7.10 shows the water surface and the scaled CK indicator $\mathrm{CK}/\max|\mathrm{CK}|$ at time $t = 0.2$. Figure 7.11 depicts the corresponding momentum and mesh at this time ($t = 0.2$), where the number of triangles is now 1656. We see from these results that refinements are done around the shock and rarefaction in order to get an accurate solution.

7.4.4 A radial dam break

In the following simulation, we consider a radial dam break problem resulting in a two-dimensional flow. We use the same solver as in the previous planar dam break simulation, but set up a different initial condition.

We consider a spatial domain defined by $(x, y) \in [-1, 1] \times [-1, 1]$. The initial condition is

$$u(x, y, 0) = 0\,, \quad v(x, y, 0) = 0\,, \tag{7.56}$$

$$w(x, 0) = \begin{cases} 1 & \text{if} \quad x^2 + y^2 < 0.25\,, \\ 0.5 & \text{otherwise}\,. \end{cases} \tag{7.57}$$

The domain is discretised into 2048 triangular cells initially. We take fixed time step $\Delta t = 0.002$ with 25 iterations. The maximum level of refinement or coarsening is 2. The NEP tolerance is $\mathrm{CK}_{\mathrm{tol}} = 0.5 \max|\mathrm{CK}|$. Cells having absolute CK larger than $\mathrm{CK}_{\mathrm{tol}}$ are candidates for refinement, while otherwise are candidates for coarsening.

Representatives of the results are shown in Figure 7.12 and Figure 7.13. Figure 7.12 shows the water surface and the scaled CK indicator $\mathrm{CK}/\max|\mathrm{CK}|$ at time $t = 0.05$. Figure 7.13 depicts the corresponding momentum and mesh at this time ($t = 0.05$), where the number of triangles is now 2168. We see from these results that refinements are, similar to the planar dam simulation, done around the shock and rarefaction in order to get an accurate solution.

Overall, the weak local residuals we formulate produce the expected behaviour of smoothness indicators, so that they can be used in adaptive methods.

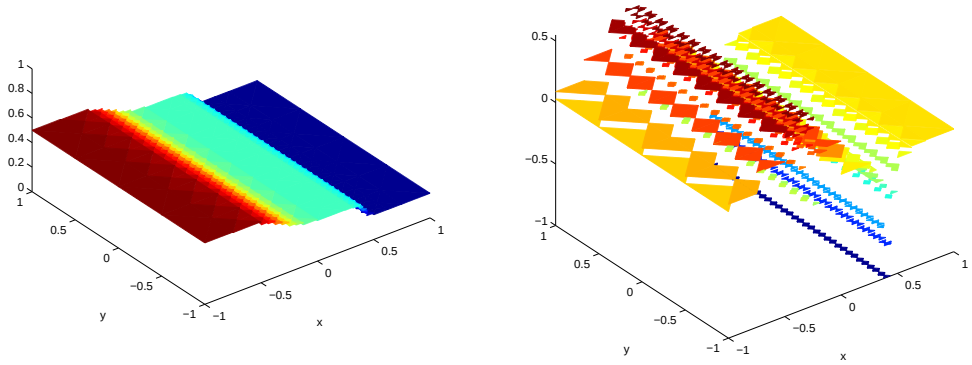

Figure 7.10: The stage and error indicator of the planar dam-break problem at $t = 0.2$ using the adaptive method. The subfigure on the left is the water surface, while on the right is $\mathrm{CK}/\max|\mathrm{CK}|$. The base planes are the xy-plane.

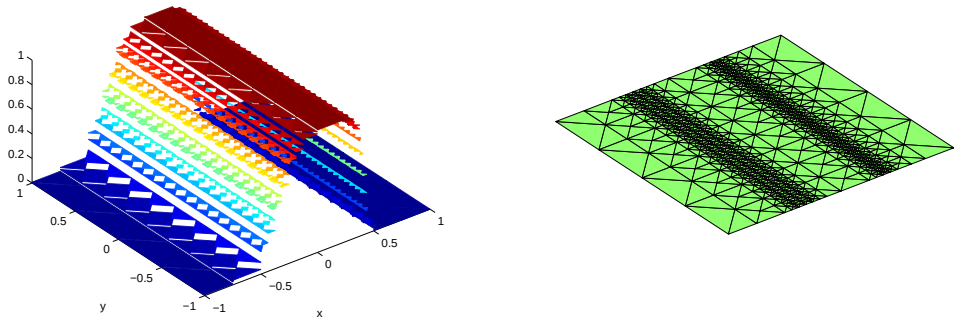

Figure 7.11: The x-momentum and mesh of the planar dam-break problem at $t = 0.2$ using the adaptive method with the CK indicator. The subfigure on the left is the x-momentum, while on the right is the corresponding mesh. The base planes are the xy-plane.

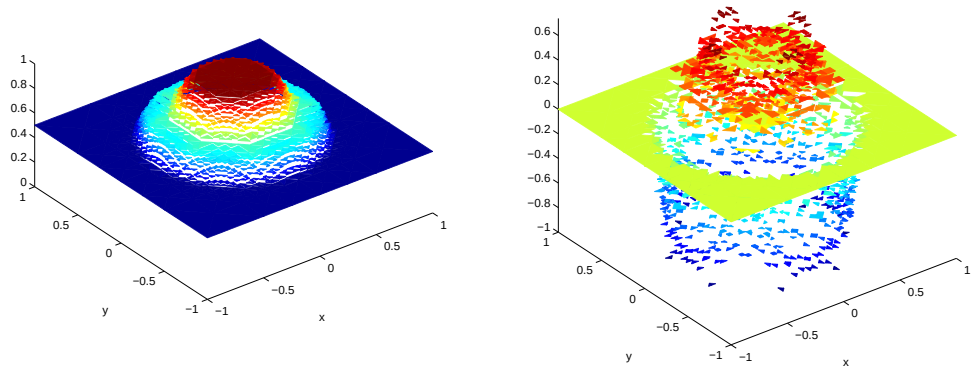

Figure 7.12: The stage and error indicator of the radial dam-break problem at $t = 0.05$ using the adaptive method. The subfigure on the left is the water surface, while on the right is $\mathrm{CK}/\max|\mathrm{CK}|$. The base planes are the xy-plane.

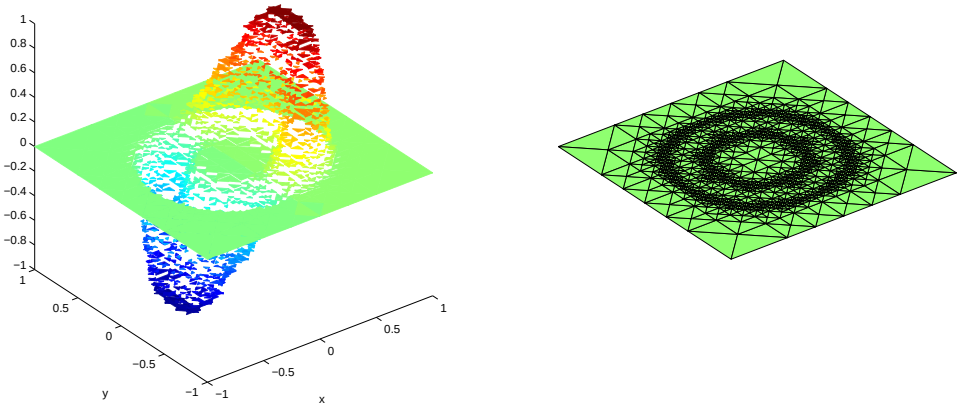

Figure 7.13: The x-momentum and mesh of the radial dam-break problem at $t = 0.05$ using the adaptive method with the CK indicator. The subfigure on the left is x-momentum, while on the right is the corresponding mesh. The base planes are the xy-plane.

7.5 Concluding remarks

Weak local residuals have been formulated to measure the smoothness of solutions of the shallow water equations. Furthermore, weak local residuals have been implemented successfully in adaptive methods as refinement indicators. Even though the theory of weak local residuals as smoothness indicators is so far available only for the scalar conservation law, weak local residuals can also be used as smoothness indicators for the nonhomogeneous shallow water equations, which are a system of balance laws. This suggests that weak local residuals may also be used as smoothness indicators for a system of balance laws in general, as long as an appropriate well-balanced treatment is undertaken.

This page was intentionally left blank.

Chapter 8

Conclusions and future work

At this point, the three aims of this thesis stated in Chapter 1 have been achieved. Now, we shall conclude this thesis and list some possible future work.

8.1 Conclusions

We have studied three aspects in solving the shallow water equations using finite volume methods. The three aspects are the well-balanced method, the derivation of analytical solutions, and developing a refinement indicator.

A well-balanced technique is implemented in finite volume methods, to enable the methods to solve steady state problems accurately. However, the well-balanced technique does not prevent these methods from being applied to solve unsteady state problems. As long as an appropriate combination of quantity reconstructions and treatment of the wet/dry interface is taken, the well-balanced methods preserve the steady state of a lake at rest up to machine precision. The well-balanced technique is studied in one dimension.

New analytical solutions to debris avalanche problems have been derived based on the shallow water approach in one dimension. The analytical solutions can be used to test the performance of finite volume methods and other numerical methods. The limitation of this approach is that the resulting analytical solutions are not physically valid for a very steep sloping topography.

Another analytical solution we study is the Carrier-Greenspan periodic solution for flows on a sloping beach. We found that a linear explicit approximation of the Carrier-Greenspan periodic solution may result in large errors in some cases. A new formula for the shoreline velocity has been derived for this type

of problem. In addition, we provide higher order approximations of the Carrier-Greenspan periodic solution at the zero point of the spatial domain.

Finally, we have studied the numerical entropy production and weak local residuals as refinement indicators. The study includes one, one-and-a-half, and two dimensions. The numerical entropy production and weak local residuals are able to detect smooth and nonsmooth regions successfully in the adaptive methods. We note that error analyses of these indicators is not done in this thesis.

8.2 Future work

The shallow water equations and finite volume methods may always represent a promising direction for research due to their applications in real world scenarios. Possible future work based on this thesis is:

- implementation of a well-balanced technique in two dimensions on structured and unstructured grids,
- seek for a better approach to solve debris avalanche problems on an arbitrary shape of topography,
- research to determine solutions for water flows on a beach with arbitrary shape of topography, and
- conduct error analysis of the numerical entropy production and weak local residuals as refinement indicators.

Each item can be carried out as a large project in its own right.

Appendix A

Equations and methods in two dimensions*

In this appendix, we briefly describe a finite volume method used to solve the two-dimensional shallow water equations. Before we proceed to the finite volume method, we shall write the two-dimensional shallow water equations in integral form as presented in the following section.

A.1 Integral forms of shallow water equations

Recall the two-dimensional shallow water equations (6.64). Integrating (6.64) over an arbitrary closed and connected spatial domain Ω having boundary Γ and applying the Gauss divergence theorem to the flux terms, we obtain the integral form

$$\frac{\partial}{\partial t}\int_{\Omega}\mathbf{q}\,d\Omega+\oint_{\Gamma}\mathbf{F}\cdot\mathbf{n}\,d\Gamma=\int_{\Gamma}\mathbf{s}\,d\Omega\,, \tag{A.1}$$

where $\mathbf{F}=[\mathbf{f}(\mathbf{q})\ \mathbf{g}(\mathbf{q})]^T$ is the flux function, $\mathbf{n}=[\cos(\theta)\ \sin(\theta)]^T$ is the outward normal vector of the boundary, and θ is the angle between $\mathbf{n}$ and the x-direction. Equation (A.1) is called the integral form of the two-dimensional shallow water wave equations.

The rotational invariance property of the shallow water wave equations implies that

$$\mathbf{F}\cdot\mathbf{n}=\mathbf{T}^{-1}\mathbf{f}(\mathbf{T}\mathbf{q})\,, \tag{A.2}$$

*This appendix was part of our published work in an IEEE conference [44], where an extension of that work has also been published by invitation in Journal of Computer Science and Information [49].

where $\mathbf{T}$ is the transformation matrix

$$\mathbf{T} = \begin{bmatrix} 1 & 0 & 0 \\ 0 & \cos(\theta) & \sin(\theta) \\ 0 & -\sin(\theta) & \cos(\theta) \end{bmatrix}. \tag{A.3}$$

Therefore, (A.1) can be rewritten as

$$\frac{\partial}{\partial t}\int_{\Omega} \mathbf{q}\, d\Omega + \oint_{\Gamma} \mathbf{T}^{-1}\mathbf{f}(\mathbf{T}\mathbf{q})\, d\Gamma = \int_{\Gamma} \mathbf{s}\, d\Omega\,. \tag{A.4}$$

Equations (A.1) and (A.4) are integral forms of the two-dimensional shallow water equations (6.64).

A.2 Finite volume methods

In this section, we describe a finite volume method based on integral form (A.4) in order to solve the two-dimensional shallow water equations.

First of all, we need to discretise the spatial domain into a finite number of polygonal cells. In particular, we choose to have triangular cell discretisations. After the spatial domain is discretised into triangular cells, we have the equation constituting the semi-discrete finite volume scheme over each triangular cell of the grid [59]

$$\frac{d\mathbf{q}_i}{dt} + \frac{1}{A_i}\sum_{j\in\mathcal{N}(i)} \mathbf{H}_{ij}\, l_{ij} = \mathbf{s}_i\,. \tag{A.5}$$

Here, $\mathbf{q}_i$ is the vector of conserved quantities averaged over the ith cell, $\mathbf{s}_i$ is the source term associated with the ith cell, $\mathbf{H}_{ij}$ is the outward normal flux of material across the ijth edge, and l_{ij} is the length of the ijth edge. Here, the ijth edge is the interface between the ith and jth cells. The flux $\mathbf{H}_{ij}$ is evaluated using a numerical flux function $\mathbf{H}(\cdot,\cdot;\cdot)$ such that for all conservation vectors $\mathbf{q}$ and normal vectors $\mathbf{n}$

$$\mathbf{H}(\mathbf{q},\mathbf{q};\mathbf{n}) = \mathbf{F}\cdot\mathbf{n}\,. \tag{A.6}$$

Furthermore,

$$\mathbf{H}_{ij} = \mathbf{H}(\mathbf{q}_i(m_{ij}), \mathbf{q}_j(m_{ij}); \mathbf{n}_{ij})\,, \tag{A.7}$$

where m_{ij} is the midpoint of the ijth edge and $\mathbf{n}_{ij}$ is the outward normal vector, with respect to the ith cell, on the ijth edge. The function $\mathbf{q}_i$ is obtained from

the averaged values of quantities in the ith and neighbouring cells. By letting $\mathbf{n}_{ij} = [n_{ij}^{(x)}\ n_{ij}^{(y)}]^T$ and from (A.6) and (A.7), we have

$$\mathbf{H}_{ij} = \mathbf{f}[\mathbf{q}_i(m_{ij})]n_{ij}^{(x)} + \mathbf{g}[\mathbf{q}_j(m_{ij})]n_{ij}^{(y)}\,. \tag{A.8}$$

The algorithm we use to compute the flux term in (A.5) is the same as that described by Guinot [27]. Assuming unit normal, this algorithm has four steps:

1. For each interface (i, j), transform the quantity $\mathbf{q}_i$ and $\mathbf{q}_j$ in the global coordinate system (x, y) into the quantity $\hat{\mathbf{q}}_i$ and $\hat{\mathbf{q}}_j$ in the local coordinate system $(\hat{x}, \hat{y})$. The water depth h is unchanged as it is a scalar variable, whereas the velocities u and v are transformed into $\hat{u}$ and $\hat{v}$. Therefore, the new quantities in the local coordinate system are

$$\hat{\mathbf{q}}_i = \mathbf{T}\mathbf{q}_i \quad \text{and} \quad \hat{\mathbf{q}}_j = \mathbf{T}\mathbf{q}_j\,, \tag{A.9}$$

   where $\mathbf{q}_i = [h_i\ (hu)_i\ (hv)_i]$ and $\mathbf{q}_j = [h_j\ (hu)_j\ (hv)_j]$ are, respectively, the quantities in the global coordinate system. The matrices $\mathbf{T}$ and $\mathbf{T}^{-1}$ are

$$\mathbf{T} = \begin{bmatrix} 1 & 0 & 0 \\ 0 & n_{ij}^{(x)} & n_{ij}^{(y)} \\ 0 & -n_{ij}^{(y)} & n_{ij}^{(x)} \end{bmatrix} \tag{A.10}$$

   and

$$\mathbf{T}^{-1} = \begin{bmatrix} 1 & 0 & 0 \\ 0 & n_{ij}^{(x)} & -n_{ij}^{(y)} \\ 0 & n_{ij}^{(y)} & n_{ij}^{(x)} \end{bmatrix}. \tag{A.11}$$

2. Compute the flux $\hat{f}$ at the interface (i, j). In the local coordinate system, the problem is a one-dimensional Riemann problem with an additional passive tracer transport equation or an additional transverse velocity equation (usually called a one-and-a-half-dimensional Riemann problem), as the flux vector is parallel with the normal vector of the interface. Therefore, the equations to be solved are

$$\hat{\mathbf{q}}_t + \hat{\mathbf{f}}(\hat{\mathbf{q}})_{\hat{x}} = \hat{\mathbf{s}}\,, \tag{A.12}$$

   with initial condition given by $\hat{\mathbf{q}}_i$ on one side of the interface (i, j) and $\hat{\mathbf{q}}_j$ on the other side of the interface (i, j). The conserved quantity $\hat{\mathbf{q}}$, flux $\hat{\mathbf{f}}$,

and source $\hat{\mathbf{s}}$ are

$$\hat{\mathbf{q}} = \begin{bmatrix} h \\ h\hat{u} \\ h\hat{v} \end{bmatrix}, \quad \hat{\mathbf{f}} = \begin{bmatrix} h\hat{u} \\ h\hat{u}^2 + \frac{1}{2}gh^2 \\ h\hat{u}\hat{v} \end{bmatrix}, \quad \text{and} \quad \hat{\mathbf{s}} = \begin{bmatrix} 0 \\ -ghz_{\hat{x}} \\ 0 \end{bmatrix} \tag{A.13}$$

respectively. Here $\hat{v}(\hat{x})$ is the horizontal velocity orthogonal to the $\hat{x}$-axis. For the passive tracer transport model, $\hat{v}(\hat{x})$ is the concentration of the passive tracer. It should be stressed that at this step, we do not need to integrate (A.12) for the quantity $\hat{\mathbf{q}}$, but all we need is the value of the flux $\hat{f}$. Hence, applying either the exact or approximate Riemann solvers to compute the flux $\hat{f}$ at the interface (i, j) is enough. Note that here the source term may not need to be transformed in the local coordinate system, since it involves only scalar variables.

3. Transform the flux $\hat{\mathbf{f}}$ back to the global coordinate system (x, y), so the flux at the midpoint of the interface (i, j) in the global coordinate system is

$$\begin{aligned} \mathbf{H}_{ij} &= \mathbf{T}_{ij}^{-1}\hat{\mathbf{f}} \\ &= \mathbf{T}_{ij}^{-1}\tilde{\mathbf{f}}(\hat{\mathbf{q}}_\mathbf{i}\,; \hat{\mathbf{q}}_\mathbf{j}; \mathbf{s_i}; \mathbf{s_j}) \\ &= \mathbf{T}_{ij}^{-1}\tilde{\mathbf{f}}(\mathbf{T_{ij}}\mathbf{q_i}\,; \mathbf{T_{ij}}\mathbf{q_j}; \mathbf{s_i}; \mathbf{s_j})\,. \end{aligned} \tag{A.14}$$

Here, $\tilde{\mathbf{f}}$ is the flux computed with a Riemann solver for the one-dimensional problem stated in step [ii].

4. Finally, solve (A.5) where $\mathcal{N}(i) = \{0, 1, 2\}$, as triangular grids are considered, for $\mathbf{q}_i$. We multiply $\mathbf{H}_{ij}$ with l_{ij} in order to get the flux over the interface (i, j). This is because the flux at the midpoint of the interface (i, j) is $\mathbf{H}_{ij}$, and the length of the interface (i, j) is l_{ij}.

As we have mentioned, the finite volume method described above is applicable for arbitrary polygonal cells in two dimensions. However, we limit our discussion to triangular cells in this thesis.

Appendix B

Data structure for triangulations in *i*FEM

In this appendix, we summarise the *i*FEM data structure for triangulations to assist mesh adaptation (refinement or coarsening) techniques in the finite volume method used to solve the two-dimensional shallow water equations. We stress that *i*FEM and its data structure are the work of Chen [13].

In our work in this thesis the spatial dimension is two. Let N be the number of triangular vertices and NT be the number of elements. A two-dimensional triangulation is represented by the matrices $node(1 : N, 1 : 2)$ and $elem(1 : NT, 1 : 3)$. The ith row of the matrix *node* represents the (x, y) coordinates of the ith node. The ith row of the matrix *elem* stores the three nodes (global indices of vertices) of the ith element. The three nodes are stored counter-clockwise.

Two conditions on triangulations are imposed. The first condition is that a triangulation must be conforming. That is, the intersection of any two simplexes and in the triangulation is either empty or a common lower dimensional simplex. The second condition is that all triangulations must be shape regular. A set $\mathcal{T}$ of triangulations T is called shape regular if there exists a constant c_0 such that

$$\max_{\tau \in T} \frac{\mathrm{diam}(\tau)^2}{|\tau|} \leq c_0 \tag{B.1}$$

for all triangulation T in $\mathcal{T}$, where $\mathrm{diam}(\tau)$ is the diameter of τ and $|\tau|$ is the measure of τ.

The rest of this appendix is organised as follows. We present a summary of the refinement method used in *i*FEM in Section B.1. In Section B.2 a summary

of the *i*FEM coarsening method is provided. Section B.3 briefly explains how to deal with conserved quantites in finite volume methods.

B.1 A newest vertex bisection for refinement

A newest vertex bisection method is implemented for grid refinement, where the initial bisection of the initial triangulation is based on the longest edge bisection. Some discussion on the newest vertex bisection method is also found in the work of Stals [64], in addition to that of Chen [13]. The function bisect refines a given triangulation by bisecting marked elements and minimal neighbouring elements to get a conforming and shape regular triangulation.

A triangulation is labeled as follows. Note that global indices of three vertices of a triangle t are given by $\text{elem}(t, [1, 2, 3])$. The newest vertex of the triangle t is set as $\text{elem}(t, 1)$ and the refinement edge is $\text{elem}(t, [2, 3])$. That is, if we label vertices of the parent t as p_1, p_2, p_3 and the new node relating to a refinement of t is p_4, then the children of t have vertices p_4, p_1, p_2 and p_4, p_3, p_1. The first child called the LEFT (L) child occupies the location used by t. The second child called the RIGHT (R) child is appended as a new element to elem matrix. To be specific, the first (L) child is stored in a prior to the second (R) child in elem matrix. We call this storing technique the (L,R) positioning.

Bisections over a collection of elements could result in a non-conforming triangulation. To enforce that we get a conforming triangulation, we proceed as follows. Let $\text{cutEdge}(\tau)$ be the refinement edge of τ and $F(\tau)$ be the refinement neighbour of τ. The refinement neighbour means the neighbour sharing the refinement edge of τ. We note that a triangle τ has at most three neighbours and we may have that $\text{cutEdge}(\tau) \neq \text{cutEdge}(F(\tau))$. The rule that enforces comformity is that if $\text{cutEdge}(\tau)$ is bisected, then $\text{cutEdge}(F(\tau))$ must also be bisected. In *i*FEM, this rule is implemented in a loop and the loop terminates in a finite number of steps producing a conforming triangulation.

B.2 A nodal-wise algorithm for coarsening

A nodal-wise coarsening algorithm is used for adaptive grids obtained from newest vertex bisections, with a note that the algorithm enforces not to coarsen the grids in the initial triangulation. A coarsening process is thought as the inverse of a

conforming bisection and restricted to a conforming star. A conforming bisection means a bisection which results in a conforming triangulation, and a conforming star means a star-shaped domain consisting of some conforming triangles.

A node p is called a *good-for-coarsening node* or a *good node* in short if there exists a conforming bisection b_e such that p is the middle point of e, where b_e bisects

- two conforming triangles into four conforming triangles if e is an interior edge or
- one triangle into two conforming triangles if e is a boundary edge.

Finding good nodes can be described as follows. Let T and T_0 be conforming triangulations, where T can be found by refinement of some triangles of T_0. A node of T is a good node if and only if

1. it is not a vertex of T_0
2. it is the newest vertex of all elements in the star of the node
3. the number of elements in the star is four if the node is an interior node or two if otherwise (a boundary node).

Therefore, if some triangles of T are marked to be coarsened then we check the newest vertices, which satisfies the three conditions, of the marked elements.

After good nodes are identified, coarsening of conforming stars can be done by considering the (L,R) type of positioning. If a good node is an interior node then four conforming triangles are coarsened into two conforming ones. If a good node is a boundary node then two conforming triangles are coarsened into one triangle.

Actions are taken with respect to conserved quantities when we do refinement and/or coarsening. These are described in the following section.

B.3 Conserved quantites in finite volume methods

The data structure for conserved quantities follows from the structure for triangulations. In addition, if a parent-cell is bisected then we do a weighted splitting of

the quantity volume of the parent-cell into two parts for the resulting child-cells. If two conforming child-cells are coarsened then we do a weighted averaging of the quantity volumes of the child-cells for the resulting parent-cell. The splitting and averaging are done in a proportional weight with respect to the areas of the base child-cells.

This appendix is provided only to facilitate our work in this thesis. More detailed explanations on *i*FEM and its data structure can be found in a technical report written by Chen [13] and a paper by Chen and Zhang [14].

References

[1] C. Ancey, R. M. Iverson, M. Rentschler, and R. P. Denlinger. An exact solution for ideal dam-break floods on steep slopes. *Water Resources Research*, 44(W01430):1–10, 2008. http://dx.doi.org/10.1029/2007WR006353.

[2] E. Audusse, F. Bouchut, M. O. Bristeau, R. Klein, and B. Perthame. A fast and stable well-balanced scheme with hydrostatic reconstruction for shallow water flows. *SIAM Journal of Scientific Computing*, 25(6):2050–2065, 2004. http://dx.doi.org/10.1137/S1064827503431090.

[3] G. Bellotti and M. Brocchini. On the shoreline boundary conditions for Boussinesq-type models. *International Journal for Numerical Methods in Fluids*, 37(4):479–500, 2001. http://dx.doi.org/10.1002/fld.194.

[4] A. Bermudez and M. E. Vazquez. Upwind methods for hyperbolic conservation laws with source terms. *Computers & Fluids*, 23(8):1049–1071, 1994. http://dx.doi.org/10.1016/0045-7930(94)90004-3.

[5] A. Bollermann, A. Kurganov, and S. Noelle. A well-balanced reconstruction for wetting/drying fronts. *IGPM Report*, 313:1–18, 2010. http://www.igpm.rwth-aachen.de/Download/reports/noelle/Bollermann-Kurganov-Noelle_IGPM_Report.pdf.

[6] F. Bouchut. *Nonlinear Stability of Finite Volume Methods for Hyperbolic Conservation Laws*. Birkhäuser Verlag, Basel, 2004. http://www.springer.com/birkhauser/mathematics/book/978-3-7643-6665-0.

[7] F. Bouchut. Efficient numerical finite volume schemes for shallow water models. *In V. Zeitlin (editor), Nonlinear dynamics of rotating shallow water: methods and advances. Edited series on advances in nonlinear*

science and complexity, 2:189–256, 2007. http://dx.doi.org/10.1016/S1574-6909(06)02004-1.

[8] F. Bouchut and M. Westdickenberg. Gravity driven shallow water models for arbitrary topography. *Communications in Mathematical Sciences*, 2(3):359–389, 2004. http://projecteuclid.org/euclid.cms/1109868726.

[9] R. Briganti and N. Dodd. Shoreline motion in nonlinear shallow water coastal models. *Coastal Engineering*, 56(5–6):495–505, 2009. http://dx.doi.org/10.1016/j.coastaleng.2008.10.008.

[10] M. Brocchini, I. A. Svendsen, R. S. Prasad, and G. Bellotti. A comparison of two different types of shoreline boundary conditions. *Computer Methods in Applied Mechanics and Engineering*, 191(39–40):4475–4496, 2002. http://dx.doi.org/10.1016/S0045-7825(02)00392-4.

[11] P. Brufau, M. E. Vázquez-Cendón, and P. García-Navarro. A numerical model for the flooding and drying of irregular domains. *International Journal for Numerical Methods in Fluids*, 39(3):247–275, 2002. http://dx.doi.org/10.1002/fld.285.

[12] G. F. Carrier and H. P. Greenspan. Water waves of finite amplitude on a sloping beach. *Journal of Fluid Mechanics*, 4(1):97–109, 1958. http://dx.doi.org/10.1017/S0022112058000331.

[13] L. Chen. *iFEM: An innovative finite element methods package in MATLAB*. Technical report, University of California, Irvine, 2008. http://math.uci.edu/~chenlong/Papers/iFEMpaper.pdf.

[14] L. Chen and C.-S. Zhang. A coarsening algorithm on adaptive grids by newest vertex bisection and its applications. *Journal of Computational Mathematics*, 28(6):767–789, 2010. http://dx.doi.org/10.4208/jcm.1004-m3172.

[15] Y. Chen, A. Kurganov, M. Lei, and Y. Liu. An adaptive artificial viscosity method for the Saint-Venant system. *Notes on Numerical Fluid Mechanics and Multidisciplinary Design*, 120:125–141, 2012. http://dx.doi.org/10.1007/978-3-642-33221-0_8.

[16] L. A. Constantin and A. Kurganov. Adaptive central-upwind schemes for hyperbolic systems of conservation laws. *In F. Asakura et al. (editors), Hyperbolic problems: Theory, numerics, and applications. Proceedings of the 10th international conference, Osaka, Japan, 13–17 September 2004, Yokohama Publishers, Yokohama, 2006*, 1:95–103. http://129.81.170.14/~kurganov/Constantin-Kurganov.pdf.

[17] R. Courant and K. O. Friedrichs. *Supersonic Flow and Shock Waves*. Interscience Publishers, New York, 1948. http://www.springer.com/mathematics/analysis/book/978-0-387-90232-6.

[18] A. J. C. B. de Saint-Venant. Theorie du mouvement non-permanent des eaux, avec application aux crues des rivieres et a l'introduction des marees dans leur lits. *Comptes Rendus de l'Academie des Sciences, Paris*, 73:147–154; 237–240, 1871.

[19] J. C. Dietrich, R. L. Kolar, and R. A. Luettich. Assessment of ADCIRC's wetting and drying algorithm. *In C. T. Miller et al. (editors), Proceedings of the 15th International Conference on Computational Methods in Water Resources (CMWR XV) 13–17 June 2004*, 2:1767–1778, 2004. http://www.caseydietrich.com/Publications/CMWR2004.pdf.

[20] R. F. Dressler. Mathematical solution of the problem of roll-waves in inclined open channels. *Communications on Pure and Applied Mathematics*, 2(2–3):149–194, 1949. http://dx.doi.org/10.1002/cpa.3160020203.

[21] R. F. Dressler. Unsteady non-linear waves in sloping channels. *Proceedings of the Royal Society of London. Series A, Mathematical and Physical Sciences*, 247(1249):186–198, 1958. http://dx.doi.org/10.1098/rspa.1958.0177.

[22] M. Ersoy, F. Golay, and L. Yushchenko. Adaptive multi-scale scheme based on numerical entropy production for conservation laws. *Central European Journal of Mathematics*, page to appear, 2013. http://imath.univ-tln.fr/fichier/preprints/imath_20120328120101_83.pdf.

[23] J. Felcman and L. Kadrnka. Adaptive finite volume approximation of the shallow water equations. *Applied Mathematics and Computation*, 219(7):3354–3366, 2012. http://dx.doi.org/10.1016/j.amc.2011.04.042.

[24] J. M. Gallardo, C. Parés, and M. Castro. On a well-balanced high-order finite volume scheme for shallow water equations with topography and dry areas. *Journal of Computational Physics*, 227(1):574–601, 2007. http://dx.doi.org/10.1016/j.jcp.2007.08.007.

[25] F. Golay. Numerical entropy production and error indicator for compressible flows. *Comptes Rendus Mecanique*, 337(4):233–237, 2009. http://dx.doi.org/10.1016/j.crme.2009.04.004.

[26] N. Goutal and F. Maurel. *Technical Report HE-43/97/016/B: Proceedings of the 2nd Workshop on Dam-Break Wave Simulation*. Direction des études et recherches, Electricité de France, Paris, 1997.

[27] V. Guinot. *Wave Propagation in Fluids: Models and Numerical Techniques*. ISTE (and John Wiley & Sons), London (and Hoboken), 2008. http://www.iste.co.uk/index.php?f=a&ACTION=View&id=368.

[28] A. Harten. The artificial compression method for computation of shocks and contact discontinuities. I.: Single conservation laws. *Communications on Pure and Applied Mathematics*, 30(5):611–638, 1977. http://dx.doi.org/10.1002/cpa.3160300506.

[29] D. D. Houghton and A. Kasahara. Nonlinear shallow fluid flow over an isolated ridge. *Communications on Pure and Applied Mathematics*, 21(1):1–23, 1968. http://dx.doi.org/10.1002/cpa.3160210103.

[30] J. Jakeman. *Honours thesis: On numerical solutions of the shallow water wave equations*. The Australian National University, Canberra, 2006.

[31] B. Johns. Numerical integration of the shallow water equations over a sloping shelf. *International Journal for Numerical Methods in Fluids*, 2(3):253–261, 1982. http://dx.doi.org/10.1002/fld.1650020304.

[32] S. Karni and A. Kurganov. Local error analysis for approximate solutions of hyperbolic conservation laws. *Advances in Computational Mathematics*, 22(1):79–99, 2005. http://dx.doi.org/10.1007/s10444-005-7099-8.

[33] S. Karni, A. Kurganov, and G. Petrova. A smoothness indicator for adaptive algorithms for hyperbolic systems. *Journal of Computational Physics*, 178(2):323–341, 2002. http://dx.doi.org/10.1006/jcph.2002.7024.

[34] R. Knobel. *An Introduction to the Mathematical Theory of Waves*. American Mathematical Society, Providence, 2000. http://www.ams.org/bookpages/stml-3.

[35] A. Kurganov and Y. Liu. New adaptive artificial viscosity method for hyperbolic systems of conservation laws. *Journal of Computational Physics*, 231(24):8114–8132, 2012. http://dx.doi.org/10.1016/j.jcp.2012.07.040.

[36] A. Kurganov, S. Noelle, and G. Petrova. Semidiscrete central-upwind schemes for hyperbolic conservation laws and Hamilton-Jacobi equations. *SIAM Journal on Scientific Computing*, 23(3):707–740, 2001. http://dx.doi.org/10.1137/S1064827500373413.

[37] B. Larrouturou. How to preserve the mass fractions positivity when computing compressible multi-component flows. *Journal of Computational Physics*, 95(1):59–84, 1991. http://dx.doi.org/10.1016/0021-9991(91)90253-H.

[38] A. S. Leon, M. S. Ghidaoui, A. R. Schmidt, and M. H. Garcia. An efficient finite-volume scheme for modeling water hammer flows. *In W. James (editor), Contemporary modeling of urban water systems, Monograph 15. Proceedings of stormwater and urban water systems modeling conference, Toronto, 2006*, pages 411–430, 2007. https://netfiles.uiuc.edu/asleon/www/web/Toronto.pdf.

[39] R. J. LeVeque. *Numerical Methods for Conservation Laws*. Birkhäuser Verlag, Basel, 2nd edition, 1992. http://www.springer.com/birkhauser/mathematics/book/978-3-7643-2723-1.

[40] R. J. LeVeque. *Finite-Volume Methods for Hyperbolic Problems*. Cambridge University Press, Cambridge, 2002. http://dx.doi.org/10.1017/CBO9780511791253.

[41] A. Mangeney, P. Heinrich, and R. Roche. Analytical solution for testing debris avalanche numerical models. *Pure and Applied Geophysics*, 157(6–8):1081–1096, 2000. http://dx.doi.org/10.1007/s000240050018.

[42] K. W. Morton and D. F. Mayers. *Numerical Solution of Partial Differential Equations*. Cambridge University Press, Cambridge, 2nd edition,

2005. http://www.cambridge.org/gb/knowledge/isbn/item1110027/?site_locale=en_GB.

[43] S. Mungkasi. *Masters thesis: Finite volume methods for the one-dimensional shallow water equations.* The Australian National University, Canberra, 2008.

[44] S. Mungkasi and S. G. Roberts. A finite volume method for shallow water flows on triangular computational grids. *Proceedings of IEEE International Conference on Advanced Computer Science and Information System (ICACSIS) 2011*, pages 79–84. http://ieeexplore.ieee.org/xpl/freeabs_all.jsp?arnumber=6140781.

[45] S. Mungkasi and S. G. Roberts. On the best quantity reconstructions for a well balanced finite volume method used to solve the shallow water wave equations with a wet/dry interface. *ANZIAM Journal (E)*, 51:C48–C65, 2010. http://journal.austms.org.au/ojs/index.php/ANZIAMJ/article/view/2576/1289.

[46] S. Mungkasi and S. G. Roberts. A new analytical solution for testing debris avalanche numerical models. *ANZIAM Journal (E)*, 52:C349–C363, 2011. http://journal.austms.org.au/ojs/index.php/ANZIAMJ/article/view/3785/1465.

[47] S. Mungkasi and S. G. Roberts. Numerical entropy production for shallow water flows. *ANZIAM Journal (E)*, 52:C1–C17, 2011. http://journal.austms.org.au/ojs/index.php/ANZIAMJ/article/view/3786/1410.

[48] S. Mungkasi and S. G. Roberts. Analytical solutions involving shock waves for testing debris avalanche numerical models. *Pure and Applied Geophysics*, 169(10):1847–1858, 2012. http://dx.doi.org/10.1007/s00024-011-0449-1.

[49] S. Mungkasi and S. G. Roberts. ANUGA software for numerical simulations of shallow water flows. *Journal of Computer Science and Information*, 5(1):1–8, 2012. http://jiki.cs.ui.ac.id/index.php/jiki/article/view/180/100.

[50] S. Mungkasi and S. G. Roberts. Approximations of the Carrier–Greenspan periodic solution to the shallow water wave equations for flows on a sloping beach. *International Journal for Numerical Methods in Fluids*, 69(4):763–780, 2012. http://dx.doi.org/10.1002/fld.2607.

[51] S. Mungkasi and S. G. Roberts. Behaviour of the numerical entropy production of the one-and-a-half-dimensional shallow water equations. *ANZIAM Journal (E)*, page to appear, 2013. http://journal.austms.org.au/ojs/index.php/ANZIAMJ.

[52] M. Naaim, S. Vial, and R. Couture. Saint Venant approach for rock avalanches modelling. *Proceedings of the Saint Venant Symposium: Multiple scale analyses and coupled physical systems,* Presses de l'École Nationale des Ponts et Chaussées, Paris, pages 61–69, 1997.

[53] S. Noelle, N. Pankratz, G. Puppo, and J. R. Natvig. Well-balanced finite volume schemes of arbitrary order of accuracy for shallow water flows. *Journal of Computational Physics*, 213(2):474–499, 2006. http://dx.doi.org/10.1016/j.jcp.2005.08.019.

[54] G. Puppo. Numerical entropy production on shocks and smooth transitions. *Journal of Scientific Computing*, 17(1–4):263–271, 2002. http://dx.doi.org/10.1023/A:1015117118157.

[55] G. Puppo. Numerical entropy production for central schemes. *SIAM Journal on Scientific Computing*, 25(4):1382–1415, 2003. http://dx.doi.org/10.1137/S1064827502386712.

[56] G. Puppo and M. Semplice. Entropy and the numerical integration of conservation laws. submitted to *Physics Procedia, Proceedings of the 2nd annual meeting of the Lebanese Society for Mathematical Sciences 2011*, 2011. http://calvino.polito.it/~puppo/papers/lebanon.pdf.

[57] G. Puppo and M. Semplice. Numerical entropy and adaptivity for finite volume schemes. *Communications in Computational Physics*, 10(5):1132–1160, 2011. http://dx.doi.org/10.4208/cicp.250909.210111a.

[58] A. Ritter. Die fortpflanzung der wasserwellen. *Zeitschrift des Vereines Deutscher Ingenieure*, 36(33):947–954, 1892.

[59] S. Roberts, O. Nielsen, D. Gray, and J. Sexton. *ANUGA User Manual*. Geoscience Australia, 2010. http://anuga.anu.edu.au.

[60] S. B. Savage and K. Hutter. The motion of a finite mass of granular material down a rough incline. *Journal of Fluid Mechanics*, 199:177–215, 1989. http://dx.doi.org/10.1017/S0022112089000340.

[61] S. B. Savage and K. Hutter. The dynamics of avalanches of granular materials from initiation to run-out. Part I: Analysis. *Acta Mechanica*, 86(1–4):201–223, 1991. http://dx.doi.org/10.1007/BF01175958.

[62] G. L. D. Sidén and D. R. Lynch. Wave equation hydrodynamics on deforming elements. *International Journal for Numerical Methods in Fluids*, 8(9):1071–1093, 1988. http://dx.doi.org/10.1002/fld.1650080908.

[63] J. Smoller. *Shock Waves and Reaction-Diffusion Equations*. Springer-Verlag, New York, 1983. http://www.springer.com/mathematics/analysis/book/978-0-387-94259-9.

[64] L. Stals. *Ph.D. thesis: Parallel multigrid on unstructured grids using adaptive finite element methods*. The Australian National University, Canberra, 1995.

[65] J. J. Stoker. The formation of breakers and bores. *Communications on Pure and Applied Mathematics*, 1(1):1–87, 1948. http://dx.doi.org/10.1002/cpa.3160010101.

[66] J. J. Stoker. *Water Waves: The Mathematical Theory with Application*. Interscience Publishers, New York, 1957. http://onlinelibrary.wiley.com/book/10.1002/9781118033159.

[67] J. C. Strikwerda. *Finite Difference Schemes and Partial Differential Equations*. SIAM, Philadelphia, 2nd edition, 2004. http://dx.doi.org/10.1137/1.9780898717938.

[68] E. Tadmor. Entropy stability theory for difference approximations of nonlinear conservation laws and related time-dependent problems. *Acta Numerica*, 12:451–512, 2003. http://dx.doi.org/10.1017/S0962492902000156.

[69] Y. C. Tai, S. Noelle, J. M. N. T. Gray, and K. Hutter. Shock-capturing and front-tracking methods for granular avalanches. *Journal of Computational*

Physics, 175(1):269–301, 2002. http://dx.doi.org/10.1006/jcph.2001.6946.

[70] W. Tan. *Shallow Water Hydrodynamics: Mathematical Theory and Numerical Solution for a Two-Dimensional System of Shallow Water Equations*. Elsevier Science Publishers, Amsterdam, 1992. http://www.sciencedirect.com/science/bookseries/04229894/55.

[71] W. C. Thacker. Some exact solutions to the nonlinear shallow water equations. *Journal of Fluid Mechanics*, 107:499–508, 1981. http://dx.doi.org/10.1017/S0022112081001882.

[72] G. Watson, D. H. Peregrine, and E. F. Toro. Numerical solution of the shallow-water equations on a beach using the weighted average flux method. *Computational Fluid Dynamics '92, Proceedings of the First European Computational Fluid Dynamics Conference, Brussels, 7–11 September 1992*, 1:495–502, 1992.

[73] O. C. Zienkiewicz, R. L. Taylor, and P. Nithiarasu. *The Finite Element Method for Fluid Dynamics*. Elsevier Butterworth-Heinemann, Burlington, 6th edition, 2005. http://store.elsevier.com/The-Finite-Element-Method-for-Fluid-Dynamics/O_-C_-Zienkiewicz/isbn-9780750663229/.